

Low Energy Collisions in Merged Neutral Molecular Beams

THÈSE N° 6210 (2014)

PRÉSENTÉE LE 20 JUIN 2014

À LA FACULTÉ DES SCIENCES DE BASE

GROUPE OSTERWALDER

PROGRAMME DOCTORAL EN CHIMIE ET GÉNIE CHIMIQUE

ÉCOLE POLYTECHNIQUE FÉDÉRALE DE LAUSANNE

POUR L'OBTENTION DU GRADE DE DOCTEUR ÈS SCIENCES

PAR

Benjamin BERTSCHE

acceptée sur proposition du jury:

Prof. Y. Tsybin, président du jury

Prof. A. Osterwalder, directeur de thèse

Dr M. Drabbels, rapporteur

Dr S. Y. van de Meerakker, rapporteur

Prof. S. Willitsch, rapporteur



ÉCOLE POLYTECHNIQUE
FÉDÉRALE DE LAUSANNE

Suisse
2014

Alles läuft perfekt,
schon seit Stunden:
Wissenschaftliche
Experimente.
“Doch was nützen die
am Ende” denkt
sich Major Tom.
— Peter Schilling

To Steffi,
Marla and Romy,
and my parents.



Acknowledgements

First things first. The following pages would not exist, if not for the help and support of many other people. Some of them I will mention here explicitly.

I have to thank especially my wife Steffi for her support. During my thesis I was away from home for a few days almost every week. She was doing all our family chores all alone by herself. Without her I could not have been sufficiently focused on my research. She was, and still is, the base on which I can rely.

All the research described later would not have been realized, in the first place, without Andreas. Not only had he developed the basic ideas for all our experiments, he also made it possible, in his very own pragmatic way, for me work in Lausanne and live in Freiburg (i. Br.). Without his deep understanding of science and his visionary foresight, these experiments would never have been possible and I would have been lost in science. He guided me through all of this.

The work I have done in the last 3 and a half years wouldn't be rewarded with a degree, if Justin had not joined our lab just at the right time. I already decided to break up my thesis when he finally brought the machine to work literally within the last few days. Just as my enthusiasm went away, he came with his vast enthusiasm for science and his practical skills in how to run an experiment, so that I had suddenly both: The missing data and a returned enthusiasm. Without his help I would have given up.

Besides countless standard pieces, the final design of the merged beam apparatus contained over 200 custom-made parts in nearly 50 different designs. In building this experiment from scratch, I took profit enormously from the experience and passion of the people from our mechanical workshop. I especially annoyed André Fattet and Christophe Clément with daily visits while the custom-made parts were in production. They pulled the machine out of the drawings into our lab.

I could rely on Gil, Thomas, George, Morten, Maarten, Nils, Xiaohang, Liudmilla and Antoine if I needed distraction from the daily lab routine. The strong and pragmatic support of Marianne always helped me, when bureaucracy was about to tear me down.

Here, at the bottom of this text comes the foundation of all my achievements: my parents. They provided me something which is hard to pin down to certain events or actions. I just knew, and still know, that there are two persons who will catch me when ever I might fall. Without them I would never have had the courage to make the decision which later turned out to be right.

Lausanne, April 15, 2014

B. B.



Abstract

Within this thesis two experiments will be described.

In the first experiment a *velocity filter* was used to obtain a beam of polar molecules (ND_3) with a translational temperature of less than 5 K. For the first time the dynamics of individual rotational states inside a velocity filter could be investigated directly. Usually a *velocity filter* defines only a maximum velocity that can pass the filter. We successfully implemented two different approaches where molecules below a certain minimal velocity are removed from the beam, turning the *velocity filter* into a bandpass filter.

The second and more interesting experiment is the *merged beam* experiment. We developed and constructed the first apparatus which successfully merged two guided beams, one consisting of polar molecules, the other of paramagnetic particles, into an overlapping parallel movement. With this approach we could lower the temperature at which the reaction of metastable Ne^* with ND_3 , NH_3 and CH_3F has been investigated by 3 orders of magnitude down to the sub-kelvin regime. Especially the stereochemistry of those reactions revealed an unexpected energy-insensitivity at temperatures below 200 K. As our setup is very general the investigation of many more neutral-neutral reactions will be possible, opening a new route into a temperature regime where only a few reactions have been studied before.

keywords

Cold chemistry, velocity filtering, merged molecular beams, sub-kelvin neutral-neutral reactions, Penning ionization, stereochemistry

German abstract



Zusammenfassung

Diese Arbeit beschreibt zwei Experimente.

Im ersten Experiment wurde ein *Geschwindigkeitsfilter* benutzt, um einen Strahl aus polaren Molekülen mit einer translatorischen Temperatur von weniger als 5 K zu erzeugen. Zum ersten Mal konnten die Dynamik einzelner Rotationszustände in einem Geschwindigkeitsfilter direkt untersucht werden. Normalerweise können Geschwindigkeitsfilter nur eine obere Grenze für die Geschwindigkeit festlegen. Wir verwendeten erfolgreich zwei verschiedene Techniken, um auch Moleküle unterhalb einer unteren Schranke aus dem Strahl zu entfernen und den Geschwindigkeitsfilter so in einen Bandpassfilter zu verwandeln.

Das zweite, und interessantere, Experiment ist das *Vereinigte Strahlen* Experiment. Wir entwickelten und konstruierten die erste Maschine, die erfolgreich zwei geführte Strahlen, einer bestehend aus polaren Molekülen, der andere aus paramagnetischen Teilchen, in eine parallele und überlappende Bewegung vereinigt. Mit diesem Ansatz konnten wir die Temperaturen, bei der die Reaktion von metastabilen Ne^* mit NH_3 , ND_3 und CH_3F untersucht wurden, um drei Größenordnungen, bis an den Rand des ultrakalten Bereichs, senken. Besonders die Stereochemie dieser Reaktionen zeigte unterhalb von 200 K eine unerwartete Unabhängigkeit von der Kollisionsenergie. Unser genereller Ansatz ermöglicht die Untersuchung vieler weiterer Reaktionen mit neutralen Reaktanten. Dies eröffnet einen neuen Zugang zu Temperaturen bei denen erst wenige Reaktionen untersucht werden konnten.

Schlüsselwörter

Kalte Chemie, Geschwindigkeitsfilter, vereinigte Molekularstrahlen, Reaktionen zwischen neutralen Teilchen im Sub-Kelvin Bereich, Penning Ionisation, Stereochemie



Contents

Acknowledgements	v
List of figures	xii
List of tables	xiv
1 Motivation	1
1.1 Cold Chemistry	1
1.1.1 Scientific Interest	1
1.1.2 State of the Art	3
2 Introduction	5
2.1 Collision Kinematics	5
2.1.1 Collision Energies	5
2.1.2 Energy Resolution in Merged Beam Experiments	7
2.1.3 Reaction Rate and Cross Section	9
2.2 Penning Ionization	10
2.2.1 Cross Section of the Penning Ionization	11
2.2.2 Penning Ionization of Ammonia by Metastable Ne [*]	14
2.3 Stereochemistry	16
2.3.1 Stereochemistry of the Penning Ionization	16
2.4 Manipulation of Neutrals	17
2.4.1 Stark Effect	17
2.4.2 Zeeman Effect	21
2.5 Guiding	24
2.5.1 The Hexapole Guide	24
2.5.2 Curved Hexapole Guide	29
2.6 Trajectory Simulations	34
2.7 Detection Methods	37
2.7.1 REMPI	37
3 Velocity Filtering	41
3.1 Introduction	41
3.2 Experimental Setup	43

Contents

3.2.1	Effusive Source	45
3.2.2	Guide	47
3.2.3	Detection	52
3.3	Measurements	53
3.3.1	Arrival Time Traces of a Hexapole Configuration	53
3.3.2	Switching the Segments - Bandpass Filter	55
3.3.3	The Hexapole and the Dipole Configuration	58
3.3.4	Filtering of Different States	61
3.3.5	Measuring the Transmission Probability	67
3.4	Conclusions	69
4	Merged Beams	71
4.1	Motivation	71
4.2	Former Experiments	73
4.2.1	Crossed Beam Experiments with small Intersection Angles	73
4.2.2	CRESU	73
4.2.3	Merged Beam Experiment of Henson <i>et al.</i>	73
4.3	Experimental Setup	75
4.3.1	The Sources	77
4.3.2	The Guides	78
4.3.3	Detection	90
4.4	Measurements	95
4.5	Results	98
4.5.1	Reaction Rates	98
4.5.2	Stereochemistry	102
4.5.3	Improvements of the Experimental Apparatus	105
4.6	Conclusions	106
5	Conclusions	107
	Bibliography	117
	Curriculum Vitae	

List of Figures

1.1	Picture of an Interstellar Cloud	2
2.1	Laboratory Frame and Center-of-Mass Frame	5
2.2	Energy Resolutions with Pulsed Beams	8
2.3	Potential Curves of the Penning Ionization	11
2.4	Energies of NH_3^+ , $\text{NH}_2^+ + \text{H}$ and Metastable Ne^*	14
2.5	Stark Effect of H_2O , CO , H_2CO and CH_3F	18
2.6	Definition of the Rotational Quantum Numbers J , K and M	19
2.7	Stark Effect for Ammonia	20
2.8	Electric and Magnetic Hexapole	24
2.9	Electric Fields along Different Cross Sections of an Electric Hexapole.	24
2.10	Magnetic Fields along Different Cross Sections of a Magnetic Hexapole.	25
2.11	Potentials of Different Stark Effects in an Electric Guide	26
2.12	A Straight Guide	27
2.13	Focusing Polar Molecules	28
2.14	A Curved Guide	29
2.15	Effective Potential in a Curved Guide	30
2.16	Trajectories in a Curved Guide	31
2.17	The Dipole Configuration in a Curved Hexapole Guide	32
2.18	Electric Fields and Effective Potentials inside a Dipole Configuration	32
2.19	The (2+1) REMPI Scheme	37
2.20	The Energy Levels of ND_3	40
3.1	Experimental Setup of the Velocity Filter	43
3.2	Thermal Velocity Distribution of ND_3 at Room Temperature	45
3.3	Angular Distribution of the Effusive Source	46
3.4	Coordinates and Dimensions of the Curved Guide	47
3.5	Simulated Transmission of the Hexapole Configuration	49
3.6	Simulated Transmission of the Dipole Configuration	50
3.7	Acceptance of the Hexapole Configuration	51
3.8	Wiley-McLaren Type Time-of-Flight Mass Spectrometer	52
3.9	AT Trace for Different Guide Voltages	53
3.10	Switching the Straight Segment	55

List of Figures

3.11 Bandpass Filter by Switching the Straight Segment	56
3.12 The Quasi-Continuous Bandpass Filter	57
3.13 AT Traces of the Hexapole and Dipole Configuration	58
3.14 Velocity Distributions of the Hexapole and Dipole Configuration	59
3.15 Guiding of different Rotational States of ND ₃	61
3.16 Simulated and Derived Velocity Distributions	63
3.17 Comparison of Simulated Velocity Distributions	64
3.18 Velocity Distribution for the <i>M</i> manifold of the 4 ₄ state	65
3.19 Stop Band Trajectories	66
3.20 Spectrum with Relative Transmission Probabilities	67
4.1 Overview of the Merged Beam Experiment	75
4.2 Rendering of the Two Guides	76
4.3 Photos of the Guide Segments	78
4.4 Fields in the Electric Guide	79
4.5 Transmission of the Electric Guide for Different Mass over Dipole Moment Ratios	80
4.6 Transmission of H ₂ O, CO [*] , CH ₃ F and H ₂ CO through the Electric Guide	81
4.7 Transmission of ND ₃ through the Electric Guide	82
4.8 Beam Profile of ND ₃	83
4.9 Fields in the Magnetic Guide	84
4.10 Measured Field Strength in the Magnetic Guide	85
4.11 Transmission of the Magnetic Guide for Different Mass over μ_{bohr} Ratios	86
4.12 Transmission of the Magnetic Guide	87
4.13 Stop Bands in the Magnetic Guide for Ne [*]	88
4.14 Beam Profile of Ne [*] in the Detection Region	88
4.15 The Detector for the Penning Ions	90
4.16 Signal Trace of the TOF-MS	91
4.17 Energy Resolution with the Pulsed TOF-MS	92
4.18 Velocity Distributions for Ne [*] with the Pulsed TOF-MS	93
4.19 The Detectors for the Reactant Beams	94
4.20 Trace of the mass-spectrometer	95
4.21 Reaction Rate for Different Relative Velocities	96
4.22 Rate Constants of Penning Ionization of ND ₃ by Metastable Ne [*]	98
4.23 Rate Constants of Penning Ionization of NH ₃ and ND ₃ by Metastable Ne [*]	99
4.24 Rate Constants of Penning Ionization of CH ₃ F by Metastable Ne [*]	100
4.25 Branching Ratios of the Penning Ionization of ND ₃ and NH ₃ by Metastable Ne [*]	102
4.26 Branching Ratio of the Penning Ionization of CH ₃ F by Metastable Ne [*]	104
4.27 The Reaction Guide	105



List of Tables

2.1	Zeeman Effect for Ne [*]	23
2.2	Rotational Constants of ND ₃	38
4.1	Performance of the Sources	77
4.2	Possible Reaction with the Current Apparatus	89

1 Motivation

I would risk to say that every scientific progress was made possible by, or at least was based on, the development of new experimental devices. This might be as simple as a stick whose shadow allowed early scientists to observe and quantify the motion of the sun in the sky, enabling timekeeping in scales from minutes to months [1] or a machine of unprecedented complexity like the Large Hadron Collider (LHC) at CERN. If those devices opened new doors of perception the human mind was always very eager to explore the unknown fields behind it. The aim of my thesis was the development of an experimental device which will enable us to observe chemical reactions at such low temperatures where these reactions could not be observed so far. As a chemical reaction demands that the reactants get so close to each other that they (somehow) interact, a chemical reaction can also be regarded as a collision of the reactants.

1.1 Cold Chemistry

As already mentioned our interest is in chemistry at low temperatures, cold chemistry. We are focused in particular on neutral-neutral reactions; therefore, the following review will neglect experiments performed with ions.

Within the cold chemistry community it has become consensual to label temperatures below 1 mK *ultracold* while temperatures between 1 mK - 2 K are called *cold* [2]. In the ultracold regime the collision energy becomes so low that the collision partners can be described by single-partial waves; these systems are clearly governed by the quantum physics. The cold regime on the other hand is still (at least partly) in the classical picture: The collision partners have to be described by many partial waves; it is therefore somehow more *chemical*.

1.1.1 Scientific Interest

In addition to the human urge to “boldly go where no one has gone before” [3], there is an intrinsic value in cold chemistry which makes its exploration worthwhile.

Astrochemistry



Figure 1.1: Small part of an interstellar cloud (emission nebula - NGC 6357), located some 8000 light years away. The image glows with the characteristic red of an H II region, and contains a large amount of ionized and excited hydrogen gas. The scale indicated the distances within the shown interstellar cloud. *European Southern Observatory - ESO* (CC BY 3.0)

Most of the chemistry (by volume) in the universe is happening at temperatures between 2.7 K - 100 K; inside interstellar clouds (IC) (see figure 1.1). Although those clouds have very low densities ($<10^6 \text{ cm}^{-3}$) astronomers have identified nearly 200 different molecules, consisting of up to 13 atoms [4], in the interstellar space. This indicates a very rich and active chemical environment. If we would understand more about the reaction rates of interstellar molecules we would learn much about the past and future of those interstellar clouds.

Long Range Interactions

As a low reaction temperature is equivalent to a very slow, gentle approaching of the reactants, reactions at low temperatures are much more sensitive to rather weak long-range interactions. Low energy collisions are therefore an ideal probe for such interactions.

At the Border to Quantum Mechanics

The lower the energy gets, the more dominant quantum-mechanical effects become. As the ultracold regime is clearly dominated by quantum physics, the cold regime is still in the middle between quantum mechanics and classical treatment¹. This means that effects originating from the nature of the wavefunction of the reactants might already occur in the cold regime, but classical approximations are still, at least partly, valid. On the other hand, this intermediate

¹ I distinguish here between the intermolecular situation and the description of the collision process. It should be clear that for the molecule itself quantum mechanics can never be neglected as it is necessary to understand the bonds within the molecule. But for the description of the collision process, quantum mechanics becomes important only from a certain collision energy on.

space between classical treatment and quantum mechanical behavior might be an interesting test bed for quantum-chemical computation models. If one of the many different approximations, needed to calculate molecular properties from pure quantum mechanical principles, is able to reproduce the measurements in the cold regime, it successfully spans the gap from purely classical to quantum mechanical.

1.1.2 State of the Art

The ultracold regime was first explored by atomic physicists when it became possible to stop atoms with laser-cooling and trap them in magnetic traps [5]. But as molecules, even if they are only made of two atoms, possess a much more complicated internal (energy-) structure [6], the very powerful technique of laser cooling fails for nearly all molecules, with the exception of SrF and YO [6–8]. The technique of optoelectrical cooling [9] was used by Zeppenfeld *et al.* to cool CH₃F down to 29 mK. Besides the molecules mentioned above, ultracold molecules are presently mainly produced from ultracold atoms via photoassociation (PA) or by fine-tuned Feshbach resonances. As this technique relies on ultracold atoms, and not all atoms can be laser-cooled up to now, this technique leads to very small molecules, presently only consisting of alkali metals [2].

In order to investigate more “chemically relevant” molecules at cold temperatures, there is another approach which starts with the desired molecule at room temperature and tries to cool or slow it down. This can either be done by buffer-gas cooling [10] or by using external fields to apply forces on the molecules. While optical fields are very rarely used [11–13], the use of magnetic and especially electric fields has proven to be very successful. The development of the Stark- and Zeemann decelerators [14–16] made it possible to slow down a variety of polar and paramagnetic molecules (and atoms); some can even be brought to a standstill in the laboratory frame. As the deceleration process is optimized for a certain state and for a certain velocity of the decelerated particles, the energy resolution and state purity are very high. A Stark decelerator was used to prepare the OH in order to investigate OH + Xe collisions by Gilijamse *et al.* [17]. They achieved a state purity of OH of practically 100% and an overall energy resolution in the collision energy of 13 cm⁻¹ in the range from 50 cm⁻¹ to 400 cm⁻¹. The bimolecular reaction OH + NO was investigated by Kirste *et al.* in the range from 70 cm⁻¹ to 300 cm⁻¹ under similar conditions [18]. In both experiments the excellent energy resolution together with the high state purity made it possible to determine state-to-state inelastic cross-sections.

Unfortunately the acceptance of the decelerators declines the more the original sample of particles is slowed down. Although the phase space density stays constant through the deceleration process, the total number of decelerated particles declines. Due to the insufficient collision probability, it has been impossible up to now to perform crossed beam experiment with decelerators if the collision energy gets below 50 cm⁻¹ \approx 70 K; although it is possible to produce much slower beams.

In addition to the use of the decelerators to perform crossed-beam experiments, they can also be used to prepare molecules for loading traps. By subsequently sympathetic [2] or evapo-

rative [19] cooling, those trapped molecules could be further cooled down (20 mK and 5 mK respectively). Collisions of such trapped species among themselves or with the background gas or interaction radiation could then be studied [20].

Although some of the techniques mentioned above can prepare cold molecules, there is still a surprising lack of experimental approaches to perform chemistry from several tens of K down into the cold regime. Only a few experiments have been able to observe chemical reaction of neutrals in this temperature range. The most productive concerning the number of investigated reactions was the CRESU apparatus [21, 22], which studied about 50 chemical reactions, mainly reactions with radicals, in the temperature range 7 K - 160 K. Another experiment was performed by Willey *et al.* which determined the cross sections of the reactions $\text{NH}_3 + \text{H}_2$ and $\text{NH}_3 + \text{He}$ in the range 10 K - 40 K by investigating the pressure broadening of the $J_K = 1_1, 2_2$ and 3_3 inversion transitions of NH_3 [23].

In crossed beam experiments at with variable angles Toennies *et al.* could investigate the reaction of H_2 with rare gases down to 5 K [24]. Crossing beams of O_2 and CO with a beam of H_2 at 12.5° allowed Costes *et al.* to measure the cross section of the rotational excitation of O_2 and CO by H_2 down to 3 K [25, 26]. Cryogenic helium buffer-gas cooling enabled Singh *et al.* to measure the $\text{Li} + \text{CaH} \longrightarrow \text{LiH} + \text{Ca}$ reaction at 1 K [27].

A recent approach combining Stark deceleration, magnetic trapping and cryogenic buffer gas cooling was realized by Ye *et al.* [28]. In this approach a beam of OH is Stark decelerated and subsequently trapped. A second velocity-selected beam of cryogenically cooled ND_3 molecules is overlapped with the trapped OH. The total trap loss cross section at a mean collision energy of 5 K could be measured. In addition the influence of an external electrical field onto the cross section of the polar reactants was investigated.

A new idea to perform chemical reaction appeared when the manipulation of the motion of neutrals, exploiting the Stark and Zeeman effect, reached a level of control where it became possible to merge two beams of neutral particles. Due to the so-achieved parallel movement of the reactants, low collision energies can be achieved even for fast beams. The main part of this thesis deals with the realization of this idea. The power of this approach has been shown in 2012 by Henson *et al.* by investigating the Penning ionization of H_2 by metastable He^* down to 10 mK [29].

Yet another approach to produce dense cold beams of neutral has appeared, although no reactions have been investigated so far. In August 2013, using a *centrifuge decelerator*, Rempe *et al.* produced continuous beams of CH_3F , CF_3H , and CF_3CCH between 15 m/s and 200 m/s (1 K to 150 K) [30]. As this technique is able to transmit 20% of the undecelerated sample, it can achieve intensities of several $10^9 / \text{mm}^2\text{s}$. The use of this technique in collision experiments is therefore very promising.²

² There are at least two other approaches which can produce samples of cold neutral molecules. The *rotating nozzle* moves the source of a supersonic expansion backwards. If the velocity of this backwards movement is as high as the forward movement of the beam, a sample is produced which is practically at rest in the laboratory frame [31, 32]. The second technique utilizes well-prepared collisions in which one of the collision partners ends up with a zero velocity in the laboratory frame [33]. Although both approaches are very generally applicable, they have not yet been used successfully in collision experiments.

2 Introduction

2.1 Collision Kinematics

2.1.1 Collision Energies

The simplest reference frame to describe the relative motion of two particles is their center-of-mass frame (CM). Within this frame, the center-of-mass of the system is at rest and therefore the only relevant direction is the connecting line between the two particles. The problem is reduced to one distance \mathbf{r} (relative distance of the two particles) and one velocity \mathbf{v} (their relative velocity), which simplifies the description of the collision process. The definitions of the lab frame and CM frame are shown in figure 2.1. The relative distance \mathbf{r} and the relative velocity \mathbf{v} of the collision partners are defined as

$$\mathbf{r} = \mathbf{r}_1 - \mathbf{r}_2 \quad (2.1)$$

$$\mathbf{v} = \mathbf{v}_1 - \mathbf{v}_2, \quad (2.2)$$

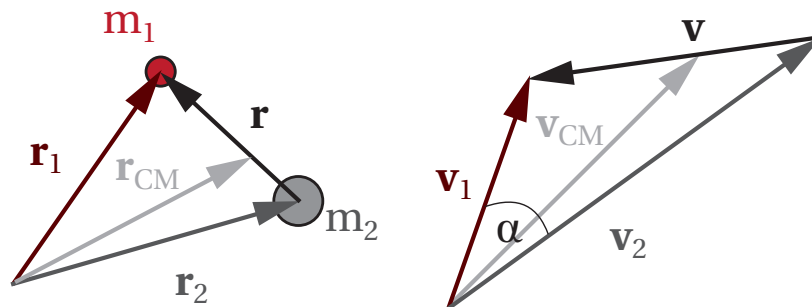


Figure 2.1: Definitions of the coordinates \mathbf{r}_i and velocities \mathbf{v}_i in the laboratory and the center-of-mass frame.

Chapter 2. Introduction

where \mathbf{r}_i and \mathbf{v}_i are the positions and velocities of particles with mass m_i in the laboratory frame. In order to describe the kinematics in the CM frame, the definition of the total mass M and the reduced mass μ are very useful:

$$M = m_1 + m_2 \quad (2.3)$$

$$\mu = \frac{m_1 m_2}{M}, \quad (2.4)$$

with the particle masses m_i . The position and velocity of the center-of-mass in the laboratory frame, \mathbf{r}_{CM} and \mathbf{v}_{CM} , are

$$\mathbf{r}_{\text{CM}} = \frac{m_1 \mathbf{r}_1 + m_2 \mathbf{r}_2}{M} \quad (2.5)$$

$$\mathbf{v}_{\text{CM}} = \frac{m_1 \mathbf{v}_1 + m_2 \mathbf{v}_2}{M}. \quad (2.6)$$

With equations 2.1-2.6 one can transform the CM frame back into the laboratory frame.

$$\mathbf{r}_1 = \mathbf{r}_{\text{CM}} + \frac{\mu}{m_1} \mathbf{r} \quad (2.7)$$

$$\mathbf{r}_2 = \mathbf{r}_{\text{CM}} - \frac{\mu}{m_2} \mathbf{r} \quad (2.8)$$

$$\mathbf{v}_1 = \mathbf{v}_{\text{CM}} + \frac{\mu}{m_1} \mathbf{v} \quad (2.9)$$

$$\mathbf{v}_2 = \mathbf{v}_{\text{CM}} - \frac{\mu}{m_2} \mathbf{v} \quad (2.10)$$

As the kinetic energy T of the system must be the same in both frames, one can apply the transformations 2.7 - 2.10 and obtain:

$$T = T_1 + T_2 \quad (2.11)$$

$$= \frac{m_1}{2} \mathbf{v}_1^2 + \frac{m_2}{2} \mathbf{v}_2^2 \quad (2.12)$$

$$= \frac{M}{2} \mathbf{v}_{\text{CM}}^2 + \frac{\mu}{2} \mathbf{v}^2, \quad (2.13)$$

In the CM frame we can separate the kinetic energy of the center-of-mass $T_{\text{CM}} = \frac{M}{2} \mathbf{v}_{\text{CM}}^2$ from the relative kinetic, i.e. the *collision energy* T_c .

$$T_c = \frac{\mu}{2} \mathbf{v}^2 \quad (2.14)$$

Described with the laboratory frame velocities \mathbf{v}_i , the collision energy T_c is given by

$$T_c = \frac{\mu}{2} (v_1^2 + v_2^2 - 2v_1 v_2 \cos \alpha), \quad (2.15)$$

where v_i are the magnitudes of the particle velocities in the lab frame and α is the angle between the beams, as shown in figure 2.1. Equation 2.15 shows that there are two ways to reduce the collision energy. Most obviously reducing v_1 and v_2 will yield a reduced collision energy. This approach is followed by using decelerators in crossed beam experiments. The second way to reduce T_c is by reducing α . If the two beams move parallel, i.e. $\alpha = 0$, the collision energy depends only on the velocity difference of the two beams:

$$T_{c,\parallel} = \frac{\mu}{2} (v_1 - v_2)^2. \quad (2.16)$$

In this equation one can see the advantage of merged beam experiments. In a merged beam experiment the relative velocity v (*collision velocity*) can be easily scaled by changing the particles velocity and, in contrast to crossed beam setups, can reach zero, even for particles with very high laboratory frame velocities.

2.1.2 Energy Resolution in Merged Beam Experiments

Though it might be theoretically possible to achieve a collision energy of zero for particles that have the same velocity and move perfectly parallel, this situation will be impossible to achieve in real experiments. The particles in the experiments do not come alone but in beams with many million other particles. These beams will have a certain spread in velocity and angle, so that the perfect overlap in angle and velocity cannot be achieved for beams. But how close can we get to the zero energy conditions?

The spread in the collision energy ΔT_c caused by a velocity spread Δv_i in one of the two beams can be calculated by taking the partial derivative of equation 2.14. From this derivative one can see that a change in velocity Δv_i will change the collision energy by ΔT_c . Taking for instance v_1 , we get

$$\Delta T_c^{v_1} = \mu (v_1 - v_2 \cos \alpha) \Delta v_1. \quad (2.17)$$

The same equation, with interchanged subscripts, holds for the dependence of the energy spread from the beam 2. The multiplier of Δv_i on the right hand side of equation 2.17 is called the *energy deamplification* [34]. For merged beam experiments ($\alpha \rightarrow 0$ therefore $\cos \alpha \approx 1$) the energy deamplification is extremely convenient, as the main purpose of merged beam experiments is the investigation of low collision energies. And exactly for low collision energies ($v_1 \approx v_2$) the uncertainty in the collision energies is decreased substantially.

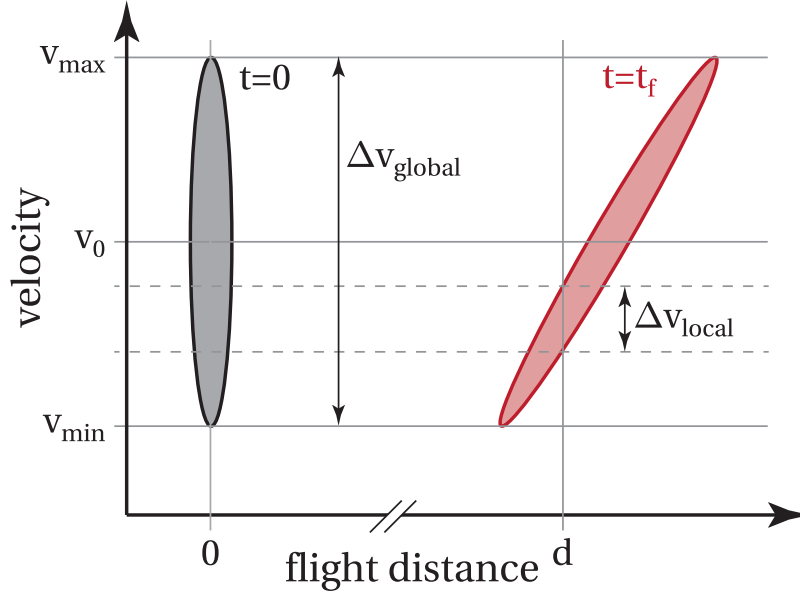


Figure 2.2: Temporal evolution of the phase space distribution of a package of freely moving particles.

For the spread in angle $\Delta\alpha$, one obtains an uncertainty in collision energy of

$$\Delta T_c^\alpha = \mu v_1 v_2 \sin \alpha \Delta \alpha. \quad (2.18)$$

In the case of merged beams ($\alpha = 0 \rightarrow \sin \alpha = 0$), this uncertainty vanishes as well. But equation 2.18 is only true if all particles originate from the same point, so that the trajectories of particles with different angles do not cross. Depending on the given setup of the merged beam experiment, this assumption might not be true.

Energy Resolution in Merged Beams Experiments with Pulsed Beams

The energy resolution as mentioned above is formulated for continuous beams. If the beams are generated by a pulsed source and the opening time of the source is much shorter than the flight time of the reactants, the energy resolution is further increased. This addition in resolution is achieved by the correlation of the velocity and position in the phase space of freely traveling particles [35]. Figure 2.2 illustrates this correlation. When the source opens at $t = 0$ the packet of particles is highly confined in position and has a certain velocity spread (black ellipse). After some flight time, t_f , the fast particles will be further away than the slow ones, causing the ellipse in figure 2.2 to tilt. Although the overall velocity spread Δv_{global} has not been reduced, the local velocity spread Δv_{local} at position d after the flight time t_f is significantly reduced. Depending on the geometry of the experiment, the local velocity

standard deviation can be reduced by several orders of magnitude.

2.1.3 Reaction Rate and Cross Section

The reaction rate is defined as the change over time of the product number density n_P due to the presence of the reactant densities n_1 and n_2 .

$$\frac{dn_P}{dt} = k(E_{coll}) n_1 n_2, \quad (2.19)$$

where $k(E_{coll})$ is the energy-dependent rate constant with the unit $\frac{\text{volume}}{\text{time}}$. If the density of the reactants is not constant over the reaction volume, the product of the densities has to be integrated over the reaction volume V .

$$n_1 n_2 = \frac{1}{V} \int n_1(x, y, z) n_2(x, y, z) dV \quad (2.20)$$

In case of a constant volume equation 2.19 can be written for the total number of reaction products N_P and reactants $N_{1,2}$:

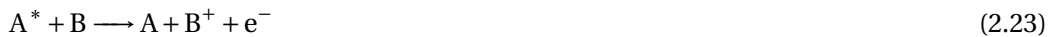
$$\frac{dN_P}{dt} = k(E_{coll}) \frac{N_1 N_2}{V}. \quad (2.21)$$

Equation 2.19 and 2.21 are based on the assumption that the yield of the reaction is so small that the initial densities can be assumed to be constant. The cross section is connected to the rate constant by the relative velocity of the reactants v_{rel} ,

$$\sigma = \frac{k(E_{coll})}{v_{rel}}. \quad (2.22)$$

2.2 Penning Ionization

An electronically excited atom or molecule A^* can ionize another atom or molecule B if the internal energy of A^* is higher than the ionization potential (IP) of B.

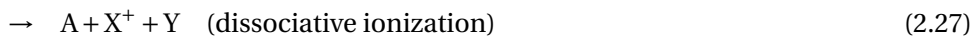
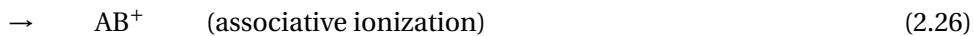
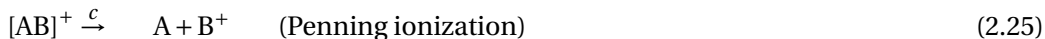


According to Hotop and Niehaus the Penning ionization (PI) is an electron rearrangement reaction where an outer-shell electron of B is transferred to the inner-shell vacancy of the excited A^* , leading subsequently to the ejection of the excited electron of A [36]. In an orbital model the ionization probability will therefore depend on the overlap of the orbitals which are part of the electron transfer. One could expect to have the highest probability at those distances between A and B where the relative motion is slowest and for those directions along which the density of the exchange orbitals are highest [37].

Described as a reaction, the PI can be described as [38]



where $[AB]^*$ and $[AB]^+$ are two collision intermediates. The second intermediate can undergo a third reaction step *c*:



In the last two pathways the molecule B is dissociated into X^+ and Y.

The reaction step *a* can be described by the potential energy surface (PES) V_0 of the initial system $A^* + B$. The reaction step *b* is considered to be irreversible, which gives rise to an imaginary potential Γ [39]. The decay of the complex $[AB]^*$ is therefore described by the optical potential $V_0 - i\Gamma/2$ which combines step *a* and *b*. The future of the ionic complex $[AB]^+$, step *c*, can be calculated from its PES V_+ .

In principle this PES can be calculated *ab initio*, although the model becomes more complicated if B (or A) is a molecule and if the spatial degeneracy is broken by the approaching of A and B.

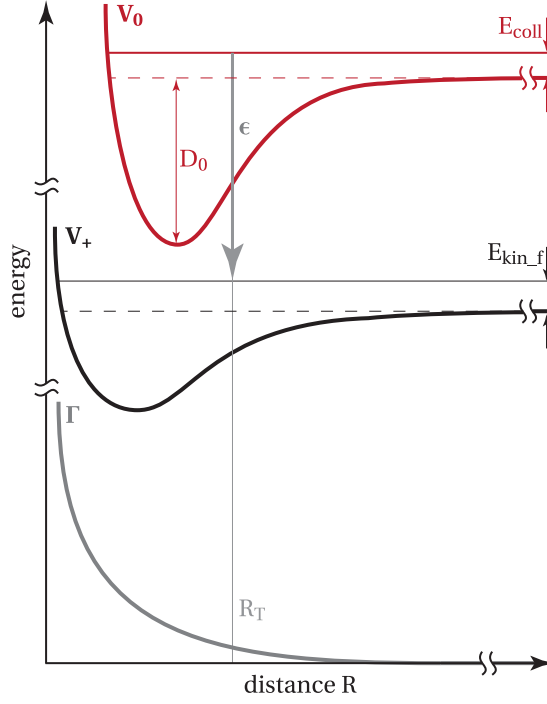


Figure 2.3: Potential curves of the Penning ionization

2.2.1 Cross Section of the Penning Ionization

In order to get an estimate on the energy-dependence of the cross section of the PI, we take a look at the PI process on a one-dimensional PES in a classical treatment¹. The Penning ionization probability $P(R)$ at a certain distance R of the reactants for a system with an angular momentum l can be described as

$$P_l(R) = 1 - \exp\left(-\int_{R_l}^{\infty} \frac{\Gamma(R)}{\hbar v_l(R)} dR\right), \quad (2.29)$$

with the local velocity

$$v_l(R) = \sqrt{\frac{2}{\mu} \left(E_{coll} + V_0(\infty) - V_0(R) - \frac{l(l+1)\hbar^2}{2\mu R^2} \right)}, \quad (2.30)$$

where μ is the reduced mass. The collision energy E_{coll} and the PES of the system before the ionization V_0 can be seen in figure 2.3. R_l is the l -dependent turning point on $V_0(R)$ and therefore the solution of $v_l(R_l) = 0$. In order to simplify this theoretical treatment only one reaction coordinate (R) is considered. In case of a Penning ionization of a molecule by a

¹The derivation of the cross section in this section follows very closely the argumentation of A. Niehaus [40, p.408]

Chapter 2. Introduction

metastable atom, the pathway on the multidimensional PES has to be considered. The total cross section σ for a Penning ionization is with equation 2.30

$$\sigma(E_{coll}) = \frac{\pi \hbar^2}{2\mu E_{coll}} \sum_{l=0}^{\infty} (2l+1) P_l. \quad (2.31)$$

Assuming large values of l , equation 2.31 can be turned into an integral over the impact parameter b by the substitution $b\sqrt{2\mu E_{coll}}/\hbar = (l + \frac{1}{2})$.

$$\sigma(E_{coll}) = 2\pi \int_0^{\infty} P(b) b db \quad (2.32)$$

The energy dependence of equation 2.31 and 2.32 comes in via the energy-dependent local velocity v_l and turning point R_l . As the total cross section depends from V_0 and Γ and is independent from V_+ , a precise knowledge of the product PES V_+ is not necessary. As long as there are enough l -values participating in the collision, quantum effects in the cross section should be averaged out and the results of this classical treatment should be accurate.

In order to get a first overview over the features of the cross section, one can derive the dependency of the cross section for two different energy regimes. If the collision energy E_{coll} is much smaller than the well depth D_0 of the potential V_0 ($\frac{E_{coll}}{D_0} \ll 1$), the attractive part of the potential V_0 will dominate the reaction process. On the other hand the attractive part can be neglected if the collision energy E_{coll} is much higher than D_0 ($\frac{E_{coll}}{D_0} \gg 1$).

Low Collision Energies ($\frac{E_{coll}}{D_0} \ll 1$)

If the impact parameter b is raised from zero, the turning point $R_c(b)$, where $v_l(R_c) = 0$, jumps at a certain value b_c from very low values at the centrifugal barrier to very large values at the rotational barrier of the effective potential. For large R (i.e. $b > b_c$) the Penning ionization probability P is very low, therefore values above b_c can be neglected in equation 2.32.

The trajectories for $b < b_c$ are, on the other hand, mainly determined by the attractive forces and rather independent of b . This simplifies the cross section for $\frac{E_{coll}}{D_0} \ll 1$ to

$$\sigma(E_{coll}) \approx 2\pi \int_0^{b_c} P(b) b db \approx \pi \bar{P} b_c^2, \quad (2.33)$$

where \bar{P} is the average, assumed energy-independent ionization probability. The energy dependence of b_c is determined by the long-range attractive forces of V_0 and can be estimated as $b_c \propto E_{coll}^{-\frac{1}{s}}$ if we assume $V_0 \propto R^{-s}$ for large R . Therefore we expect the energy dependence

of the Penning ionization cross section for $\frac{E_{coll}}{D_0} \ll 1$ to be

$$\sigma(E_{coll}) \propto E_{coll}^{-\frac{2}{s}}. \quad (2.34)$$

Using equation 2.22 and $v_{coll} \propto \sqrt{E_{coll}}$ we expect the rate constant k to be

$$k(E_{coll}) \propto E_{coll}^{\frac{s-4}{2s}}. \quad (2.35)$$

High Collision Energies ($\frac{E_{coll}}{D_0} \gg 1$)

In the case of $\frac{E_{coll}}{D_0} \gg 1$ the attractive part of V_0 can be neglected and be approximated by a purely repulsive potential. If we assume further a small ionization probability per collision, we can approximate

$$P(b) \approx 2 \int_{R(b)}^{\infty} \frac{\Gamma(R)}{\hbar v(b, R)} dR. \quad (2.36)$$

The cross section becomes an integral over the distance

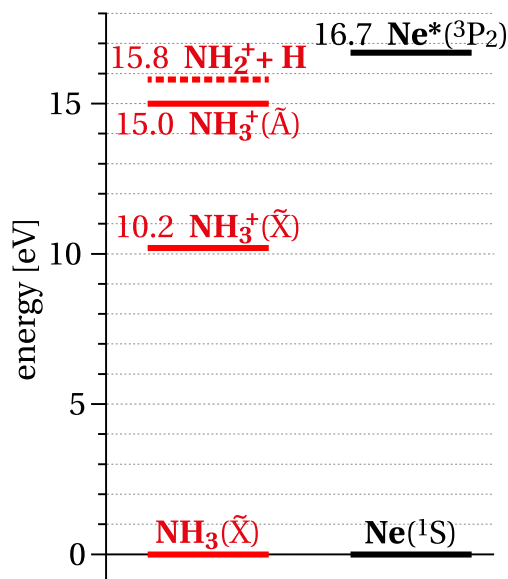
$$\sigma(E_{coll}) \approx \int_{R(0)}^{\infty} \frac{4\pi R^2 \Gamma(R)}{\hbar \sqrt{\frac{2}{\mu} [E_{coll} - V_0(R)]}} dR. \quad (2.37)$$

If the repulsive potential is approximated by $V_0 = C \exp(-\frac{R}{F})$ and the optical potential by $\Gamma(R) = \hbar A \exp(-\frac{R}{B})$, with $\frac{R}{B} \gg 1$ we obtain a cross section of

$$\sigma(E_{coll}) \approx 2A \left(\frac{\mu}{2B} \right)^{\frac{1}{2}} (BF\pi)^{\frac{3}{2}} \left[\ln \frac{C}{E_{coll}} \right]^2 \left[\frac{E_{coll}}{C} \right]^{\frac{F}{B} - \frac{1}{2}}. \quad (2.38)$$

Consequently the rate constant in the high energy limit is expected to be

$$k(E_{coll}) \propto \left[\ln \frac{C}{E_{coll}} \right]^2 \left[\frac{E_{coll}}{C} \right]^{\frac{F}{B}}. \quad (2.39)$$

Figure 2.4: Energies of NH_3^+ , $\text{NH}_2^+ + \text{H}$ and metastable Ne^*

2.2.2 Penning Ionization of Ammonia by metastable Ne^*

There is very little experimental data available on the Penning ionization of ammonia by metastable neon. To my knowledge there are only two studies: Čermák [41] determined that this Penning ionization leads to electrons with two very distinguished energies. Ben Arfa *et al.* [42] assigned these energies to the $\text{X } ^2\text{A}'_1$ ground state and the excited $\text{A } ^2\text{E}$ state of the NH_3^+ ion.

The removal of one electron from the $3a_1$ orbital of NH_3 produces the ground state of NH_3^+ , while a loss of one $1e$ electron leads to the observed excited state. The $3a_1$ orbital is oriented along the symmetry axis of ammonia; the $1e$ orbital along the N–H bonds. The probability of producing an ammonia ion in the ground state or the excited state should therefore depend on the orientation of the molecule and the metastable Ne^* at the moment of ionization. An attack along the symmetry axis of NH_3 is more likely to yield the $\text{X } ^2\text{A}'_1$ ground state, while a sideways collision will more probably produce the excited $\text{A } ^2\text{E}$ state of NH_3^+ .

The $\text{X } ^2\text{A}'_1$ state is stable but the Jahn-Teller distortion of the $\text{A } ^2\text{E}$ state leads to an $\approx 80\%$ dissociation probability into NH_2^+ fragments [43].

Ben Arfa *et al.* measured this ratio $[\text{NH}_2^+]/[\text{NH}_3^+]$ in the energy range from 0.04 meV to 0.4 meV. They also determined the total cross section of the Penning ionization of NH_3 by the metastable Ne^* in the same energy range [42].

The measured ratio increases for increasing collision energies while the cross section decreases.

Unfortunately there are presently no PES available for the ND_3-Ne^* or NH_3-Ne^* complex. But the chemically similar $\text{H}_2\text{O}-\text{Ne}^*$ complex has a 400 meV deep well along the O-lone pair... Ne^* coordinate, while there is barely any minimum along the O–H... Ne^* coordinate [44, 45]. With

the arguments of previous section (2.2.1 *Cross Section of the Penning Ionization*) the rate constant along the lone-pair bond can be approximately described by the low energy approximation (equation 2.2.1) for temperatures below 1000 K, while the rate constant assigned to the N–H...Ne^{*} bond should show the behavior predicted by the high energy approximation of equation 2.39.

2.3 Stereochemistry

Stereodynamics describes the influence of the orientation of the reactants on a reaction. The reactants approach each other on a complicated *potential energy surface* (PES). Different routes on this surface indicate different orientations during the reaction, and it is generally believed that the reactants follow the *minimum-energy path* (MEP) [46]. For reactions that can take different routes on the PES, this assumption must lead to the conclusion that lower collision energies, or equivalently a slower approach, will favor the reaction channel that has a steeper MEP. This, in turn, must lead to a temperature dependent branching ratio for the reaction products. Such effects have been studied in detail at high collision energies, but few studies have been performed at collision energies below 1 K. The reaction $\text{KRb} + \text{KRb} \longrightarrow \text{K}_2 + \text{Rb}_2$, for example, had been investigated at ultracold temperatures. The reaction rate of this reaction is suppressed by nearly two orders of magnitude when the KRb molecules approach each other in a side-by-side fashion [47].

2.3.1 Stereochemistry of the Penning Ionization

In several previous studies the stereochemistry of the Penning ionization of polyatomic molecules at collision energies in the range of from 30 meV to 500 meV (230 K to 3900 K) has been studied [37, 38, 48–56]. The findings of these studies can be summarized as follows: There is an agreement between theory and experiment that the ionization step is vibrationally adiabatic and that the vibrational populations in the ion are governed by the Franck-Condon overlap with the neutral [38, 48, 49]. When the collision energy is high compared to the depth of the MEP well, the reaction is insensitive to the topology of the PES [37]. The stereochemistry in that case is determined by the instantaneous orientation of the molecule relative to the direction of the incoming metastable atom, and the branching ratio follows from the cones of acceptance for the different channels. In a spherical symmetric molecules like CH_4 , the branching ratios for the formation of CH_4^+ vs. any of the CH_n^+ , for example, are completely independent of temperature [50]. The example of the previous section (sec. 2.2.2), Penning ionization of the non-spherical NH_3 by Ne^* , already revealed a temperature dependency in the branching ratio of NH_3^+ vs. NH_2^+ [42]. A markedly change in branching ratio as a function of temperature has been observed for other non-spherical molecules as well [51–56]. As the speed of approach is reduced, the molecule starts to funnel along the MEP towards the energetically favored geometry of the Rg^* -molecule complex.

2.4 Manipulation of Neutrals

In order to perform collision studies with high energy resolution or at low collision energies, a way to control the motion of the collision partners is needed. According to Newton's first law of motion, the only way to change the motion of a particle is through the action of a force on the particle. Gravity provides the most general force as it acts on all particles with a mass, but it is on the other hand also the weakest of the four fundamental interactions. An ammonia molecule with a "room-temperature" velocity of about $v = \sqrt{2 \frac{k_b T}{m}} \approx 500 \text{ m/s}$ would need to travel nearly 13 km up in the earth's gravity field to come to a standstill. The simple idea of a "molecular fountain" will therefore not work for reasonably sized laboratories on Earth using particles with room temperature velocities.

As two of the three other fundamental interactions, the weak and the strong nuclear force, have ranges limited to the nucleus, we are left with only one fundamental interaction, the electromagnetic force². Especially the electrostatic part of this interaction, the Coulomb force, provides an easy and powerful way to manipulate charged particles. If the above mentioned ammonia would have a charge of $1e$, it could be stopped by a potential of only 25 mV.

Unfortunately it is much more demanding to apply forces on neutral particles which can change the motion significantly. In our experiments we will use the Stark and the Zeeman effect to create forces on our neutral collision partners.

2.4.1 Stark Effect

The Stark³ effect describes the energy shift W_S of a polar particle due to an external electric field. Figures 2.5 and 2.7 show this energy shift for selected states of different molecules.

The origin of this shift is the presence of a dipole moment μ due to unsymmetric charge distribution of a particle. In an electric field \mathbf{E} a polar particle has a potential energy W_S which depends on the orientation of the electric dipole moment μ relative to the external field \mathbf{E} .

$$W_S = -\mu \mathbf{E} \quad (2.40)$$

The Stark effect can be exploited to manipulate the motion of neutral molecules via inhomogeneous fields. The gradient of the potential energy will generate a force on the molecule.

$$\mathbf{F}_s = -\nabla W_s \quad (2.41)$$

² If one is not focused on the manipulation of the particles in free space, mechanical devices (e.g. paddle wheel slowers) can be used [57]. The forces of particles colliding with solids are caused by the electromagnetic force as well.

³ Unfortunately this effect was named after Johannes Stark (1874-1957). Not only his strong support for the NSDAP, the German fascist party, and his fanatic belief in the cruel and inhumane fascist ideology makes it difficult to honor him. Even if we let politics out of science, his understanding of science in general was insane. Already in the twenties of the 20th century, long before the Nazis came to power, he tried to implement the "german (aryan) physics" in contrast to the "jewish physics", which he considered to be the quantum theory and the relativity theory [58].

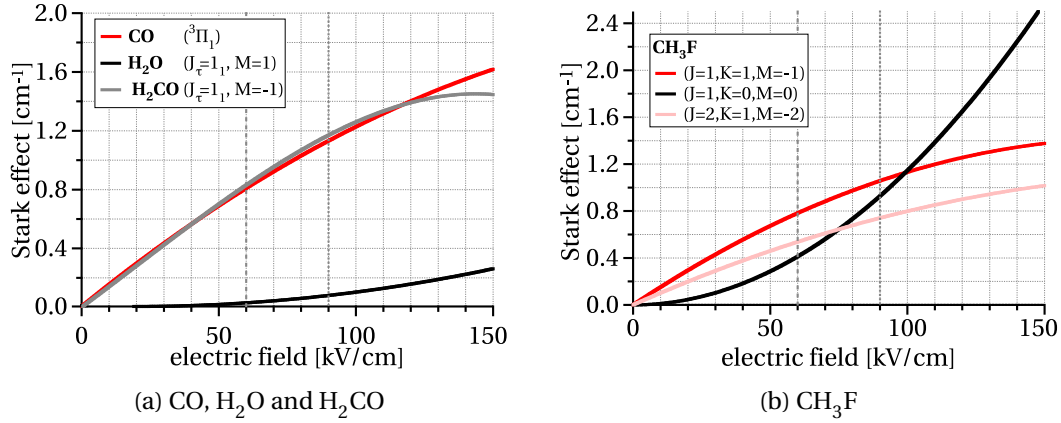


Figure 2.5: **Stark effect of selected states of H_2O , CO , H_2CO and CH_3F .** The vertical lines indicates the maximum electric field for the $\pm 8\text{kV}$ (left) and the $\pm 12\text{kV}$ in the electric guides of our experiments.

Depending on the orientation of the dipole moment relative to the electric field, a particle either gains or loses energy in rising electric fields (see graph 2.7). The so-called low-field-seeking (lfs) states are attracted by low field regions, while the high-field-seekers (hfs) will move towards higher fields. Therefore the Stark effect provides the possibility to change the motion of neutral polar molecules in free space [59]. As it is possible to create a three-dimensional field minimum in free space, one can even trap polar molecules in lfs states with static electric fields [60]. For hfs states this is only possible with time-dependent fields [61].

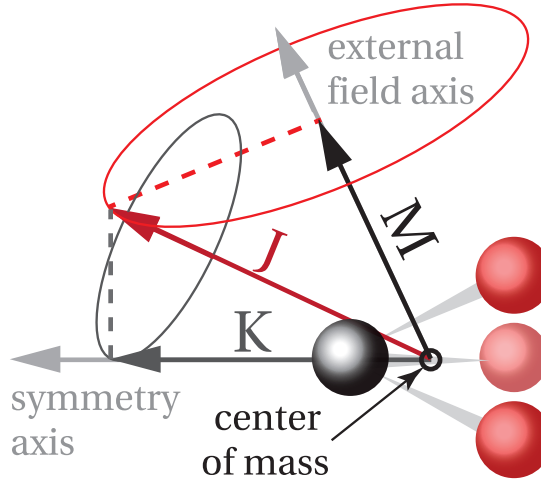
Linear and Quadratic Stark Effect

The dipole moment μ is permanently present if the positive and negative charges of a molecule are not centered at the same point. The permanent electric dipole moment of a molecule depends therefore on its geometry and can be easily calculated if the structure of the electron shell and the positions of the nuclei are known. This permanent dipole moment gives rise to the *linear Stark effect*.

A dipole moment can as well be induced by an external electric field. Depending on the polarizability α , the particle in an external electric field E will induce a dipole moment of

$$\mu_{ind} = \alpha E. \quad (2.42)$$

The energy shift due to an induced dipole moment is called *quadratic Stark effect* as in this case the Stark energy rises quadratically with the electric field. For polar molecule the quadratic Stark effect is orders of magnitude weaker than the linear Stark effect. For molecules displayed in figures 2.5 and 2.7, the quadratic Stark effect at 100kV/cm is at least 10^3 weaker than the linear Stark effect [62]. The forces induced by the quadratic Stark effect are therefore negligibly small. Thus I will focus on the Stark effect caused by a permanent dipole moment.

Figure 2.6: Definition of the rotational quantum numbers J , K and M .

Rotation and the Effective Dipole Moment

If the polar molecule is rotating, all components of the dipole moment orthogonal to its total angular momentum \mathbf{J} are canceled. The residing component of the dipole moment parallel to \mathbf{J} is $\langle \boldsymbol{\mu}_J \rangle$. As the angular momentum \mathbf{J} is in precession around the external field axis, which we define as the z-axis \mathbf{z} , $\langle \boldsymbol{\mu}_J \rangle$ is further reduced by the projection of \mathbf{J} onto the external field axis. In the case of a symmetric top molecule, the dipole moment has to be along the symmetry axis of the molecule. The projection of the total angular momentum \mathbf{J} on the symmetry axis of the molecule is the quantum number K (see graph 2.6). The quantum mechanical projection leads to

$$\langle \boldsymbol{\mu}_J \rangle = \frac{K}{\sqrt{J(J+1)}} \boldsymbol{\mu} \mathbf{e}_J, \quad (2.43)$$

where μ is the magnitude of the dipole moment and \mathbf{e}_J is the unit vector along \mathbf{J} . The projection of \mathbf{J} onto an external field axis is labeled by the quantum number M , so that the first order perturbation matrix element of the Stark operator of a polar molecule in an external field \mathbf{E} can be described as

$$W_S = -\frac{MK}{J(J+1)} \mu E, \quad (2.44)$$

where E is the magnitude of the external electric field.

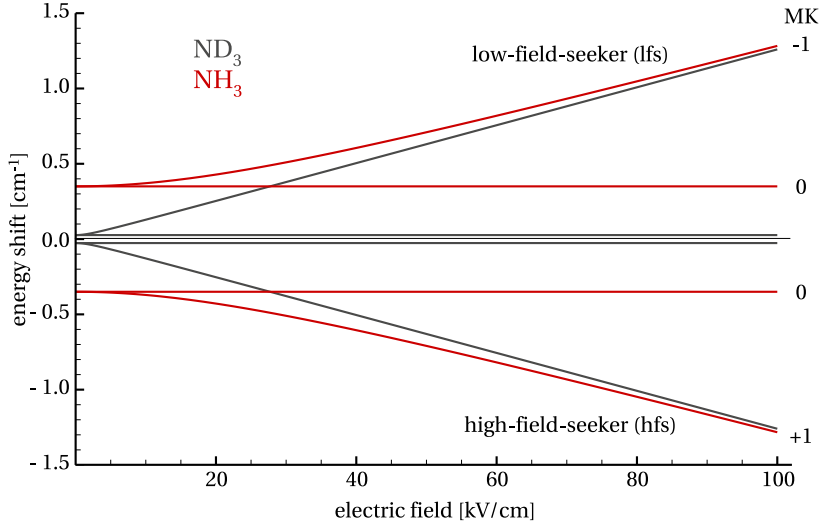


Figure 2.7: First order Stark shift for the $J_K = 1_1$ state of ammonia in electric fields.

Stark Effect of the Ammonia Molecule

Due to its symmetry the ammonia molecule possesses an inversion splitting W_{inv} in its ground state. Both components of the inversion splitting have opposite parities and they are coupled by the Hamiltonian of the linear Stark effect [63]. Taking this into account the first order approximation of the Stark shift of ammonia is given by

$$W_S = \pm \sqrt{\left(\frac{W_{inv}}{2}\right)^2 + \left(\frac{MK}{J(J+1)}\mu E\right)^2} \mp \left(\frac{W_{inv}}{2}\right). \quad (2.45)$$

The different tunnel probabilities of H and D through the potential barrier between the two configurations of the ground state lead to different values of the inversion splitting W_{inv} for NH_3 and ND_3 .

$$W_{inv}(NH_3) = 0.79 \text{ } ^1/\text{cm} \quad [64] \quad (2.46)$$

$$W_{inv}(ND_3) = 0.053 \text{ } ^1/\text{cm} \quad [65] \quad (2.47)$$

The rotational state has a small influence on the inversion splitting [66], but its magnitude (less than $0.03 \text{ } ^1/\text{cm}$ for ND_3 in the observed rotational states) was negligible in the scope of our experiment. Graph 2.7 shows the Stark effect for NH_3 and ND_3 . In order to keep the electrode design simpler and to avoid switching the electrode voltages, we have only worked with lfs states.

2.4.2 Zeeman Effect

The Zeeman Effect is the magnetic analogue of the Stark effect. Analog to the electric dipole moment a particle can possess a permanent magnetic moment. The magnetic moment is either an intrinsic property of the particle, i.e. the spin, or it is created by the motion of a charge, e.g. the orbiting motion of an electron.

The spin magnetic moment is

$$\boldsymbol{\mu}_s = -2 \frac{\mu_B}{\hbar} \mathbf{s}, \quad (2.48)$$

where $\mu_B = e\hbar/2mc$ is the Bohr magneton. If a charged particle with a charge $-qe$ is orbiting with angular momentum \mathbf{l} , its orbital magnetic moment is

$$\boldsymbol{\mu}_l = -q \frac{\mu_B}{\hbar} \mathbf{l} \quad (2.49)$$

If both momenta are taken into account, the magnetic moment of an electron is

$$\boldsymbol{\mu}_e = \frac{\mu_B}{\hbar} (2\mathbf{s} + \mathbf{l}) \quad (2.50)$$

In an atom with Russell-Saunders coupling, the total angular momentum \mathbf{J} can be described as

$$\mathbf{J} = \mathbf{L} + \mathbf{S}, \quad (2.51)$$

where

$$\mathbf{L} = \sum \mathbf{l}_i \quad (2.52)$$

$$\mathbf{S} = \sum \mathbf{s}_i, \quad (2.53)$$

so that the total magnetic moment of an atom with Russell-Saunders coupling is

$$\boldsymbol{\mu} = -\frac{\mu_B}{\hbar} (2\mathbf{S} + \mathbf{L}) = -\frac{\mu_B}{\hbar} (\mathbf{J} + \mathbf{S}), \quad (2.54)$$

The Zeeman effect is the energy shift of a particle with a magnetic moment $\boldsymbol{\mu}$ in an external magnetic field \mathbf{B} , which depends on the orientation of the magnetic moment to the external

Chapter 2. Introduction

field axis.

$$W_Z = -\boldsymbol{\mu}\mathbf{B} \quad (2.55)$$

or

$$W_Z = -\mu_z B, \quad (2.56)$$

if we define the direction of \mathbf{B} as the z-axis and B as the magnitude of \mathbf{B} . As J and its projection to the external axis M are good quantum numbers, the states of our atom can be described as $|\alpha JM\rangle$, where α represents all other quantum numbers. With this the energy shift is

$$W_Z = -\langle \alpha JM | B\mu_z | \alpha JM \rangle. \quad (2.57)$$

It can be shown that the right side of equation 2.57 is identical to

$$W_Z = -\mu_B B M \left(1 + \frac{\langle \alpha JM | \mathbf{J} \cdot \mathbf{S} | \alpha JM \rangle}{\hbar^2 J(J+1)} \right). \quad (2.58)$$

There is a common abbreviation [67]

$$g_{\alpha J} = 1 + \frac{\langle \alpha JM | \mathbf{J} \cdot \mathbf{S} | \alpha JM \rangle}{\hbar^2 J(J+1)}, \quad (2.59)$$

so that the Zeeman energy can be written as

$$W_Z = g_{\alpha J} \mu_B B M. \quad (2.60)$$

With $\mathbf{J} \cdot \mathbf{S} = \frac{1}{2}(J^2 + S^2 - L^2)$ we get

$$g_{\alpha J} = g_{LSJ} = 1 + \frac{J(J+1) + S(S+1) - L(L+1)}{2J(J+1)}, \quad (2.61)$$

where g_{LSJ} is called the Landé g-factor.

state	g_{LSJ}	M_J	W_z/B
3P_2	$\frac{3}{2}$	2	$3\mu_B$
		1	$\frac{3}{2}\mu_B$
		0	0
3P_1	$\frac{3}{2}$	1	$\frac{3}{2}\mu_B$
		0	0
3P_0	1	0	0

Table 2.1: Strength of the Zeeman effect W_z for the $^3P_{2,1,0}$ states according to equation 2.60.

Zeeman Effect of the Metastable Neon

Like all closed shell atoms the neon atom possesses no permanent magnetic moment in its ground state. This can change, however, if neon is excited into higher states, i.e. by lifting one of the 2p electrons into a higher orbital. An excitation into the 3s orbital leads to 4 rotational states $^1P_1, ^3P_{0,1,2}$. The transition between the excited states $^3P_{2,0}$ and the ground state requires a change in total angular momentum of either $\Delta J = 2$ or $\Delta J = 0, J = 0 \leftrightarrow 0$. These transitions are not allowed for an electric dipole transition and therefore the lifetime of these excited states are very long: 24.4s for the 3P_2 state [68] and even 430s for 3P_0 [69], therefore those excited states are called metastable.

Because the excited states of neon are not generally eigenstates J^2, L^2 and S^2 but linear combination of $|\alpha JM\rangle$, the Russell-Saunders coupling does not apply anymore and equation 2.61 is not the exact Landé g-factor. Fortunately the metastable excited states 3P_0 and 3P_2 have a unique J quantum number, so there is no mixing and those “pure” states are in fact well described by equation 2.61.

The strength of the Zeeman effect for the different states of metastable Neon are given in table 2.1.

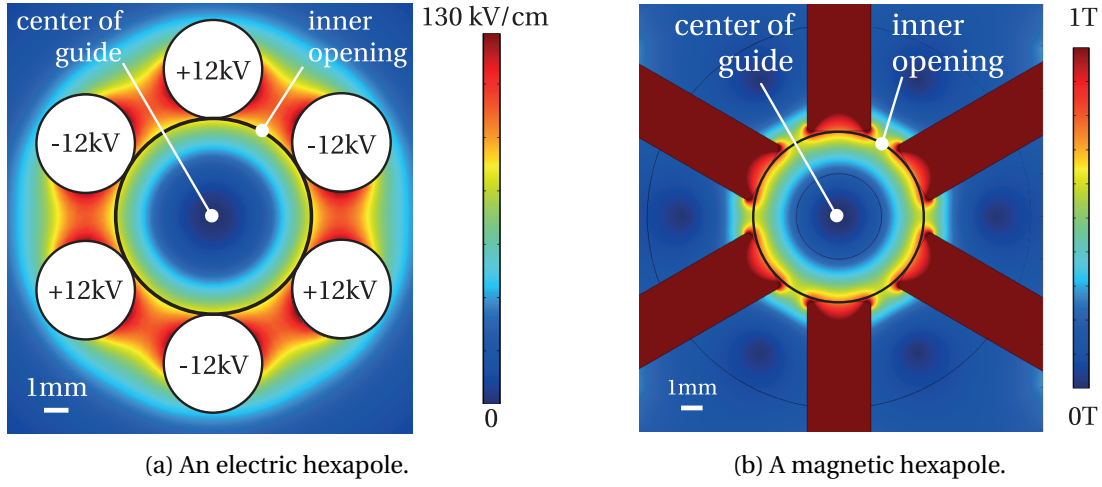


Figure 2.8: Hexapole configurations.

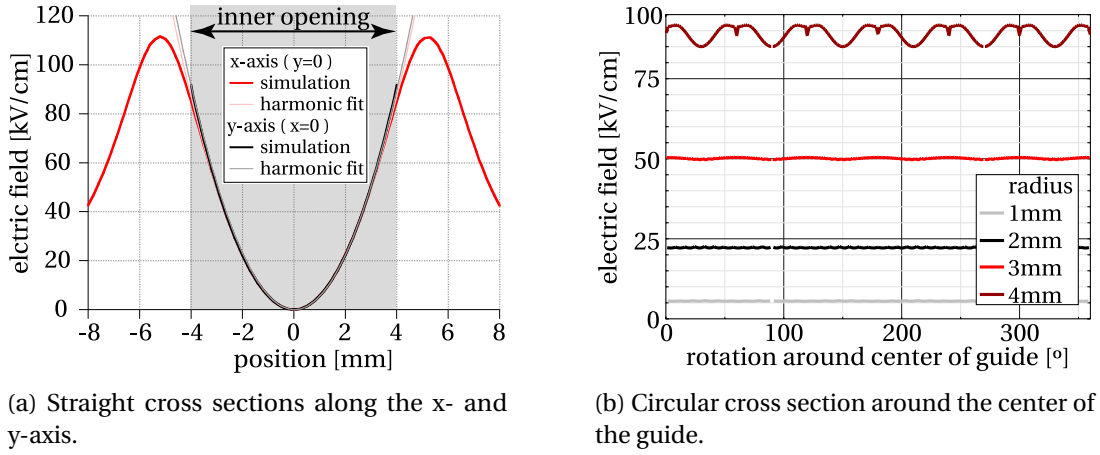


Figure 2.9: Electric fields along cross sections of the electric hexapole of figure 2.8a.

2.5 Guiding

2.5.1 The Hexapole Guide

Figure 2.8 shows cross sections through an electric and a magnetic hexapole guide. Those fields are zero in the center and will rise nearly quadratically until the edge of the inner opening, which is bounded by the electrodes or magnets.

A perfect harmonic potential is achieved if the electrodes or magnets would have a hyperbolic shape. Hyperbolic shapes are extremely difficult to machine and as the use of circular electrodes already produces a very harmonic potential it is common to use cylindrical electrodes in electric guides. The best approximation of an harmonic potential with cylindrical rods is achieved if the ratio of the electrode's radius to the radius of the inner opening is 0.565 [70]. But as shown in figure 2.9, even the use of electrodes with a ratio of $\frac{1}{2}$ produces an electric field which differs from a perfect harmonic field only in the range 10^{-3} in radial directions (see

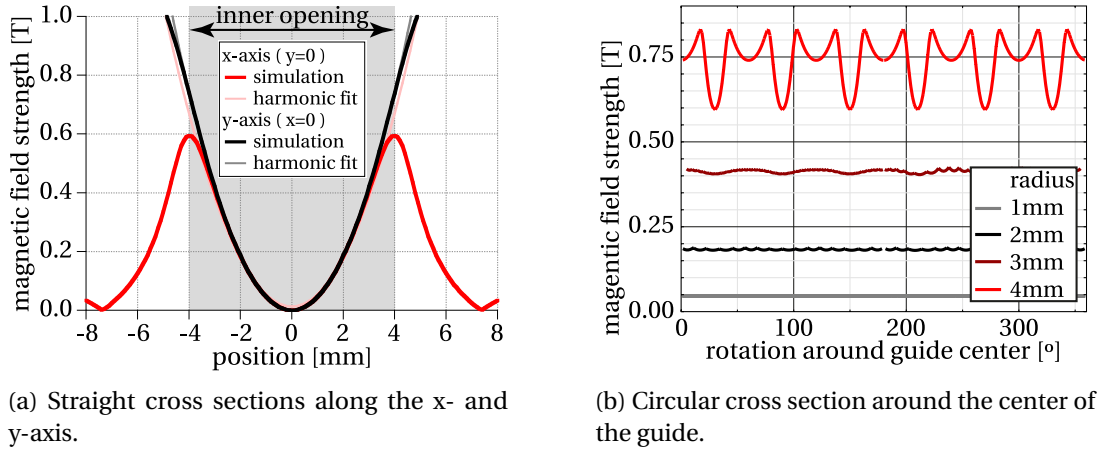


Figure 2.10: Magnetic field strength along cross sections of the magnetic hexapole of figure 2.8b.

fig. 2.9a). The variation from a perfect harmonic potential in a circular cross section is less than 6% (see fig. 2.9b).

But even for the rectangle magnets in figure 2.8b, the field strength is nearly harmonic. Figure 2.10 shows that in this case the radial divergence to a perfect harmonic potential is still only 0.4%. The variation on the edge of the inner opening is much bigger with 15%, but the variance declines rapidly toward the center of the guide, so that an harmonic potential is still a valid approximation even for rectangular magnets.

Parabolic fields directly lead to a harmonic potential if the Stark or Zeeman effect is linear. While this is the case for the Zeeman effect in metastable rare gas atoms, it is not necessarily true for polar molecules. In the exemplary case of ND_3 , as shown in figure 2.11, the Stark energy for ND_3 in an electric hexapole guide (as shown in fig. 2.8a) can be very well described by a harmonic potential. Due to its large inversion splitting and the consequently more quadratic Stark Effect of NH_3 , a hexapole guide can, in contrast, not be described by a harmonic potential for NH_3 .

The absolute strength of a quadratic Stark effect is relatively lower than of the linear one. This can also be seen in figure 2.11, where the Stark energy at the edge of the inner opening of NH_3 is $\approx 25\%$ lower than for ND_3 .

The two-dimensional potentials discussed above can be seen as two dimensional traps for particles in a low-field-seeking state. A particle with a suitable Stark or Zeeman effect is trapped in the xy-plane if its kinetic energy in this plane is lower than the corresponding Stark or Zeeman energy at the edge of the inner opening⁴.

For particles in high-field-seeking (hfs) states the same configuration is not a potential minimum but a maximum. Particles in a hfs state are therefore pushed towards the electrodes or magnets.

⁴ It is generally assumed throughout my thesis that particles are lost once they are outside the inner opening r_{max} , although for a short distance the fields between the electrodes will push the particles in a lfs state back into the guide.

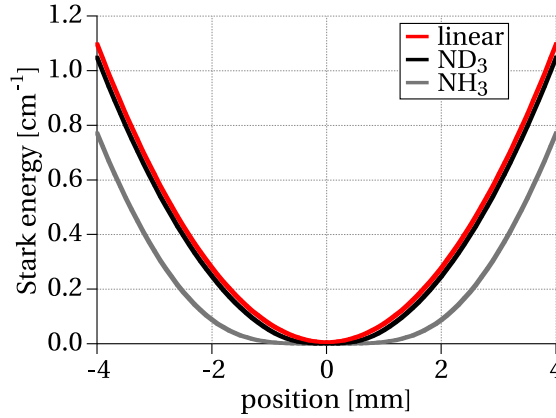


Figure 2.11: The Stark energy for different Stark effects in the fields of figure 2.8a: Purely linear Stark effect with $0.75 D$ (red), and for ammonia in the $J_K = 1_1$ state with $M_J = -1$; NH_3 (black) and ND_3 (gray).

By extending the magnets or electrodes along the z -axis (perpendicular to the plane of the figures) as shown in figure 2.12, these potentials can be used to guide particles in an lfs state. As particles in an hfs state are expelled from the potential inside the guide, such a guide will act as a filter for particles in a lfs state.

Dynamics in a Straight Hexapole Guide - Transverse Oscillations

Guidable particles will oscillate around the potential minimum with a specific frequency ω . Due to its similarity with the transverse oscillations in a synchrotron, this oscillation is called *betatron oscillation* [71].

In the case of a harmonic potential, this frequency ω is the same for any particle with the same magnitude of the guiding effect and independent of the particle's amplitude. In the case of a non-harmonic potential, the frequency also depends on the amplitude. The amplitude of the betatron oscillation can also be seen as a criterion for the guidability of a particle. If the particle enters the guide with a phase which will lead to an amplitude exceeding the inner opening of the guide, the particle cannot be guided.

Due to the (nearly) harmonic potential in a hexapole guide for guidable particles with a (nearly) linear guiding effect, one can use a hexapole guide as a lens to focus those particles. This is illustrated in figure 2.13. Molecules with a perfect linear Stark effect are focused on the exactly same point in a perfectly parabolic field if they have a common starting point. In the simulations of figure 2.13 using the fields shown in figure 2.8a, the molecules with a perfect linear Stark effect (red lines) are focused within a distance of about 7 cm. The use of cylindrical electrodes instead of hyperbolic electrodes causes a small deviations in the parabolic dependency of the electric field inside the guide, which gives rise to this blurring. The Stark effect of ND_3 is quite linear for high fields (see fig. 2.7); nevertheless, its quadratic part blurs the focus up to around 10 cm (see black lines in fig. 2.13). The quadratic part of the

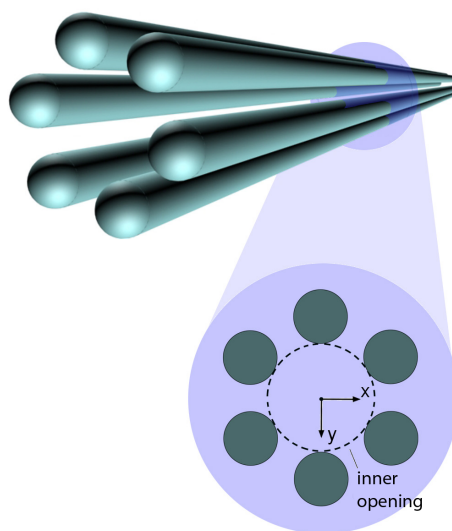


Figure 2.12: A straight guide.

Stark effect of NH_3 becomes so dominate that there is hardly any focus anymore (gray lines in fig. 2.13).

The focal length of such a lens depends on the strength of the Stark effect and the time the molecule spends inside the lens. Due to this temporal dependency the focal point depends on the longitudinal velocity of the molecule.

The focusing can be either used to increase the density of the guided particles at a certain point or, by using pinholes and beam blockers, to filter for certain rotational states, as the length of a betatron oscillation depends on the rotational state of the particle [72].

In our merged beam experiment we used such a hexapole lens to prepare the molecules for a 500 mm free flight.

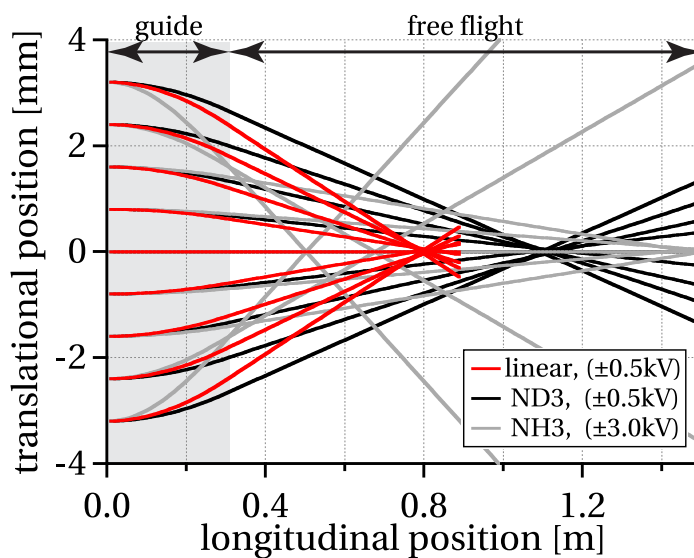


Figure 2.13: A straight hexapole guide as a lens. Simulated trajectories for a polar molecule with mass 20 and a perfect linear Stark effect (red line), ND_3 (black line) and NH_3 (gray line). All molecules have the same longitudinal velocity of 800 m/s and zero in the transversal direction. The hexapole guide has a geometry as shown in figure 2.8a and a length of 300 mm. The applied voltage is $\pm 0.5 \text{ kV}$ for the molecule with a linear Stark effect and ND_3 and $\pm 3 \text{ kV}$ for NH_3 .

2.5.2 Curved Hexapole Guide

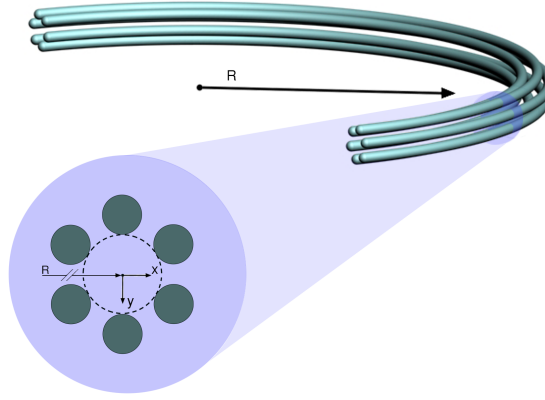


Figure 2.14: A curved hexapole guide.

In a curved guide the particles experience an additional force, the centrifugal force

$$F_c = \frac{m v_l^2}{R + x}, \quad (2.62)$$

where v_l is the longitudinal velocity (tangential to the curvature of the guide), R and x are the coordinates according to figure 2.14, and m is the mass of the particle. The influence of this force can be described by a pseudo-potential

$$W_c = -m v_l^2 \ln(R' + x') \quad (2.63)$$

where R' and x' are the values of distances R and x in units of *meters* in order to stay in the SI system. This pseudo-potential needs to be added to the potential of the guiding force in order to describe the effective potential inside a curved guide. If the radius of curvature R is much bigger than the radius of the inner opening r_{max} , the pseudo-potential of the centrifugal force can be assumed to be linear. In case of a harmonic guiding potential, the effective potential still has the same parabolic shape, it is simply shifted towards the outside bend. This is shown for different longitudinal velocities in figure 2.15.

At the position of the minimum of the effective potential, the centrifugal force F_c and the guiding force F_g cancel each other. Therefore this radius is called the *equilibrium radius* r_{eq} . Assuming a harmonic potential

$$W_g = W_{gmax} \frac{x^2}{r_{max}^2}, \quad (2.64)$$

where W_{gmax} is the energy of the Stark or Zeeman effect at the inner opening r_{max} , one can

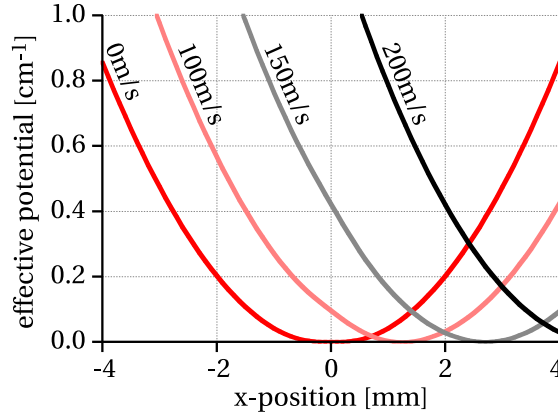


Figure 2.15: Effective potential of ND_3 in the $J_K = 1_1$ state with $M_J = -1$ in a curved $\pm 8\text{kV}$ guide with $R = 125\text{ mm}$ along the x -axis for different longitudinal velocities.

find the position of r_{eq} as the radius where

$$F_g = -\frac{d}{dx}W_g = -F_c \quad (2.65)$$

$$-\frac{2W_{gmax}}{r_{max}^2}r_{eq} = \frac{mv_l^2}{R+r_{eq}} \quad (2.66)$$

$$r_{eq} = \sqrt{\frac{R^2}{2} + \frac{m r_{max}}{2W_{gmax}}v_l} - \frac{R}{2}. \quad (2.67)$$

The equilibrium radius r_{eq} has the same dependencies as W_{gmax} . At a certain velocity v_{lmax} the equilibrium radius is right on the edge of the inner opening ($r_{eq} = r_{max}$). Particles which are faster than v_{max} cannot be guided anymore. This v_{max} is given by

$$v_{max} = \sqrt{\frac{2W_{gmax}}{m} \left(1 + \frac{R}{r_{max}}\right)}. \quad (2.68)$$

For ND_3 and the strength of the electric field we used in the experiment, we can assume the Stark effect to be linear, so that the maximum energy $W_{gmax} = W_g(r_{max})$ is

$$W_g(r_{max}) = \mu\kappa E_{max}, \quad (2.69)$$

where μ is the permanent electric dipole moment. $\kappa = \frac{M_J K}{J(J+1)}$ represents the effect of the orientation of this dipole moment to the electric field axis due to the rotational quantum numbers J , K , and M_J . $E_{max} = E(r_{max})$ is the electric field strength at the edge of the inner opening. E_{max} is proportional to the applied voltage. The maximum guidable velocity of a

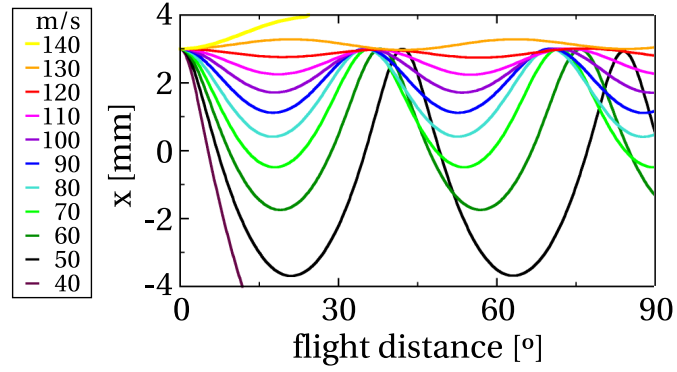


Figure 2.16: Simulated trajectories in a curved guide with radius $R = 125\text{mm}$ for a ND_3 molecule with $\kappa = \frac{M_J K}{J(J+1)} = \frac{1}{2}$ with different longitudinal velocities. The potentials and dimension of the guide are shown in graph 2.8a. The molecule enters the curved guide with zero transverse velocities at $x = 3\text{ mm}$.

symmetric top molecule with a linear Stark effect is therefore

$$v_{max} = \sqrt{\frac{2\mu E_{max}}{m} \kappa \left(1 + \frac{R}{r_0}\right)}. \quad (2.70)$$

As the particles inside a curved guide oscillate around r_{eq} , the maximum amplitude a particle can have is $r_{max} - r_{eq}$. Therefore the faster a molecule is, the less transversal velocities are accepted. This is illustrated in graph 2.16. All molecules in this simulation started from the same position ($x = 3\text{ mm}$). The different position of the equilibrium radius for each simulated velocity can be seen as the x -position around which the simulated particles oscillate.

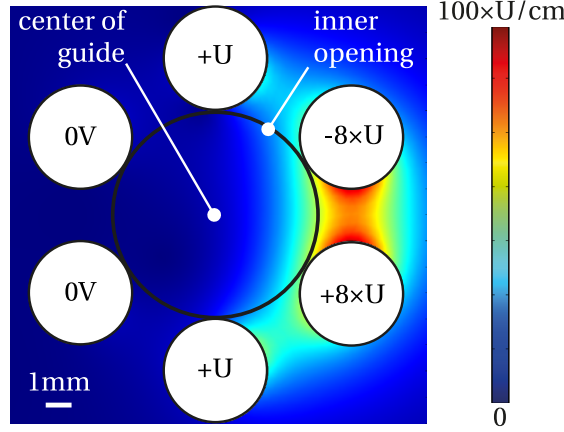


Figure 2.17: The *dipole configuration*. In a curved hexapole guide, the outside bend is on the right hand side. Please note that both central electrodes are at $+U$.

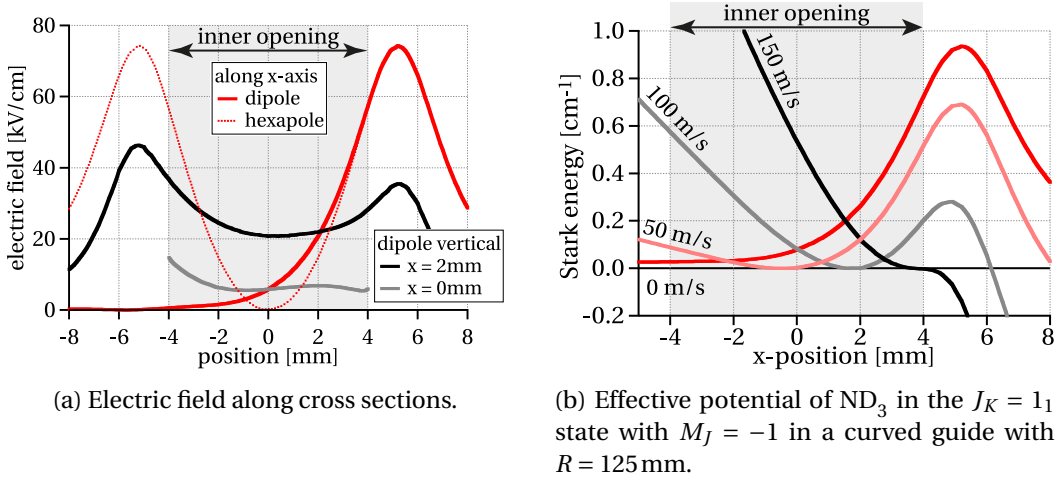


Figure 2.18: Electric fields (a) and effective potentials (b) of a 8kV dipole configuration.

The Dipole Configuration in a Curved Hexapole Guide

The *hexapole configuration*, as shown in figure 2.8a, where the polarity is alternating between neighboring electrodes is not the only applicable field in a curved hexapole guide. Figure 2.17 shows the so-called *dipole configuration*. The dipole configuration is labeled according to the magnitude of the electrode at the outside bend (positive x) of the guide. Figure 2.17 would be a 8kV-dipole configuration if $U = 1$ kV.

As shown in figure 2.18a, the field of the dipole configuration is optimized in order to achieve a continuously declining field in the negative x -direction while having the highest possible confinement along the y -axis. In order to achieve this, both center electrodes has to be applied to the same voltage. As there is no potential minimum along the x -axis inside the dipole configuration, a molecule with a zero longitudinal velocity is pushed out of the guide towards the inner bend (left hand side in fig. 2.18a). A molecule needs a certain centrifugal force in order

to stay inside the guide. This effect can be seen in the effective (pseudo-)potentials in figure 2.18b. In order to create a minimum in the effective potential, a certain pseudo-potential originating from the centrifugal force is needed. Just like in the hexapole configuration, once the centrifugal force is too strong, i.e. the molecule is too fast, the minimum of the dipole configuration is shifted out of the guide on the outside bend.

The dipole configuration can therefore be used as a band-pass filter for velocities as it has two thresholds, one for the maximum and one for the minimum guidable velocity. In figure 2.18a the comparison of the field along the x-axis between the hexapole configuration (dotted red) and the dipole configuration (solid red) shows that the field at the outside bend has the same magnitude. Therefore we can expect a comparable maximum guidable velocity v_{max} in both configurations.

The situation is very different for the confinement in the y-direction. Although the dipole configuration had been optimized in order to achieve the highest possible confinement in this dimension, it is very weak compared with the hexapole configuration. There is hardly any vertical confinement on the left hand side (inner bend, $x < 0$ mm) of the potential. This is of minor importance as the potential minimum for the majority of the velocities lies within the right side of the guide (see figure 2.18b) and the molecules therefore will spend more time within the right-hand side ($x > 0$ mm) of the guide.

Due to the reduced confinement in the y-direction, the total transmission of the dipole configuration will be much lower than in the very well confined hexapole configuration. This lack of confinement in y-direction of the dipole configuration will have the consequence that the theoretically highest guideable velocity as described in equation 2.68 will not be observed in the experiment as the acceptance of the dipole configuration will be too small for this velocity to guide a detectable amount of those molecules.

2.6 Trajectory Simulations

In order to get a better understanding of the dynamics of the molecules while traveling through the guide, we developed a very accurate trajectory simulation program. This program is written in C++ and calculates the motion of the molecules by solving the equations of motion (equation 2.45 and 2.60) using a Runge-Kutta method of the 4th order [73]. The fields inside the guide are simulated with the finite element solving software *COMSOL* [74] with a spacial resolution of $4\mu\text{m}$ on the x-axis and $40\mu\text{m}$ on the y-axis. The gradients in x- and y-directions of those fields are subsequently calculated and saved in auxiliary files. In order to calculate the force on the guided particles, those fields and gradients are read and interpolated by the trajectory program.

In order to keep the trajectory simulation program flexible, the parameters of the simulation are defined in the *initial distribution file* and the *parameter file*.

Initial Distribution File

This file contains the initial three-dimensional velocity distribution and the rotational states (for a symmetric top molecule if applicable) of the simulated particles. A program calculates this distribution and saves the values for the x-, y- and z- component of the velocity and the rotational state J_K for each simulated particle. Those values can be calculated for different conditions. The user can choose whether the velocity distribution should be

- flat between v_{min} and v_{max} ,
- a Maxwell-Boltzmann distribution with a given temperature, or
- Gaussian with a given width around an average velocity v_0 (supersonic expansion).

The angular distribution could either follow a Zugenmaier distribution [75] for a tube nozzle, or be limited to a maximum ratio of transversal over longitudinal velocity, as it is the case for the geometric cut off of a skimmer. The distribution of the rotational state J_K can be set to one particular state (fixed J and K) or be distributed according to a given temperature.

Parameter File

In the parameter file the characteristics of the guide, the timings in the experiment, the computational settings and the physical properties of the particles are defined. For the characteristics of the guide

- the type of guide (electric or magnetic),
- the number of segments,
- the type of each segment (straight or curved) and its size,

- the tilt and offset between each segment,
- the applied voltage or the strength of the magnetic field, and
- the nozzle diameter and the position of the source

are defined. For the timing of the experiment the user can choose

- how long the source is open (different exit likelihoods within this time can be simulated),
- when each segment is switched on or off, and
- the timing of the pulsed detection (if applicable).

The computational setting covered the

- number of simulated particles,
- the temporal resolution, and
- the number of threads used for the calculation.

The physical properties include the mass of the particle. For paramagnetic particles the magnetic moment is required. For symmetric top molecule, e.g. NH_3 or ND_3 , the dipole moment and the inversion splitting is needed. In case of a more complicated Stark effect, the energy shift in electric fields can also be given as explicit values for different field strengths.

Output

The trajectory program calculated the trajectory of each particle through the defined guide. If the particle completes the guide the

- start and finish time,
- initial and final x-, y- and z- component of velocities,
- initial and final position, and
- the rotational state (including M quantum number for symmetric top molecules)

of the successfully guided particle are saved in an output file. Further processing of this output file can, for example, calculate

- the arrival times (AT) of the particles at the end of the simulated guide (see fig. 3.15 as an example),

Chapter 2. Introduction

- the acceptance of the simulated guide (fig. 3.7),
- the transmission profile of the simulated guide (fig. 3.5 and fig. 4.6).

2.7 Detection Methods

2.7.1 REMPI

In order to determine the rotational state populations of the guided ammonia, we used a *resonance enhanced multiphoton ionization* (REMPI) technique [63].

REMPI uses multiple photons from a laser to ionize atoms or molecules. The ionization process can be split into two steps if the energy of one or more photons matches the energy difference from states which are present in the original sample and an excited state. In this case the molecule is first excited and subsequently ionized. This increases the ionization probability by orders of magnitude compared to a direct ionization. As illustrated in figure 2.19, we used the (2+1)-REMPI scheme, where 2 photons are used to excite the observed molecule from the ground state to the excited state and a third one to ionize the excited molecule. All three photons are from the same laser pulse and therefore have the same energy. This detection scheme is described in detail in the reference [63].

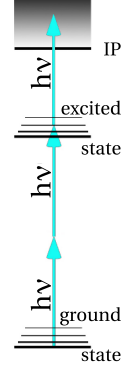


Figure 2.19:
The (2+1)
REMPI
scheme.

REMPI of Ammonia

In order to assign the measured transitions in a REMPI spectrum to the rotational quantum numbers in the \tilde{X} ground state, we need precise knowledge of the rovibrational energies of this ground state and the excited state. The ND_3 molecule is an oblate symmetric top molecule and has a symmetry of D_{3h} [76]. Including the effects of the electronic degeneracy in the \tilde{B} state, the Hamiltonian \mathbf{H}_{rve} can therefore be described as [63]

$$\begin{aligned} \mathbf{H}_{\text{rve}} = & T_v + BJ(J+1) + (C-B)K^2 - D_J J^2(J+1)^2 - D_{JK} J(J+1)K^2 - D_K K^4 \\ & - 2C\zeta lK + \frac{1}{2}q(\mathbf{L}_+^2 \mathbf{J}_-^2 + \mathbf{L}_-^2 \mathbf{J}_+^2), \end{aligned} \quad (2.71)$$

where T_v is the energy of the according vibronic state, B and C are the rotational constants, D_J , D_{JK} and D_K are the distortion parameters, and ζ is the constant for the Coriolis coupling. The constants of equation 2.71 are given for ND_3 in table 2.2. We assume the wavefunction to be a product of the rotational part $|JKM_J\rangle$ and a vibronic part $|l\rangle$. For the vibronic part $l = 0$ in the ground state and $l = \pm 1$ in the excited state. The term $q\mathbf{L}_\pm^2 \mathbf{J}_\pm^2$ connects the l levels and gives rise to the so-called *l-type doubling* [63]. The solution for the degenerate vibronic states requires the diagonalization of a 2×2 -matrix as the basis functions $|JKM_J\rangle| -1\rangle$ and $|J(K+2)M_J\rangle| +1\rangle$ are mixed due to the q term in 2.71. With this consideration, the energy

constant	\tilde{X} [65]	$\tilde{B}(\nu_2 = 5)$ [77]	unit
T_v	$\pm W_{inv}(J, K)/2$	62993	$1/\text{cm}$
B	5.1426	4.4829	$1/\text{cm}$
C	3.1246	2.6949	$1/\text{cm}$
q	-	0.1589	$1/\text{cm}$
D_J	196,6	318	$10^{-6} 1/\text{cm}$
D_K	-0.6364	789	$10^{-6} 1/\text{cm}$
D_{JK}	-347.94	-1209	$10^{-6} 1/\text{cm}$
ζ	-	0.8311	-

Table 2.2: Rotational constants of the \tilde{X} and the $\tilde{B}(\nu_2 = 5)$ state of ND_3 .

$E(J, K)$ is given by

$$E(J, K) = \frac{1}{2} \left[E'_0(J, K+2) + E_0(J, K) \pm \sqrt{\Delta E^2 + q^2 f(J, K)^2} \right], \quad (2.72)$$

where

$$\Delta E = E'_0(J, K+2) - E_0(J, K) \quad (2.73)$$

$$E_0(J, K) = T_v + BJ(J+1) + (C-B)K^2 + 2C\zeta K + \dots \quad (2.74)$$

$$E'_0(J, K+2) = T_v + BJ(J+1) + (C-B)(K+2)^2 + 2C\zeta(K+2) + \dots \quad (2.75)$$

$$f(J, K) = \sqrt{[J(J+1) - K(K+1)][J(J+1) - (K+1)(K+2)]} \quad (2.76)$$

Equations 2.75 and 2.76 have to be extended according to equation 2.71. Figure 2.20 shows the energy levels for ND_3 according to equation 2.72.

Symmetries in Two Photon Transitions

Due to symmetry reasons not all transitions are allowed in such an dipole transition. For the rotational transitions we can only initiate transitions which follows

$$\Delta J = 0, \pm 1, \pm 2 \quad (2.77)$$

$$\Delta K = \pm 1 \quad (2.78)$$

$$\Delta l = \pm 1. \quad (2.79)$$

In case of the observed transition in ND₃, the following rules apply for the vibronic transition:

$$\begin{aligned}
 \tilde{B}(v_2 = \textit{even}) &\leftarrow \tilde{X}(0) \\
 \tilde{B}(v_2 = \textit{odd}) &\leftarrow \tilde{X}(1) \\
 \tilde{B}(v_2 = \textit{odd}) &\not\leftarrow \tilde{X}(0) \\
 \tilde{B}(v_2 = \textit{even}) &\not\leftarrow \tilde{X}(1),
 \end{aligned} \tag{2.80}$$

where $\tilde{X}(0)$ is the lower state of the inversion doublet, $\tilde{X}(1)$ the higher one. The ν_2 is the *umbrella* vibration of the N-atom through the plane of the deuterium atoms. As the low-field-seeking molecules are in the $\tilde{X}(1)$ state we could only excite the guided molecules into odd ν_2 states.

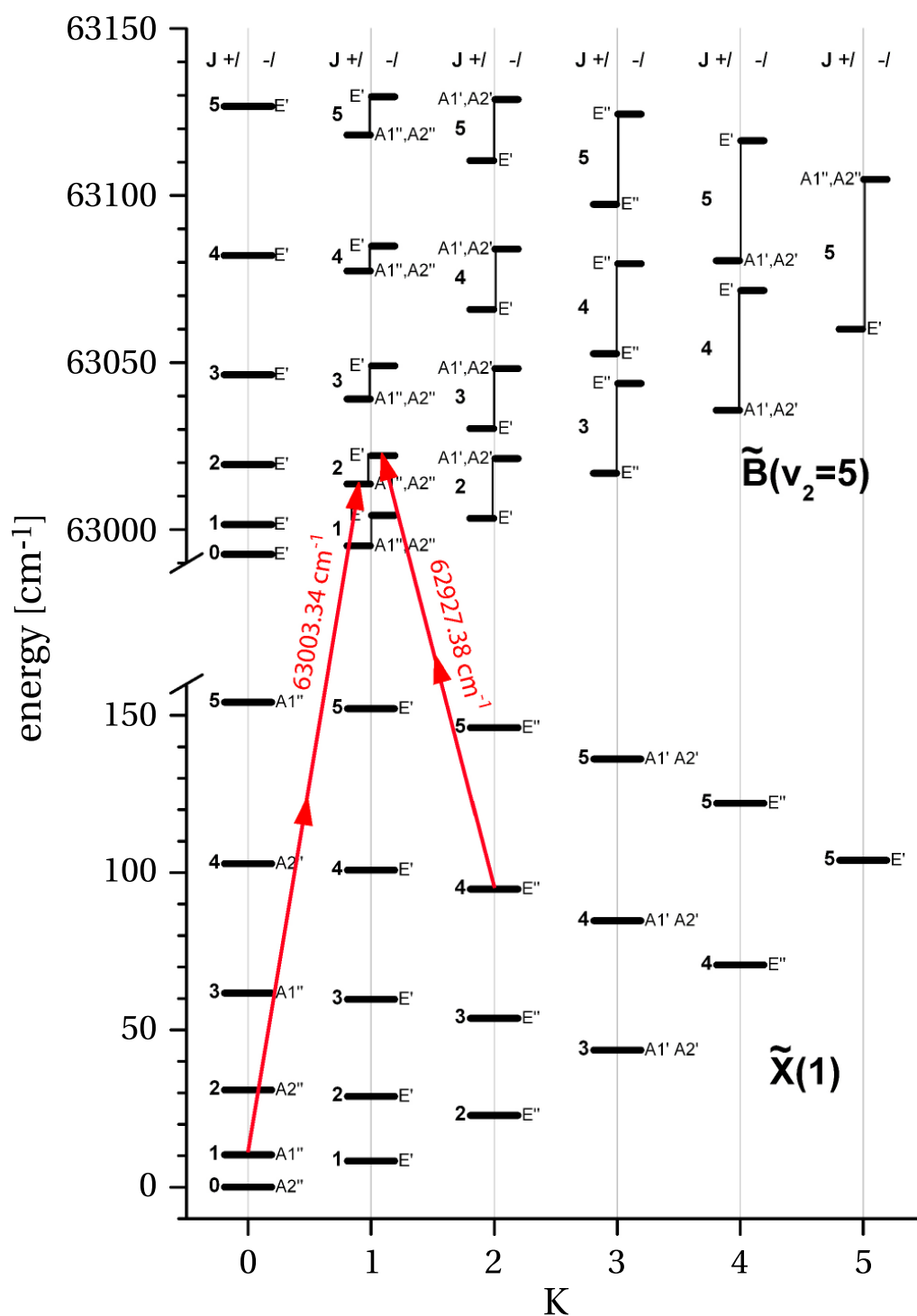


Figure 2.20: The energy levels of the $\tilde{X}(1)$ and $\tilde{B}(v_2=5)$ state of ND_3 . The rovibronic symmetries are labeled. The red arrows are examples for allowed two-photon transitions.

3 Velocity Filtering

3.1 Introduction

The idea of velocity filters is to remove certain, usually molecules with high velocities from a beam of molecules. The simplest way to do so is by rotating two wheels with apertures in such a manner that only molecules with a certain velocity have free passage [78, 79].

Another approach, which allows the preparation of a continuous beam of velocity controlled particles, is to use a curved guide. As the guiding force, which keeps the particles inside the guide, is limited, some particles are too fast to follow the curvature and are consequently lost from the guide. This concept was first realized by Ghaffari *et al.*, using the Zeeman effect of Li atoms in a curved magnetic guide [80]. The first electrostatic velocity filter exploiting the Stark effect of polar molecules was implemented in 2003 by Rempe *et al.* [81]. They successfully filtered ND₃, H₂O, D₂O, HDO, CH₂O and CH₃Cl down to a translational temperature of 1 K [81–83]. Although the density of the guided molecules were measured by a state-sensitive quadrupole mass spectrometer, Motsch [84] *et al.* determined the population of selected states of guided molecules indirectly by depletion measurements.

The curved guide technique provides a continuous source of cold molecules which is, compared to Stark or Zeeman decelerators, technically quite simple. Although the densities at the end of a decelerator are usually higher than a velocity filtered beam, the velocity filter can provide a continuous beam, so that the total flux of a velocity filter can be higher than the pulsed beam from a decelerator.

Willitsch *et al.* used a velocity filter to control the energy of CH₃F in the Ca⁺ + CH₃F reaction. As the Ca⁺ ions could be laser cooled to 400 mK, the kinetic energy of the CH₃F molecules brought most of the kinetic energy into the reaction. The electrostatic velocity filter provided them a beam of CH₃F down to 2 K yielding an average collision energy of 1.3 K [85]. The same idea was later used by different other groups to investigate the reactions Ca⁺ + CH₂F₂, Ca⁺ + CH₃Cl, Ca⁺ + CH₃CN, Ca⁺ + ND₃ and N₂H⁺ + CH₃CN [86, 87].

Just recently a new technique was introduced by Rempe *et al.* which might combine the advantages of the decelerator, i.e. the active deceleration, with velocity filtering, i.e., the continuous beam. The *centrifuge decelerator* [30] is a curved guide which forces the molecules

from a circular movement in to a spiral trajectory to the center of the rotation. The centrifugal forces decelerate the molecules continuously down on their way to the rotation, providing a continuously beam of decelerated molecules. Intensities of several 10^9 /mm²s and velocities down to 15 m/s have been achieved for CH₃F, CF₃H and CF₃CCH.

Our primary aim was to learn more about the dynamics of individual rotational states in an electrostatic guide. We were the first to use a state-selective REMPI scheme to detect the guided molecules, while all other preceding experiments used state-insensitive quadrupole mass spectrometers.

The long-term objective was the improvement of the velocity filtering technique, so that it can be used for collision experiments. Therefore we were aiming for the highest possible flux and the best possible energy resolution. In order to improve the energy resolution we tried two different techniques (switching the straight guide and the *dipole configuration*) to establish a lower threshold for the guided velocity, turning the velocity filter from a low-pass filter into a band-pass filter.

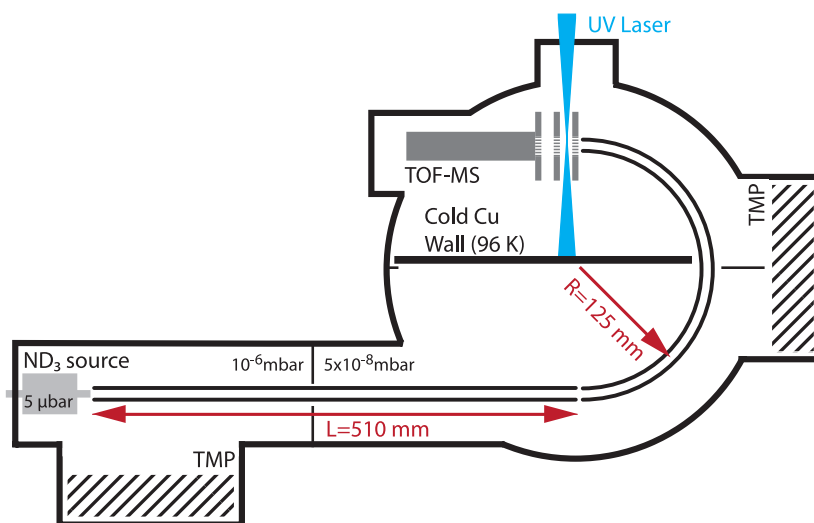


Figure 3.1: Experimental setup of the velocity filter

3.2 Experimental Setup

The velocity filter experiment had three vital parts:

- An effusive source, which provided a continuous thermal beam of ND_3 molecules.
- The guide, with a straight segment and a curved segment.
- A mass spectrometer to detect the guided molecules at the end of the guide.

The body of the effusive source was a cylindrical copper container (38 mm inner diameter, 150 mm long). The temperature of the source could have been controlled between 80 K and 500 K, but all measurements in this thesis were at room temperature.

Each guide segment was made of 6 polished stainless steel rods with a radius of 2 mm, arranged in a hexagonal pattern creating a circular inner opening with a diameter of 8 mm. With this geometry we were only able to guide molecules in the low-field-seeking state (see fig. 2.7). The source chamber was pumped by a Pfeiffer TMU1600; pumping speed 1400 L/s . The 510 mm long straight guide segment transferred the guidable molecules from the source chamber through the first differential pumping stage to the curved segment.

The curved segment guided the molecules through another (pseudo-)differential pumping stage to the detection region. The chamber of the curved segment was separated into two parts by a copper wall and both parts were pumped by the same pump (Pfeiffer TMU1400; 980 L/s). In order to increase the signal-to-noise ratio of the detection, the copper wall was cooled down to around 90 K by liquid nitrogen, which cryogenically reduces the overall ND_3 background. During operation, the pressure in the first chamber rises to $3 \times 10^{-6} \text{ mbar}$, and the pressure in the detector chamber rises from below $5 \times 10^{-9} \text{ mbar}$ to $2 \times 10^{-8} \text{ mbar}$.

For the detection of the ND_3 molecules via REMPI, the frequency-doubled output of a pulsed

Chapter 3. Velocity Filtering

tunable dye laser (Fine Adjustment Pulsare; ≈ 15 mJ/pulse at 315 nm, pumped by the second harmonic of a pulsed neodymium-doped yttrium aluminum garnet (Nd:YAG) laser (Inno-las Spitlight 1000; 20 Hz, 10 ns pulse length), was focused, using a 500 mm cylindrical lens, between the first and second plate of TOF-MS.

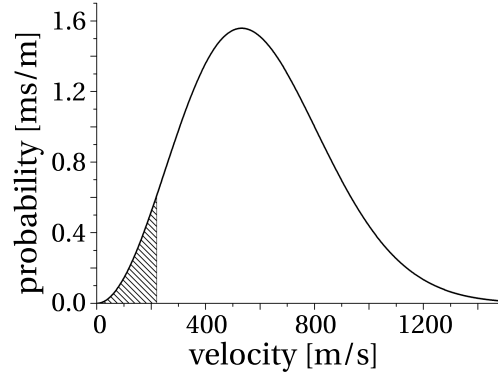


Figure 3.2: Thermal velocity distribution of ND_3 at room temperature.

3.2.1 Effusive Source

In order to achieve a high density of filtered molecules, we wanted a source which provides a very high flux of slow molecules in a very well collimated beam. We chose to use a continuous effusive source as it can produce beams which have the same velocity distribution as the thermally equilibrated molecules inside the source. An equilibrated thermal distribution can be described as

$$\rho(v) = N v^2 e^{\left(-\frac{m v^2}{2 k_B T}\right)} \quad (3.1)$$

with the normalization $N = \sqrt{\frac{2}{\pi}} \left(\frac{m}{k_B T}\right)^{2/3}$ and is shown in figure 3.2. The shaded area shows the fraction of molecules below 240 m/s . Though the relative amount of these slow molecules is small, their absolute number is huge due to the high number density of gas particles. There are still more than 10^{18} particles per cm^{-3} moving with less than 240 m/s in this distribution at 1 bar and 25°C .

As shown in figure 3.3 a simple tube used as the nozzle of the source produces a collimated beam. The bigger the ratio of length over diameter of this tube is, the better the beam will be collimated [75]. This method of beam collimation unfortunately conflicts with the demand for slow molecules, because the molecules would undergo collisions while moving through this tube. During this passage slow molecules are more likely to be hit from behind by fast molecules, which would accelerate the slow molecules and decelerate the fast ones. Therefore a tube will change the velocity distribution such that the distribution is reduced at the slow and fast ends and increased in the central part. Especially the acceleration of slow molecules, which is called *boosting*, from fast molecules was problematic for our approach, as it reduces the density of slow molecules and will even lower the overall transmission once the molecules are boosted to velocities outside the guidable range. Motsch *et al.* [88] hypothesized that this collisional acceleration of slow molecules will modify the original distribution (e.g. equation 3.1) by a factor $\exp(-b/v)$, where b is called the *boost factor*. This simple factor describes only the change for slow molecules. The influence on the faster ones is not included in this

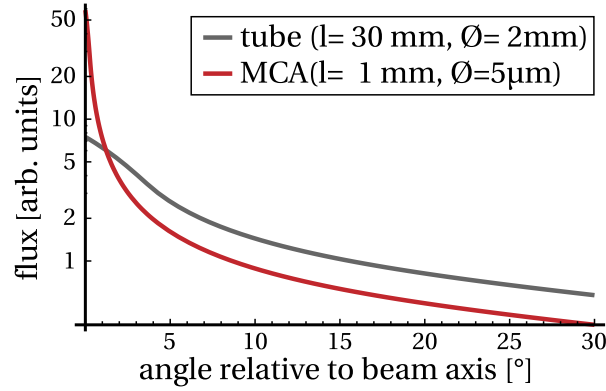


Figure 3.3: Angular distribution of the effusive source with the ceramic tube (gray line) and with the MCA (red line) as nozzle according to Zugenmaier [75].

approximation. As in our setup velocities above 240 m/s cannot be guided, this limitation has no consequences for our measurements.

The magnitude of the boosting factor depends on the collision probability inside the tube. The collision probability can be reduced by either a shorter tube or by a lower pressure in the source. However, reducing the pressure will lower the flux of the source and is therefore (normally) not desirable. Shortening of the tube length, on the other hand, demands a smaller diameter of the tube in order to maintain the collimation. But a smaller diameter will lower the flux as well.

Reducing the tube size is advantageous as several parallel tubes can be used while the total size of the source exit stays unchanged. This approach can be pushed very far by the usage of a multicapillary array (MCA). The MCA used in the measurements of section 3.3.4 was a 1 mm thick glass plate with $5 \mu\text{m}$ wide channels arranged in a hexagonal pattern with a $10 \mu\text{m}$ center-to-center distance¹. The advantage of using a MCA was the dramatically increased collimation of the beam as the length-to-diameter ratio of the MCA channels is 200, compared to 15 when using the ceramic tube. In addition, the reduced total length of the exit tube was shorter, 1 mm vs. 30 mm, which reduced the boosting factor b . Figure 3.3 shows the angular distribution for both nozzle types according to Zugenmaier² [75]. The MCA was completely covering the exit hole of the source, so that roughly 2×10^4 channels are contributing to the beam, which provided us an even higher flux at lower pressure than with the ceramic tube nozzle.

¹ This device is in fact an uncoated microchannel plate (MCP) with a zero bias angle.

² Zugenmaier calculated the angular distribution after a straight tube assuming a cosinusoidal scattering of the particles from the inside walls of the tube.

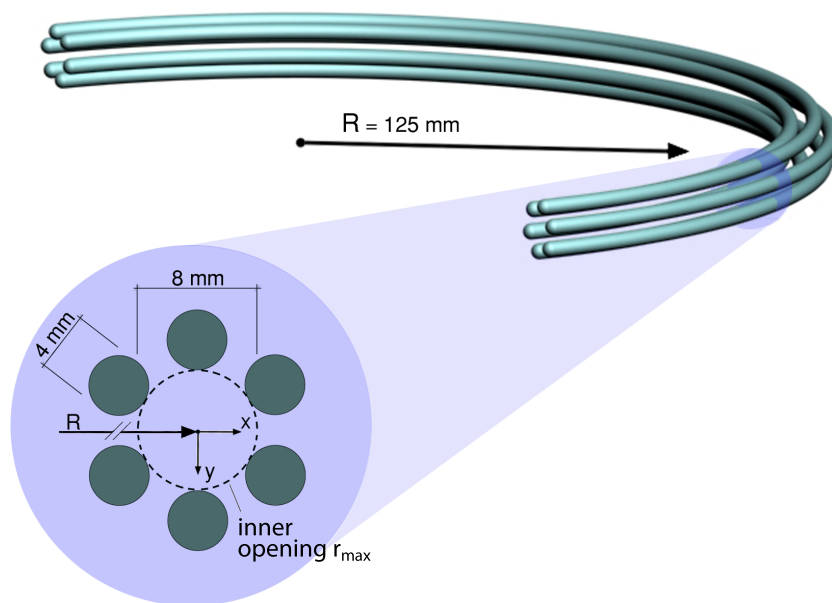


Figure 3.4: Coordinates and dimensions of the curved guide. The x -axis is always orthogonal to the curvature and points towards the outside bend. The y -axis is (atypically) pointing down, in order to have the z -axis pointing in direction of travel of the molecules (into the paper plane).

3.2.2 Guide

The guide consisted of two different segments. The main purpose of the first, straight segment was to transfer the molecules from the source nozzle through a differential pumping stage to the curved guide. The velocity filtering itself took place in the second, curved segment.

Both segments had the same electrode dimensions, shown in the inset in figure 3.4. The ratio of the diameter of the electrodes to the diameter of the inner opening was $\frac{1}{2}$. Although this produced a slightly less harmonic potential than the optimized ratio 0.565 [70], it increased the gap between the electrodes and allowed higher voltages to be applied to the guide. The applied voltages on the guide can be switched by fast high-voltage switches (Behlke: rise time ≈ 200 ns).

The straight segment was 510 mm long. For technical reasons three electrodes were permanently connected to ground, while the other three could be switched between ground and up to ± 12 kV. Increasing the voltage difference above 6 kV between the electrodes of the straight guide segment did not increase the flux at the end of the guide measurably, even if the curved guide segment was set to the maximum applicable voltage difference of 16 kV. The molecules guided additionally by the higher voltage on the straight segment could not be guided by the curved segment anymore.

The curved segment had a radius of $R = 125$ mm and covered an angle of 180° , so that the center line of the guide had a length of ≈ 393 mm. The frame of reference, as shown in the inset of figure 3.4, follows the curvature of the guide, so the x -axis is always orthogonal to the curvature and pointing to the outside bend. The centrifugal force therefore pushes the

molecules in the $+x$ -direction. The orientation of the y - and z -axis was chosen to have the molecule traveling towards $z = +\infty$.

In the curved guide segment each electrode had its own high-voltage connection; therefore, any voltage between -12 kV and $+12\text{ kV}$ could be applied on any electrode. Although the curved segment could be operated with a DC voltage of $\pm 10\text{ kV}$ without creating a leak current exceeding 100 nA , we chose to apply only $\pm 8\text{ kV}$ when we were switching the voltages on the guide. In a $\pm 8\text{ kV}$ hexapole configuration we could achieve an electric field on the edge of the inner opening of $\approx 60\text{ kV/cm}$. Using the direct access to each electrode, a $\pm 8\text{ kV}$ dipole configuration could be applied on the curved guide. This produced the fields as shown in figures 2.17 and 2.18a.

Transmission of the Guide

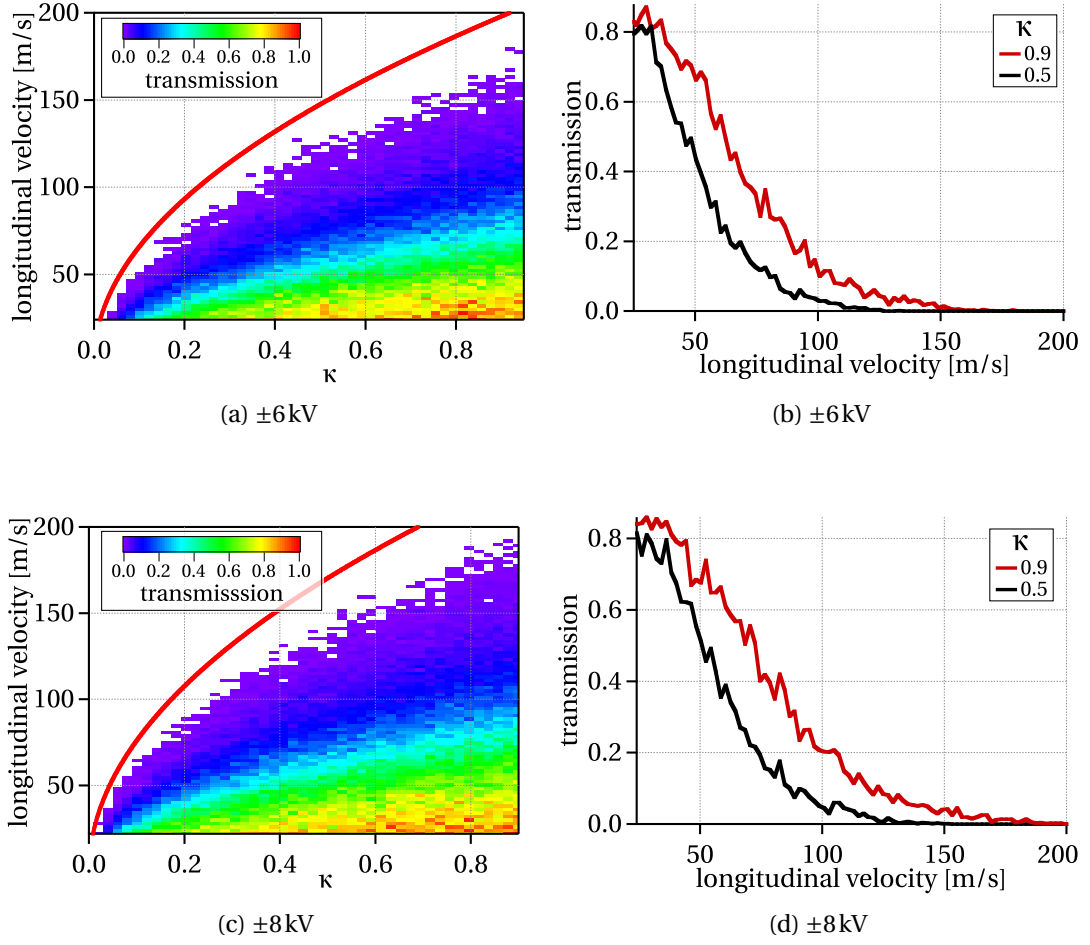


Figure 3.5: Simulated transmission of the hexapole configuration for ND_3 in a curved guide with $R = 125$ mm and a radius of the inner opening of $r_{\text{max}} = 4$ mm (see fig. 3.4). The molecules have a flat distribution for the velocities and start positions within the inner opening. The transverse velocities have a Gaussian ± 10 m/s (FWHM) distribution. The red lines in (a) and (c) show the value for the theoretical v_{max} according to equation 2.68.

Figure 3.5 shows the simulated transmission for ND_3 molecules with different longitudinal velocities and for different effective dipole moments $\kappa = \frac{M_J K}{J(J+1)}$ in the hexapole configuration; figure 3.6 shows the same for the dipole configuration. In order to highlight the influence of the longitudinal velocity on the transmission, figure 3.5, 3.6, and 3.7 show only the transmission through the curved guide for a flat longitudinal velocity distribution. The transverse velocities have a Gaussian ± 10 m/s (FWHM) distribution.

The maximum guidable velocity v_{max} according to equations 2.68 and 2.69 is indicated as the red line in figures 3.5a, 3.5c and 3.6a. The square-root dependence of v_{max} on κ can be clearly seen in the transmission simulations in figure 3.5 and 3.6, as well as the reduced v_{max} due to

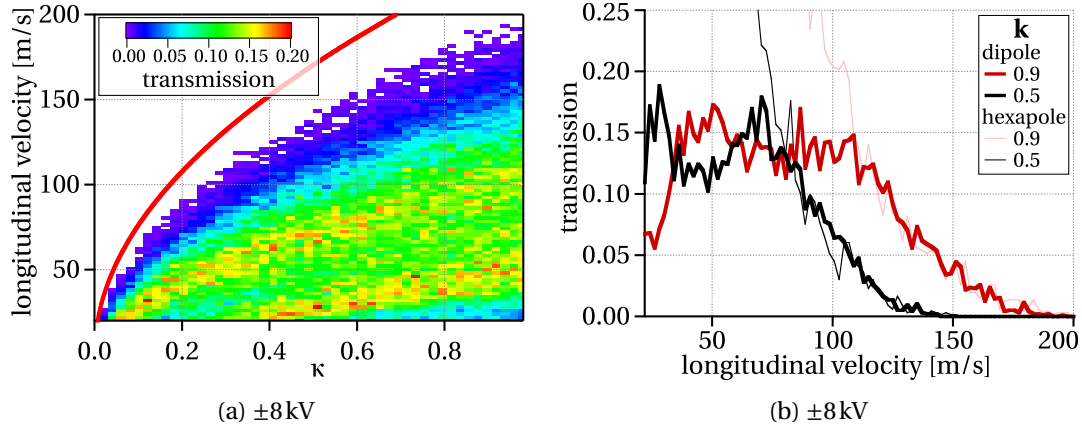


Figure 3.6: Simulated transmission of the dipole configuration for ND_3 in a curved guide with $R = 125$ mm and a radius of the inner opening of $r_{max} = 4$ mm (see fig. 3.4). The molecules have a flat distribution for the velocities and start positions within the inner opening. The transverse velocities have a Gaussian ± 10 m/s (FWHM) distribution. The red line in (a) shows the value for the theoretical v_{max} according to equation 2.68.

the lower voltage as the upper limit of the acceptance of the simulated particles shows the same dependency as the red line.

The theoretical value for v_{max} is defined as the maximum velocity of a particle can have assuming a perfect match of the initial phase space position with the acceptance of the guide this velocity can only be reached by an infinitesimal small amount of the molecules. The maximum guideable velocity which initial phase space provides contains enough molecules to be detected is therefore low which can be seen as the gap between the red line and the upper limit of the acceptance in figures 3.5a, 3.5c and 3.6a. The same argument holds for all velocities which causes the transmission probability to rise for lower velocities. Figure 3.7 shows an illustration for this argument. The higher the longitudinal velocity gets, the smaller the acceptance in the phase space will be. Close to v_{max} this phase space volume will be practically zero.

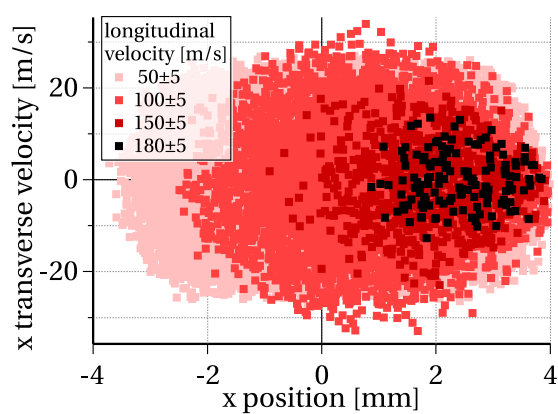


Figure 3.7: Acceptance of the hexapole configuration. In this figure the x-position and the transverse velocity in x-direction of all molecules which could completed the curved guide are shown.

3.2.3 Detection

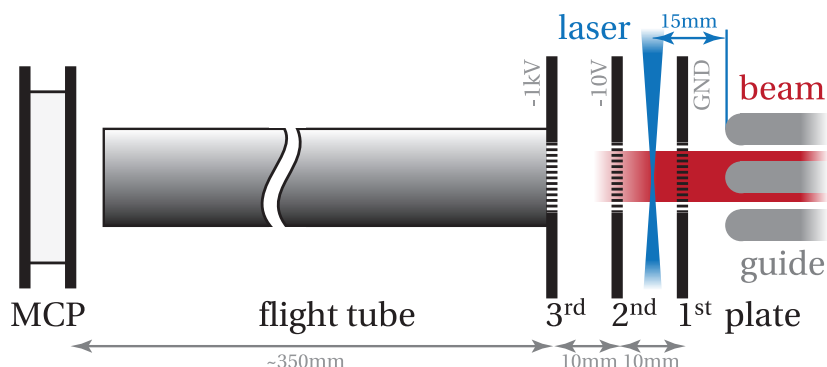


Figure 3.8: Wiley-McLaren type time-of-flight mass spectrometer (TOF-MS)

We used REMPI as described in section 2.7.1 to ionize the ammonia molecules. The ions are subsequently detected by a Wiley-McLaren type time-of-flight mass spectrometer (TOF-MS) [89] as shown in figure 3.8. The mass resolution of the TOF-MS was sufficient to discriminate between all four isotopologues of ammonia (NH_3 , NH_2D , NHD_2 and ND_3). The bandwidth of the laser was fine enough to separate single rovibronic transitions. Therefore we could measure the relative density of individual rotational states of the ground state. This was a key feature to investigate the velocity filtering for different rotational states.

The use of the rather low extraction voltage of 10V improved our signal-to-background ratio by more than 100, as the guided molecules are already moving towards the detector while the residual (background) ND_3 moves isotropic in all possible directions.

3.3 Measurements

3.3.1 Arrival Time Traces of a Hexapole Configuration

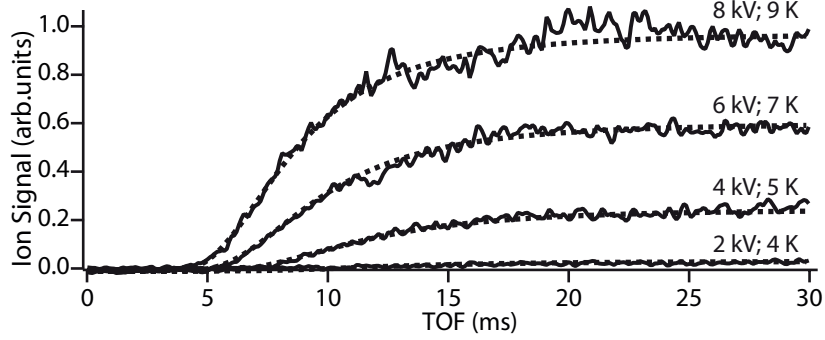


Figure 3.9: AT trace for different guide voltages. Solid curves: experimental AT traces of guided ND_3 using a $\pm 8\text{ kV}$, $\pm 6\text{ kV}$, $\pm 4\text{ kV}$, and a $\pm 2\text{ kV}$ hexapole configuration on the curved guide segment. The traces are from the same $J_K = 9_9$ state. Dashed curves: analytic calculations assuming translational temperatures of 9, 7, 5, and 4 K, respectively.

A typical measurement of the velocity filtering experiment can be seen in figure 3.9. These arrival time (AT) traces show the density of the molecules at the end of the guide as a function of the time both guide segments are switched on. This measurement was recorded by parking the Laser at the wavelength of a certain transition. In the measurement shown in figure 3.9 we choose a transition from the $J_K = 9_9$ state of the $\tilde{X}(\nu_2 = 0)$ (ground-)state into the \tilde{B} state. Therefore the recorded ion signal is proportional to the density of ND_3 molecules in the $J_K = 9_9$ state of the ground state at the laser focus. By changing the delay of the laser to the time the guide is switched on, the density can be recorded as a function of the flight time of the molecules.

After the guide is switched on, there are, for some time, no molecules present at the end of the guide, as this time is too short for even the fastest guidable molecules to travel the total distance of 918 mm. Once the fastest guidable molecules completed the guide, the density of ND_3 at the end of the guide starts to rise. This density is steadily rising because as time passes greater parts of the velocity distribution can be detected at the end of the guide. The AT trace finally approaches asymptotically a maximum value. This steady state is the density when even the slowest velocity of the initial distribution could complete the guide.

Equation 2.70 shows that the value of highest guidable longitudinal velocity depends on the maximum electric field inside the curved segment. This dependency can be seen in figure 3.9. If the voltage on the electrodes is raised, faster molecules can be guided. Faster molecules can complete the guide in less time, so the AT trace rises earlier for higher voltages. Also the steady-state density increases with rising voltages, as now bigger parts of the initial velocity distribution are present at the end of the guide. A very simple approximation for the velocity distribution of the molecules which have passed the guide is that they have a thermal distribution which can be described by a Maxwell-Boltzmann distribution [90].

Chapter 3. Velocity Filtering

This assumption was used to calculate the dashed lines in figure 3.9. AT traces with lower voltages match distributions with lower temperatures quite well. The lower the voltage on the electrodes, the colder the sample. As we do not cool but filter, the total number of molecules is also lower.

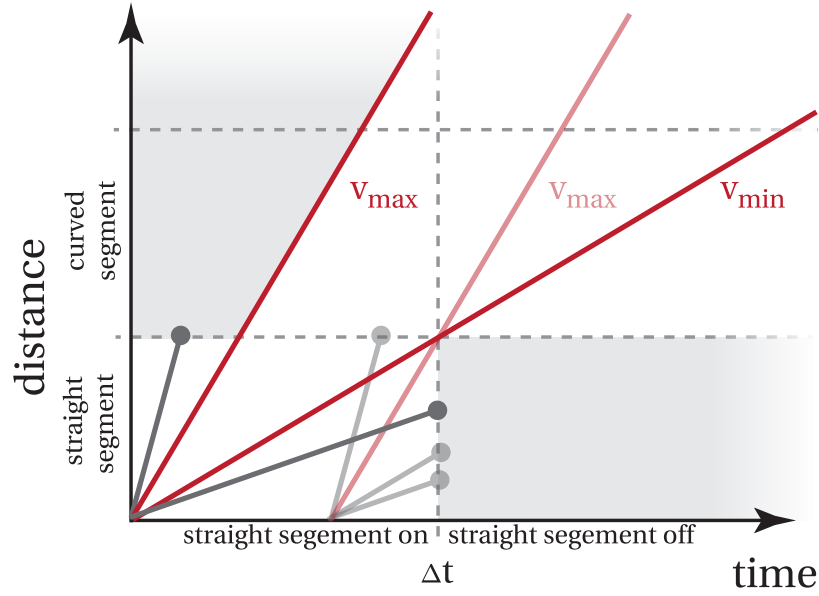


Figure 3.10: Illustration of the filtering for low velocities by switching the straight segment of the guide. The red lines indicate possible trajectories through the guide. Gray lines are trajectories of molecules which can not reach the end of the curved segment. Particles with velocities exceeding v_{max} cannot be guided due to the velocity filtering in the curved segment. A molecule is lost in the straight segment if this segment is switched off. The trajectory labeled v_{min} therefore has the flattest possible angle, i.e. the lowest guidable velocity.

3.3.2 Switching the Segments - Bandpass Filter

A static hexapole configuration, as described in the previous section, can only establish an upper threshold for the velocity, i.e., a static hexapole configuration is a lowpass filter for the velocity. The possibility to filter for low velocities as well is advantageous as with such a bandpass filter the range of guided molecules would be independent from their average velocity. This can be achieved by switching the segments of a velocity filter in a certain pattern. As there is already an upper threshold for the velocity due to the curved guide, the switching of the segments has to remove the slow molecules from the beam. As illustrated in figure 3.10, this can be achieved by switching the straight segment off after a certain time Δt . Molecules that are slower than $v_{min} = \frac{510 \text{ mm}}{\Delta t}$ will not reach the curved segment and are therefore lost from the beam. Sommer *et al.* have achieved a 5 m/s-wide band-pass filter using a similar approach [91]. In contrast to our setup they were able to switch three segments, two curved and a straight segment.

Figure 3.11 (A) shows the AT traces for the switching pattern displayed in the inset for a $\pm 8 \text{ kV}$ (black lines) and a $\pm 6 \text{ kV}$ (red lines) hexapole configuration for different on-times Δt of the straight guide. Both segments are switched on at the same time, but the straight segment is switched off after the time Δt . For the on-times shown in figure 3.11 (A), $\Delta t = 5 \text{ ms}$, 10 ms and 15 ms , v_{min} is approximately 100 m/s , 50 m/s , and 35 m/s , respectively. At first, density rises just

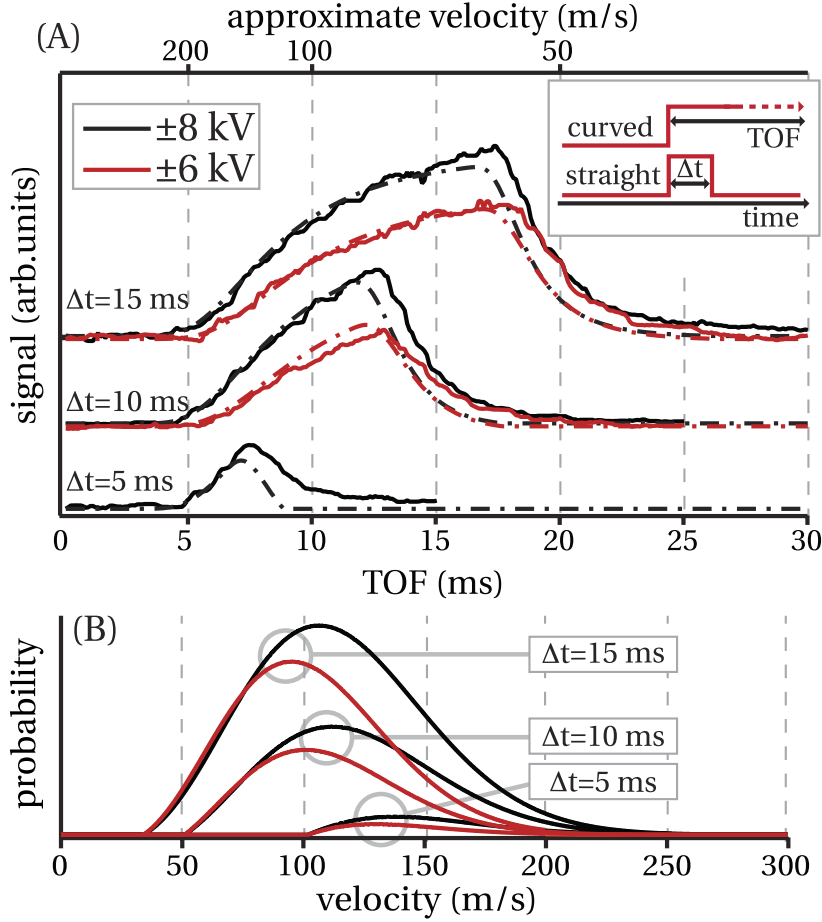


Figure 3.11: **(A)** TOF traces for bandpass-filtered ND_3 molecules using a ± 8 kV (black lines) and ± 6 kV (red lines) hexapole configuration. Solid lines are experimental data, dash-dotted lines simulations. The straight segment was kept on for a limited time Δt only such that molecules below a certain threshold velocity were not detected. **(B)** Velocity distributions corresponding to the simulated traces in (A). Black (red) show the ± 8 kV (± 6 kV) results.

as in figure 3.9, but as the flux into the curved segment is stopped when the straight segment is turned off, the guide is purged from molecules. The density at the end of the guide starts to decline once the fastest guidable molecules (v_{\max}) which just entered the curved guide at Δt have reached the end of the curved section. As in the ± 6 kV configuration v_{\max} is smaller than in the ± 8 kV configuration, the signal in figure 3.11 (A) starts to decay at later times as it takes longer for the slower molecules to purge the guide. Each switching cycle produces such a rise and decline of the signal as shown in (A).

The velocity distribution of the simulated AT traces in figure 3.11 (A) are shown in panel (B). This figure illustrates that lower velocity threshold v_{\min} is defined by the time the straight guide is switched off (Δt), while the upper threshold v_{\max} depends on the guiding voltage and is therefore different for the two displayed voltages. Due to the switching, a bandpass filter is realized where both thresholds, v_{\min} and v_{\max} , can be chosen independently.

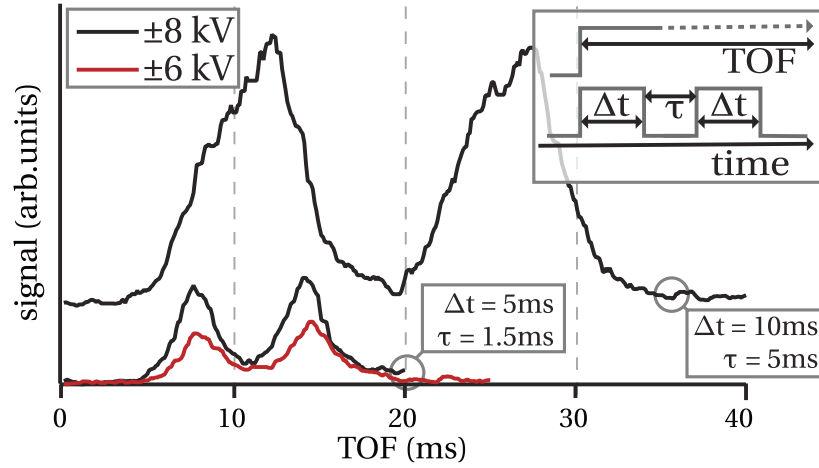


Figure 3.12: Multipulse sequence for a train of two pulses with filters at different voltages and switching sequences.

The procedure described above can be repeated continuously in order to create a quasi-continuous flux through the guide. Figure 3.12 shows that repeated switching can create a train of pulses. For a sequence with long on- and off-times, like $\Delta t = 10$ ms and $\tau = 5$ ms in the top trace in figure 3.12, the pulses are clearly separated. If the on- and off-times are short enough, e.g. $\Delta t = 5$ ms and $\tau = 1.5$ ms of the bottom traces, the pulses overlap partly and the density doesn't drop to zero between pulses. With such a setting the continuous beam of a static velocity filter can at least be partly restored.

3.3.3 The Hexapole and the Dipole Configuration

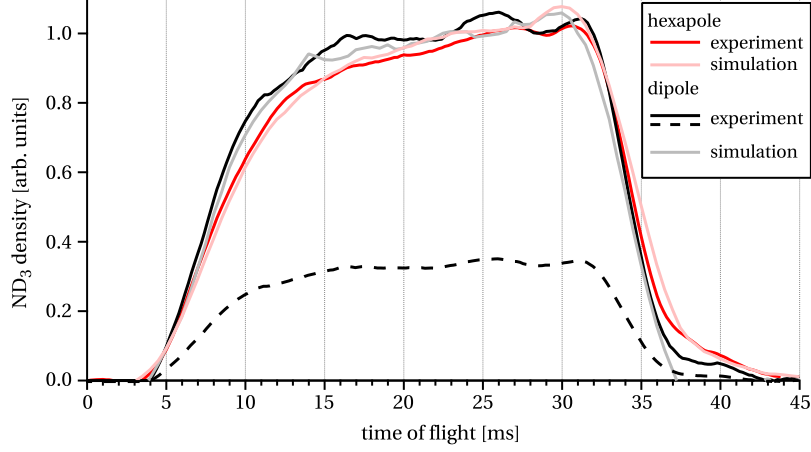


Figure 3.13: AT traces for the $\pm 8\text{kV}$ hexapole and $\pm 8\text{kV}$ dipole configuration for the 9_9 -state of ND_3 . The dashed black line was recorded under the same setting of the source conditions and detection settings as the solid red line. The solid black line was scaled to the steady state of the hexapole configuration in order to make the differences between the two configuration more visible. The guide was switched off after 30 ms.

AT traces of the dipole and hexapole configuration are shown in figure 3.13. In this measurement the laser was parked on a transition originating from a $J_K = 9_9$ state of the ground state of ND_3 . The density of this state at the end of the curved segment was recorded by changing the delay between switching on the guide and the laser. The guide was switched off after 30 ms.

This measurement was done with a $\pm 8\text{kV}$ hexapole configuration (red line in fig. 3.13) and a $\pm 8\text{kV}$ dipole configuration (dashed black line). For better comparison the graph of the dipole configuration was scaled to the steady state value of the hexapole configuration.

Here the differences and similarities between the two configuration can be clearly seen. The traces of both configurations start rising at approximately the same time, which indicates a similar v_{max} . But in contrast to the hexapole configuration, the AT trace of the dipole configuration rises much steeper and approaches the steady state value sooner. This is a consequence of the reduced probability to find slow molecules after the dipole configuration.

The differences in the transmission between the hexapole and dipole configuration can be seen by comparing the solid red curve with the dashed black one in figure 3.13. Both curves have been recorded with the same source conditions and the same detection settings. Therefore the measured density of these two curves can be compared with each other. The transmission through a dipole configuration is only about 35% of a hexapole configuration. The main reason for the reduced transmission is not the additional minimum velocity threshold but the reduced confinement in the y-direction.

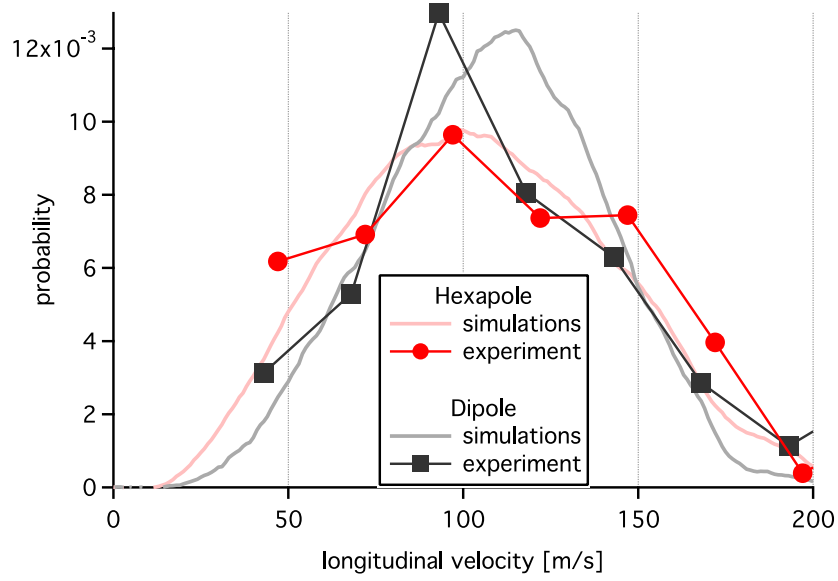


Figure 3.14: The velocity distribution for the hexapole and dipole configuration. These traces are the velocity distributions according to AT traces in figure 3.13. The distributions have been normalized to obtain the same integrated probability.

Determination the Velocity Distributions

In the previous section the measured AT have been compared with assumed distributions. But as the shape of the AT traces already contains all information about the velocity distribution, we can derive the velocity distribution from a measured AT trace.

The density $\rho(t)$ of the molecules at the end of the guide after a flight time t reflects the velocity distribution $P(v)$ of the guided molecules.

$$\rho(t) = \int_{\frac{l}{t}}^{\infty} P(v = \frac{l}{t}) dv, \quad (3.2)$$

where l is the length of the guide. If we take the derivative $\dot{\rho}(t) = \frac{d\rho(t)}{dt}$ of the recorded trace and make the substitution $v = \frac{l}{t}$ which changes $\dot{\rho}(t) \rightarrow \tilde{\rho}(v)$ we find

$$\rho(t) = \int_0^t \dot{\rho}(t) dt \quad (3.3)$$

$$= \int_v^{\infty} \tilde{\rho}(v) \frac{l}{v^2} dv \quad (3.4)$$

$$P(v) = \tilde{\rho}(v) \frac{l}{v^2}. \quad (3.5)$$

Equation 3.5 shows that the velocity distribution can be calculated from the scaled derivative of the AT trace.

A third way to reveal the velocity distribution is to perform trajectory simulations of the molecules in the guide. If all physical effects are considered properly, the simulated AT traces should reproduce the measured traces exactly. Although the direct derivation would be scientifically desirable, the measured AT traces were too noisy for continuous derivation, so we had to perform an stepwise derivation. It was very demanding to measure a trace that was smooth enough to calculate distributions with a step width less than 25 m/s .

Figure 3.14 shows velocity distributions that have been derived in the two ways described above. The experimental values were calculated from a stepwise derivation of the experimental AT traces, while the simulated distributions are obtained by the same trajectory simulations as shown in figure 3.13.

In the experimental and simulated distributions, one can see that the probability density for low velocities is reduced considerably in the dipole configuration. Due to the shallow potential minimum in the y-direction, there are also less molecules with high velocities guided in the dipole configuration. As a consequence there are relatively more molecules with a medium velocity in the dipole configuration. Compared to the hexapole configuration the dipole configuration has, as expected, a narrower velocity distribution.

Although we could detect differences between the two configurations, it turned out that the changes in the velocity distribution due to the dipole configuration are rather small. The FWHM of both configurations differs only by $\approx 20\%$ (FWHM hexapole: $\approx 105 \text{ m/s}$; FWHM dipole: $\approx 80 \text{ m/s}$) and might be achieved by other methods, e.g. by increasing the boost factor, without reducing the transmission of the guide by $\approx \frac{2}{3}$. Especially this reduced flux of the dipole configuration leads us to the conclusion that the dipole configuration is not a useful technique to increase the control of the reactant beams in a possible crossed beam experiments.

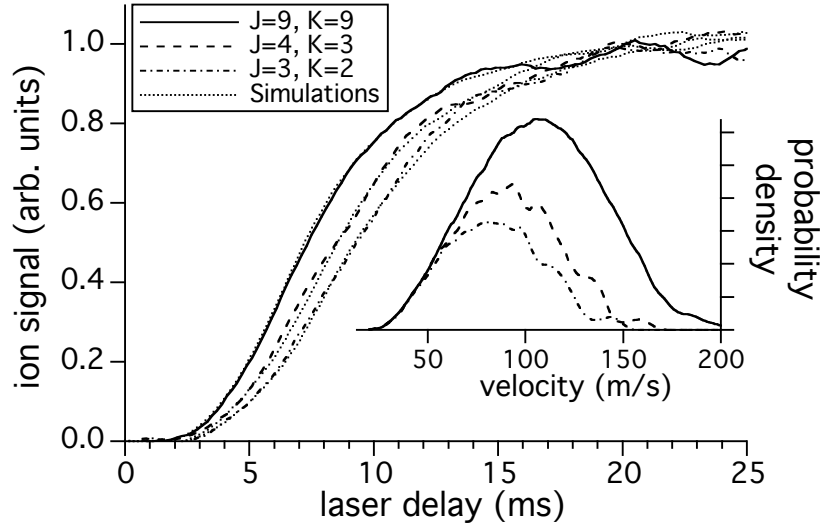


Figure 3.15: Guiding of different rotational states of ND_3 . Main panel: AT traces for individual rotational states in a $\pm 8\text{ kV}$ hexapole configuration. The solid, dashed, and dash-dotted lines show the flight times for the $J_K = 9_9$, 4_3 , and 3_2 states, respectively. Dotted lines show results from trajectory simulations for the individual levels. Inset: simulated velocity distributions for the same states as shown in the main panel. All AT traces has been normalized to the same steady-state value.

3.3.4 Filtering of Different States

In contrast to all previous experiments with velocity filters, our setup had the advantage of a state selective detection. With this feature we were able to measure the relative density of individual J_K states of the guided molecules. Equation 2.70 shows that the rotational state, represented by $\kappa = \frac{M_J K}{J(J+1)}$, together with the mass and the dipole moment of the molecule completely defines the dynamics of this molecule inside a given curved guide. The aim of the experiments described in this section is to investigate this influence of the rotational state on the guiding process.

By setting the Laser on a certain transition we could record the density of the initial J_K state of this transition. The REMPI scheme, as used in our setup, didn't offer any possibility to distinguish between different M_J values. So the traces shown in figure 3.15 contain contributions from all guidable M_J values of the recorded the J_K state. As in the measurements before the delay of the laser relative to the time the guide is switched on was tuned in order to record the AT traces shown in figure 3.15. The solid line recorded the density of the 9_9 state, the dashed line of the 4_3 state, and the dash-dotted line of the 3_2 state at the end of the guide. For better comparison all traces are scaled to the same steady state value. The dotted line are the AT traces calculated by our trajectory program. The velocity distribution obtained by this simulations are shown in the inset of figure 3.15.

The influence of the different combinations of J and K can be clearly seen in figure 3.15.

The state with the strongest Stark effect is the 9_9 -state. It has with $M_J = J = 9$ the highest $\kappa = 0.9$ of all displayed states. Also the arithmetic average $\bar{\kappa}$ of all guidable M_J values, $\kappa = 0.9, 0.8, \dots, 0.1 \rightarrow \bar{\kappa} = 0.5$, is the highest of the displayed states. Therefore the trace of the 9_9 -state has the earliest rise.

On the other hand, the highest possible κ for the 3_2 -state is $\kappa = 0.5$ for $M_J = J = 3$; the average value is with $\bar{\kappa} = 1/3$ the lowest of the displayed states. The weaker Stark effect in the 3_2 -state let only slower molecules pass the guide and we consequently observed a later rise of the trace.

The Influence of the Well-Collimated Beam from the MCA Nozzle

The measurements in figure 3.15 have been performed with the MCA as the source nozzle. The improvement in collimation compared to the ceramic tube nozzle can be seen by the significantly earlier rising time of the AT traces. In figure 3.13 the AT of the 9_9 state in the hexapole configuration with the ceramic tube nozzle starts around 3.5 ms, while the same state already starts rising before 2 ms in figure 3.15, where a MCA was used. With the MCA the beam was so well collimated that the density of molecules over the whole length of the straight guide segment was considerably high, even when the guide was switched off. This contradicts our assumption that all molecules start from the source once the guide is switched on. There is a considerable amount of molecules which start much closer to the detection area, which leads to an early rise of the AT traces. In fact the collimation was so high that we could detect molecules at the end of the guide even if only the curved guide segment was switched on. Therefore we could not perform a direct derivation of the velocity distributions with the AT traces of figure 3.15. But as the simulated AT traces reproduce the measured traces very well, we are confident that our simulation treats all vital features of the experiment, including the considerably high density of ND_3 molecules in the straight segment while the guide is switched off (pre-switching filling), correctly.

Figure 3.16 displays the different methods to obtain a velocity distribution. As the trajectory simulation has complete knowledge about the simulated particle we can obtain a very fine velocity distribution off all simulated particles which reach the end of the guide (red line). The trajectory simulation also calculates an AT trace. The stepwise derivation of that trace using equation 3.5 is another method to obtain a velocity distribution (red symbols). This method can also be applied to measured AT traces (black symbols). Figure 3.16 reveals that a simulation which contains the pre-filling of the straight guide creates AT traces, which would lead to a very wrong velocity distribution if a direct derivation would be applied (solid red vs. red symbols). But as the simulated AT traces reproduce the measured ones very well, we would in both cases get the same (distorted) velocity distribution (red symbols vs. black symbols). Therefore we will use the velocity distributions, as shown in the inset of 3.15, for the further discussion of the measurements. These velocity distributions originate from the trajectory simulations that are also shown as simulated AT traces in the main figure.

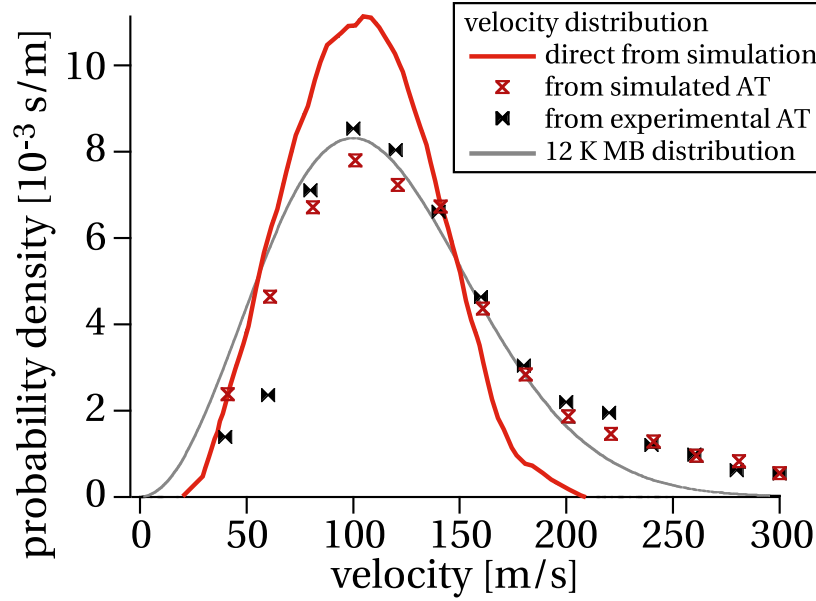


Figure 3.16: Comparison between different methods to obtain the velocity distribution. Velocity distribution obtained directly by the trajectory simulation (red line), by derivation of the simulated AT trace (red symbols) and by derivation of the measured AT trace (black symbols). The 12 K Maxwell-Boltzmann distribution is shown as a reference.

The Simulated Velocity Distribution

In the simulated velocity distribution shown in the inset of figure 3.15, the shifting of the velocity distribution to lower velocities as a function of J_K is very prominent. In contrast to the main figure where the traces have been normalized to the same steady-state value, the probability densities in the inset can be compared with each other. In analogy to a lower electric field as in figure 3.9, a weaker Stark effect leads to a colder sample with fewer molecules.

In order to get a deeper insight in the dynamics of the different M -components, we took a closer look at the velocity distributions as obtained by the trajectory simulations. Figure 3.17 shows the velocity distribution for different groups of molecules. The simple assumption that after the guiding the velocity distribution of all molecules from a thermal source can still be described by a Maxwell-Boltzmann distribution is fairly good. Comparing a Maxwell-Boltzmann distribution with 8 K (solid gray) with the simulated velocity distribution of molecules of a thermal source at 300 K (dashed) reveals only minor differences. Most prominent is the difference for fast molecules. The Maxwell-Boltzmann distribution has a slower falling edge for fast molecules than the distribution of the guided molecules. The reason for this is that in the guide there is a certain velocity threshold v_{max} which cannot be exceeded by any molecule. For the Maxwell-Boltzmann distribution, there is no such fixed threshold. Although the probabilities of finding faster molecules declines exponentially in a Maxwell-Boltzmann distribution, it has a rather long tail compared to distributions with a fixed cut-off.

Especially for collision experiments aiming for low-energies, this small difference might be considerable. The kinetic energy scales quadratically with the velocity, so an error at high

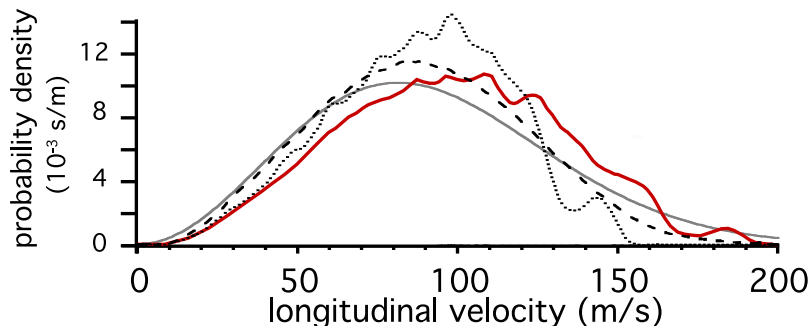


Figure 3.17: Simulated velocity distributions for ND_3 . Dashed line: All guided molecules originated from a initial rotational state distribution of 300 K. Solid red line: Only the 4_4 state with its M_J . Dotted line: A state with $\kappa = MK/J(J+1) = 0.5$. Solid line: A Maxwell-Boltzmann distribution at 8 K, for comparison.

velocities will add a much bigger error in the collision energy.

Velocity distributions of the M_J manifold of individual J_K states.

The picture gets much more detailed if we take a look at the velocity distribution of individual J_K -states. Except for the case of a very cold expansion, when only the 1_1 state is occupied, we will normally find an ensemble of different rotational states at the end of the guide. The knowledge of the exact velocity distribution of every individual rotational state becomes vital if the rotational state will influence the collision process. In this case the exact collision energy of each J_K and therefore its contribution to the cross section is important. In addition inelastic collisions, where the rotational state of the molecules is changed, can be detected much easier if the undisturbed distribution is well known.

In figure 3.17 the correct simulation of the randomly chosen 4_4 -state is shown as the solid red line. This distribution is the sum over all possible (guidable) M quantum number as shown in figure 3.18. This distribution shows significant differences to a 8 K-Maxwell-Boltzmann distribution (gray line) and to the distribution of all guided molecules as well (dashed line). This might not be very surprising as the latter two distributions assume very broad distributions in translational or rotational energy, respectively, while a specific state, like 4_4 , resembles only a very small part of those distributions.

A usefull assumption might be to simplify the M_J -manifold of a J_K state by the average κ of all guidable M -values. But the comparison between the exact distribution of the 4_4 -state (solid red) and the distribution with its $\bar{\kappa} = 0.5$ (dotted line) in figure 3.17 reveals very severe differences. An accurate treatment of the different M -values is therefore very important to obtain a good approximation for the velocity distribution for individual J_K -states.

As the trajectory simulations simulate the paths of individual molecules through the whole guide, we have to simulate many particles³ with different initial parameters in order to get a reliable results. Therefore the calculations are very time consuming. In order to avoid trajectory

³Typically 10^5 - 10^7 molecules.

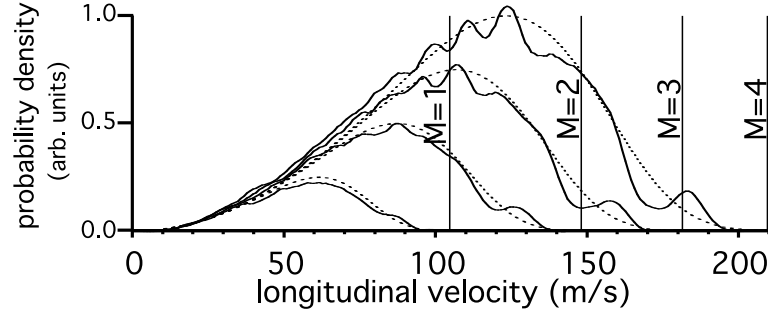


Figure 3.18: Simulated velocity distributions for the different guidable M quantum numbers of the 4_4 state (solid line) and distribution obtained by the assumption in equation 3.6 (dotted line). The vertical bars show the value of v_{max} for the different M -components according to equation 2.68.

simulations, we tried to find an analytical description of the velocity distribution of individual values of κ . This analytical distribution $P(v)dv$ should have a quadratical rise ($P(v)dv \propto v^2$ for low velocities as molecules with such velocities should be rather unaffected by the filtering process. Therefore we expect the Maxwell-Boltzmann distribution to be unchanged for the slow end of the distribution. For high velocities we have seen (fig. 3.17) that the distributions of a curved guide falls faster than the $\exp -v^2$ decay of the Maxwell-Boltzmann distribution. This can be rationalized by the fact that for higher velocities the equilibrium radius r_{eq} approaches the edge of the inner opening r_{max} (see equation 2.67). Therefore the possible amplitude of the oscillation around r_{max} gets smaller for rising velocities. As a consequence for higher velocities the acceptance range of the transversal velocities is declining and therefore the absolute number of molecules, as well. In addition this decay should depend on the analytical v_{max} (eq. 2.68). We found a decline of $\exp \left\{ - \left(\frac{v}{v_{max}} \right)^6 \right\}$ to describe this decay sufficiently well. With this reasoning we could estimate the velocity distribution for a single κ value as

$$P(v)dv = v^2 \exp \left\{ - \left(v \frac{\sqrt{2}}{v_{max}} \right)^6 \right\}, \quad (3.6)$$

where $v_{max}(\kappa)$ is the maximum guidable velocity depending on κ as defined in equation 2.70. In figure 3.18 the analytic estimations of the velocity distribution are plotted together with the exact simulations.

Transverse Motion - Stop Bands

The solid lines in figure 3.18 show an oscillating behavior (most prominent for $M = 4$ around 100 m/s), which is not reproduced by the analytic approximation of equation 3.6. This structure arises from the betatron oscillation (see section *Dynamics in a Straight Hexapole Guide* -

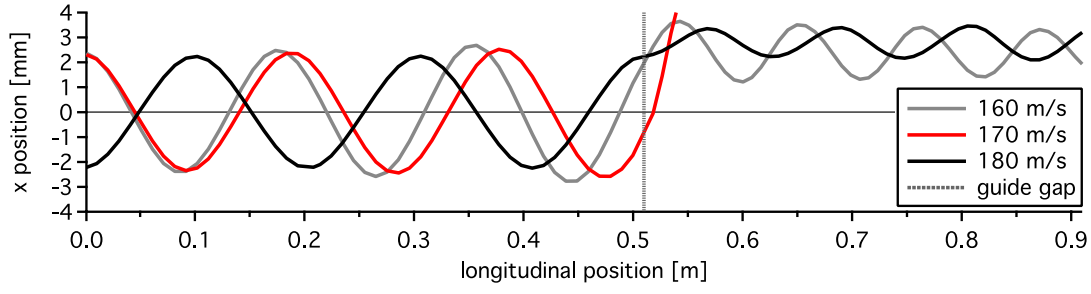


Figure 3.19: Trajectories for different longitudinal velocities. In this example a molecule with 170 m/s cannot pass the guide, although its velocity would be guidable. It is lost due to the mismatch of the phase at the end of the straight guide and the acceptance of the curved guide.

Transverse Oscillations on page 26) in the straight guide. Lets assume that the motion of the molecules can be described by

$$x(t) = x_0 \cos(\varphi(t)), \text{ with} \quad (3.7)$$

$$\varphi(t) = 2\pi\omega t \quad (3.8)$$

where ω is the frequency and x_0 the maximum amplitude of the betatron oscillation.

As the molecules are very well collimated when entering the straight guide they all start their oscillations at the point of their the maximum amplitude x_0 , i.e. $\varphi_0(t_0) = 0$ or π . For ND₃ the frequency of the betatron oscillation can be assumed to be the same for all molecules with the same κ , so that the phase at the end of the straight guide depends only on the time they spend in the straight guide. This time is given by the longitudinal velocity of the molecules. The phase at the end of the straight segment, and therefore the longitudinal velocity, determines if the molecules enter the curved guide segment concentrated in the center of the guide ($\varphi \approx (n + 1/2)\pi$ with $n \in \mathbb{N}^0$) or as widely spread as when entering the straight guide ($\varphi \approx n\pi$). Due to the curvature of the second segment, the molecules do not oscillate around the center of the curved guide but around r_{eq} (see eq. 2.67 and fig. 2.16). This is illustrated in figure 3.19 for different longitudinal velocities. A molecule can only pass the curved guide segment if the amplitude of the oscillation around r_{eq} stays within the inner opening of the guide. This amplitude is defined by the transverse velocity and position in relation to r_{eq} when entering the curved segment. This is, in turn, defined by the phase of the betatron oscillation at the end of the straight segment and the starting position. As the spacial distribution at the beginning of the guide is the same for all longitudinal velocities it is finally only the longitudinal velocity that determines how well the exiting distribution of the straight segments fits the acceptance of the curved segment.

The decline of the transmission probability between neighboring segments for certain longitudinal velocities, the so called stop bands, due to the mismatch of the phase space distribution of the particles leaving the first segment with the acceptance of the next guide segment has been investigated in detail by Zieger *et al.* [92]. The transmission will change considerably,

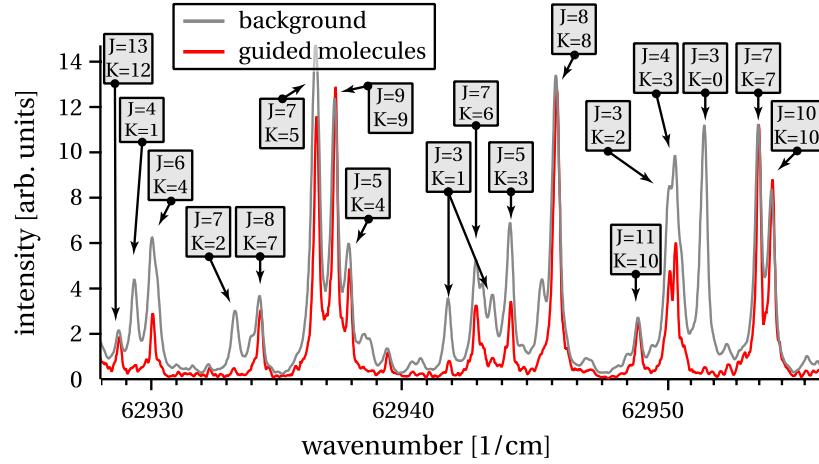


Figure 3.20: REMPI spectrum of the $\tilde{B}(v'_2 = 5) \leftarrow \tilde{X}(v''_2 = 0)$ transition of ND_3 . The insets indicate the rotational state of the $X(v''_2 = 0)$ -state. The spectra are normalized to the 8_8 -state.

even for rather small changes in the velocity, therefore giving rise to an oscillating behavior of the transmission profile. The reason why the transmission is not vanishing for those velocities is the fact that the molecules basically start from all positions inside the inner opening of the guide. So there are normally still molecules for any guidable velocity which can make it through the curved guide segment.

As these oscillations are at different positions for each M -component of a certain J_K -state they are less pronounced in our measurements where we only can measure all M -components together. But even for the 1_1 -state, which has only one M -component, the resolution of the velocity distribution derived from the measured AT traces was not good enough to observe these oscillations directly.

3.3.5 Measuring the Transmission Probability

The problem with determining the transmission probability is that the transition strength of the individual transitions are very different. If we would just compare the intensity of the ion signal of the guided molecule for different J_K -values of the ground state, we could not distinguish between good guiding or strong transition moments. In order to achieve relative transmission probabilities we did record the complete vibronic band with the guide switched on for 30 ms. In a second step, for the background spectrum, we leaked ND_3 in the guide chamber and again recorded the complete band while the guides were switched off. A part of those two spectra for the $\tilde{B}(v'_2 = 5) \leftarrow \tilde{X}(v''_2 = 0)$ transition are displayed in figure 3.20. We randomly chose one transition and normalized the two spectra according to this transition. As now this normalized transition has the same value in both spectra, we can determine the transmission probability of the J_K -states relative to the normalization transition. In figure 3.20 this is shown with the 8_8 -peak as normalization transition. The 5_3 -state has, as expected, a much lower transmission probability. The 3_0 -state is not present in the guided spectrum as

Chapter 3. Velocity Filtering

this state has no Stark effect at all. The same procedure could be done for all J_K -states, as we were able to assign a transition to nearly all observed peaks in the spectrum.

3.4 Conclusions

In our velocity filtering experiment we could successfully investigate the dynamics of different J_K -states in the guiding process. Due to the rotational-state selective detection, we achieved an unprecedented precision in determination of the velocity distribution for individual rotational states (see fig. 3.15). With our experiment we could principally measure the velocity distributions for all rotational states which are significantly present in the 300 K sample of ND₃.

As expected the translational temperature of the guided molecules is very low. A few Kelvin are easily achieved, even at relatively high flux. As the experimental data were reproduced by the trajectory simulations of our custom-made simulation program, we investigated details of the velocity distribution of the filtered molecules by analyzing the results of these simulations. This insight was used to develop an analytic assumption for the velocity distribution for any κ -value, i.e. for any combination of the J , K and M quantum numbers. This could be of interest for experiments which uses curved guides as a means to control the kinetic energy of their reactants.

We also tested the dipole configuration on the curved guide segment. The measured velocity distribution after a dipole configuration was about 20% narrower, but the transmission of the dipole configuration, on the other hand, is with $\frac{1}{3}$ of the transmission of the hexapole configuration significantly lower. From this finding we concluded that the dipole configuration is not a very useful technique to achieve narrower velocity distributions. Other methods, like an increased boost factor for example, will produce comparable velocity distributions without such a big loss in transmission.

It turned out that the very high rotational temperature of the beam together with the state-dependent translation temperature will make it very difficult to achieve a precise control over the kinetic energy of the beam. This makes the use of curved guides to further improve the presently used crossed beam experiments rather unpromising.

4 Merged Beams

4.1 Motivation

Our aim is the investigation of neutral-neutral reactions in the cold regime. With the merged beam experiment we tried to extend a method which has been successful in investigating neutral-ion reactions to neutral-neutral collisions.

A supersonic expansion provides a rather simple way to produce samples of molecules with internal temperatures down to 1 K [93]. This technique could be applied to nearly all species which can be brought into the gas phase by any means. The only problem, though, is their high kinetic energy in the laboratory frame¹. By colliding two such internally cold beams in a crossed beam experiment, the collision energy is known very precisely, but still high. The enormous progress in the development of the Zeeman and Stark decelerators was, at least partly, driven by the wish to remove the kinetic energy relative from the beams. Although it is nowadays possible to bring a beam of polar molecules to a standstill in the lab frame, the number density is reduced so much due to the deceleration that up to now collisions at temperatures below 70 K could not be successfully performed.

One idea to circumvent the problem of high velocities in the laboratory frame is to bend the two reactant beams into an overlapping parallel motion.

Already in 1929 Davis and Barnes tried to set up a merged-beam experiment for ion-electron recombination [94]. But the first successful application of the merged-beam approach for ion-ion and ion-neutral collisions was achieved in 1965 by Trujillo *et al.* [95] and shortly after (1966) by Belyaev *et al.* [96]. In the following decades this technique was used by many different groups for a great variety of ion-ion and ion-neutral collision (see [34] and references within for more details). But as the control of the motion of neutrals is much more demanding than the control of ions, merged-beam experiments, although suggested, have not been successfully implemented for neutral-neutral collisions until recently.

With the huge progress made in the manipulation and control of neutrals exploiting the Stark and Zeeman effect (see [97] and references within), it has become possible to merge beams of

¹A noticeable exception is the rotating nozzle of Gupta and Herschbach [32]. In this experiment the nozzle was move backwards with the beam velocity, so that the beam rested in the laboratory frame.

neutral particles into an overlapping, parallel motion. Just a few month before we detected the first collisions in our machine, Henson *et al.* published the first successful merged beam experiment with neutrals [29]. And already from this first paper, the power of this approach was proven, as they where able to measure reaction rates of the $\text{H}_2 + \text{He}^*$ and $\text{Ar} + \text{He}^*$ reaction down to 10mK and even observed resonances in this reactions.

Now, as this door of perception is open and as the merged-beam technique will be suitable for many other reactions, we are in the situation now where we face an as yet unknown field of science.

4.2 Former Experiments

The aim of our merged beam experiment is the investigation of a wide variety of neutral-neutral reactions in a temperature range from sub-Kelvin to nearly room temperature. Many other groups have the same aim. The following section will give an overview of some of them.

4.2.1 Crossed Beam Experiments with small Intersection Angles

As the relative velocity between particles of two beams can be reduced by lowering the angle of intersection (see equation 2.15). Toennies *et al.* applied this idea and investigated the reaction of H_2 with various rare gases down to 5 K [24]. Using cryogenically cooled Even-Lavie sources [98] and an intersection angle of 22.5° Costes *et al.* investigated the inelastic scattering of the $\text{S} + \text{H}_2$ collision down to 8 K [99]. Reducing the angle further to 12.5° they determined the inelastic cross sections for $\text{Co} + \text{H}_2$ and $\text{O}_2 + \text{H}_2$ [25, 100].

4.2.2 CRESU

In the temperatures range down to a few K the cinétique de réaction en écoulement supersonique uniforme (CRESU) apparatus is able to investigate neutral-neutral reactions for a wide range of molecules. The key element of this apparatus is the isentropic expansion of a mixture of gases through a Laval nozzle. This produces a supersonic beam, whose density and temperature is uniform for several tens of cm downstream. Each density and temperature combination demands a specially designed shape of the nozzle in order to achieve this uniform flow. The investigated reaction is initiated by creating one reactant from a predecessor already present in the beam, usually by pulsed laser photolysis (PLP) or electron bombardment. Once the reactant is created, its reactions with the surrounding gas is investigated by monitoring the temporal changes in the density of the reactants.

This approach allowed the investigation of almost 50 neutral-neutral reaction down to 13 K (see table 3 in [22]). Of special importance to our experiment is their finding that the rate constants of some radical-radical reactions are increasing for lower temperatures and can reach surprisingly high values. The reactions of CN with O_2 and C_2H_6 , for example, have a reaction rate above $10^{-10} \text{ cm}^3/\text{molecule/s}$ below 20 K; the reactions $\text{CN} + \text{NH}_3$ and $\text{CN} + \text{C}_2\text{H}_2$ even exceeds $4 \times 10^{-10} \text{ cm}^3/\text{molecule/s}$ at 25 K [101, 102]. In order to detect reactive collisions at even lower temperatures, which is our intention, such high reaction rates are desirable.

4.2.3 Merged Beam Experiment of Henson *et al.*

Just a few month before we saw our first collisions, Henson *et al.* published the results of their merged beam experiment [29]. In contrast to our setup they use only one bent guide and merge magnetically guided particles with a straight, unconfined beam.

In their first experiment they investigated the Penning ionization of H_2 and Ar by metastable

Chapter 4. Merged Beams

$\text{He}^* (^3\text{S})$ from 230 K (H_2) and 12 K (Ar) down to 10 mK. Below 10 K they detected several orbital resonances in the rate constants of both reactions.

In subsequent experiments they successfully observed an isotope effect in the Penning ionization of molecular Hydrogen (H_2 , HD and D_2) by metastable He^* in the same temperature range [103].

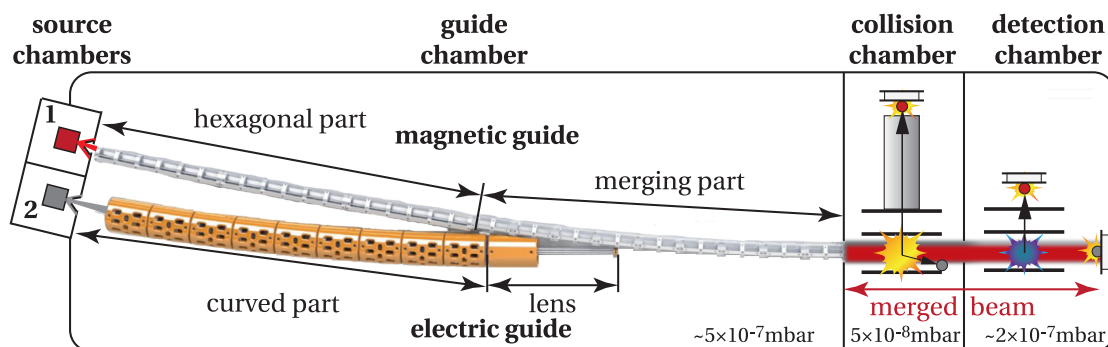


Figure 4.1: Overview of the experimental setup.

4.3 Experimental Setup

Our merged beam setup has, as shown in figure 4.1, the following vital parts:

- Two supersonic expansion sources, which provide cold and dense beams.
- One magnetic and one electric guide to merge the two beams in an overlapping, parallel motion (see figure 4.2).
- A detector to measure the reaction products, i.e. the Penning ions in our first experiments.
- Two detectors to monitor the beam intensity of the reactant beams.

The two sources produce very dense beams of translationally and rotationally cold particles, which directly enter the guides. The guides separate the particles which cannot be guided from the beam (carrier gas and reactant particles with internal states of insufficient guiding force) and bend the remaining beams into an overlapping, parallel motion. At the end of the magnetic guide, right at the entrance to the collision chamber, the beams are merged and continue to travel freely in a parallel and overlapped motion. In the collision chamber the collision products are detected by a pulsed time-of-flight mass spectrometer (TOF-MS). After the beams passed the collision chamber, they enter the detection chamber where the density of the two beams are independently monitored in real time. As the calculation of cross sections depends on the reactant's density, this information is very important for the accurate determination of the cross sections.

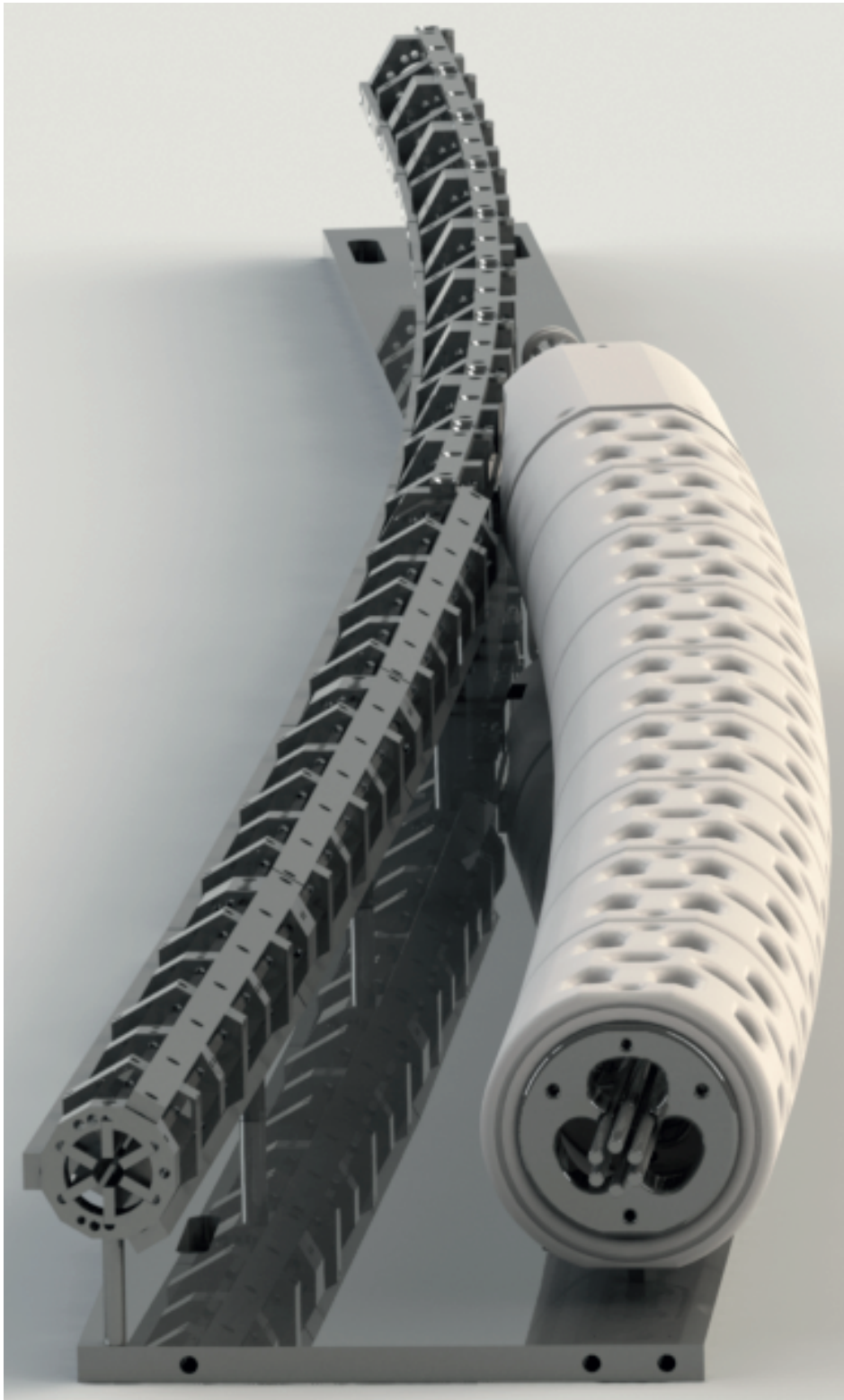


Figure 4.2: Rendering of the magnetic (left) and electric (right) guide, seen from the source side.

4.3.1 The Sources

What is required of the sources is that they provide dense beams of cold molecules. Supersonic free jet expansion sources meet this requirement [93]. In order to increase the energy resolution of our experiment, a very short opening time is desirable. In order to change the velocities of the beams, the temperature of both sources can be set to temperatures between 150 K and 400 K.

The determination of the properties of the sources has been made in a test chamber to

Source	Type	Gas	S	delay [μ s]	pulse length [μ s]	pulse center velocity [m/s]
1	Even-Lavie	Ar	20	50	34	587 ± 7
		Ne	20		34	805 ± 8
		ND ₃	6		39	1130 ± 40
2	General valve (series 9)	Ne	13	250	60 ± 15	830 ± 20
		ND ₃	3.6		87	1090 ± 50

Table 4.1: Measured properties of the supersonic valves. The delay is the time between triggering the source and the actual opening of the nozzle. The pulse length is the extrapolated pulse length just after the nozzle. The pulse center velocity was measured at room temperature.

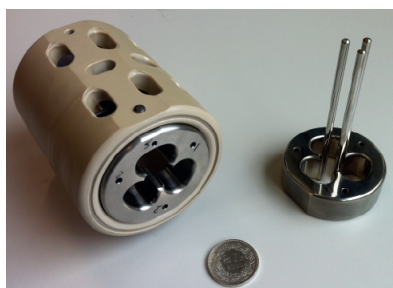
measure the beam propagation in free flight. The results are given in table 4.1. For the source of the magnetic guide (source 1 in fig. 4.1) we used an Even-Lavie source [98]. The valve is operated with a backing pressure of 10 bar to 30 bar. 1 cm after the nozzle the rare gas atoms are excited via electron bombardment.

The source for the polar molecules is a Parker general valve (series 9). Possible condensation and clustering of the molecules demand a rather low backing pressure of ≈ 1 bar. In order to achieve a sufficient flux the opening of the nozzle is with 1 mm rather big. As reducing the velocity of polar molecules by cooling the source would increase the losses from clustering and condensation, the molecules were seeded in Ne or Ar to change the beam velocity. As the rare gas atoms has much better seed ratios than the molecules seeding also improves the quality of the beam. Although having the same atomic mass, seeding ND₃ in Ne showed to reduce the beam velocity of ND₃.

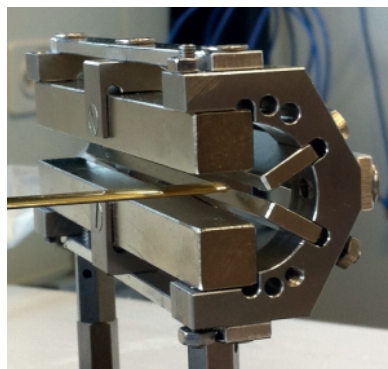
The spectroscopic characterization of the ND₃ beam after the electric guide shows $\approx 50\%$ of the ND₃ molecules in $J_K = 1_1$ and $\approx 30\%$ in $J_K = 2_2$ state. The atomic carrier gas and the ND₃ in rotational states with $K = 0$ or $J = 0$ have no effective dipole moments and do not reach the collision chamber.

Before the beams enter the guide chamber, they pass through a skimmer which removes all particles which would not hit the inner opening of the guides.

4.3.2 The Guides



(a) One segment of the electric guide. The electrode holder from the backside is removed and presented on the right.



(b) One element of the merging part of the magnetic guide. The golden stick coming from the left is the hall probe to measure the magnetic field inside the guide.

Figure 4.3: Photos of the guide segments.

In order to guide undecelerated beams of a wide variety of paramagnetic particles and polar molecules, both the strength of the guiding fields and the radius of curvature of the guides have to be as big as possible. Both guides have a curvature with a radius of $\approx 6\text{ m}$ and cover an angle of $\approx 10^\circ$. This angle is just enough to avoid a straight line of sight between the source and the end of the guide in order to separate the guidable particles from the unguidable particles. In our experiments both beams are bent, so we can reach a very high purity of the reactant particles in both beams. In the case of the electric guide, we are able to adjust the voltage applied to the guide, and therefore the maximum field inside the guide, to a value where only a single rotational state of the few occupied states in the cold beam of the supersonic source expansion can be guided. Experiments with one reactant in a single state are therefore possible.

The use of different effects in each beam makes the merging technically easier. In our experiment the magnetically guided beam is confined until both beams are merged, while the electrically guided molecules are focused into the still guided magnetic beam. This would not be possible if we used the same effect in both beams.

The second and more fundamental reason was to avoid problems due to Liouville's theorem [104, 105]. As it isn't possible to increase the phase space density by a reversible process, the merging of two beams guided with the same effect would not have produced a merged beam with the combined density of both beams but a merged beam whose density would be reduced to the value of the initial beams.

Please note, that in this experiment, unlike in the velocity filter experiment, the outside bend of the guides is in the negative x-direction. The frame of reference follows, as before in the velocity filter experiment, the curvature of the guides, so that the y-axis is always the other transverse direction, while the z-axis is the longitudinal direction.

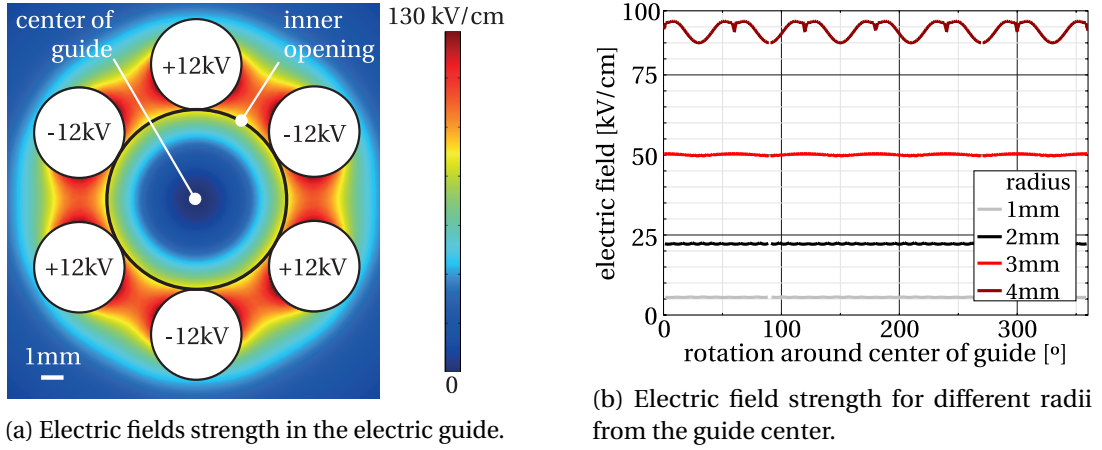


Figure 4.4: Simulated electric fields in the electric guide for ± 12 kV.

Electric Guide

The electric guide has a hexagonal geometry and consists of two parts. The first part, closer to the source, is curved in order to bend the molecules into a parallel, overlapping motion with respect to the beam from the magnetic guide. This part is made of 9 straight segments. A picture of one, partly disassembled, segment is shown in figure 4.3a. Each segment is 100 mm long and is tilted by 1° relative to the previous segment in the horizontal (xz-) plane. The first segment, where the molecules enter the guide, is aligned with the source and has extended electrodes towards the source in order to reduce the distance between guide and source. Within each segment, every second electrode is mounted on the same metal holder (as shown on the right side of fig. 4.3a).

A voltage of ± 12 kV, applied to the electrodes, creates an electric field strength of around 90 kV/cm at the edge of the inner opening, as shown in figure 4.4a. In figure 4.4b the distortions due to the use of cylindrical electrodes are shown. Right at the inner opening ($r = 4 \text{ mm}$) the variation in field strength is about 8%.

In order to avoid damaging the electric guide by discharges and high leak currents, ± 12 kV was the maximum voltage we used in the measurements of this thesis.

The second part of the electric guide is an electrostatic hexapole lens which focuses the polar molecules into the beam of the magnetic guide. This part is a single 300 mm long, straight segment and it is aligned with the final beam axis of the magnetic guide. After this segment the molecules will travel freely for 500 mm until the end of the magnetic guide. During this free flight they enter the magnetic guide.

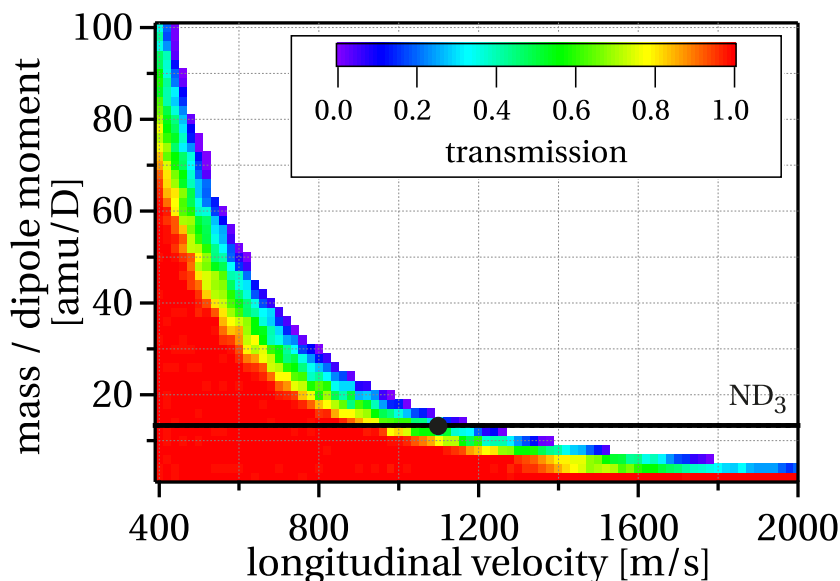


Figure 4.5: Simulated transmission through the curved segment of the electric guide (± 12 kV) for different ratios of mass over dipole moment for molecules with a linear Stark effect. The horizontal line indicates this ratio for ND_3 , the circle on this line is the velocity of ND_3 at room temperature.

Transmission

With the design of our electric guide we can only guide molecules in low-field-seeking states (see figure 2.7). Figure 4.5 shows the transmission of the curved guide segment with a guiding voltage of ± 12 kV for different ratio of mass over dipole moment assuming a linear Stark effect. For H_2O , CO^+ , CH_3F and H_2CO the transmission has been simulated using the actual Stark effect as displayed in figure 2.5. The results of this trajectory simulations are shown in figure 4.6. The ability to guide NH_3 , ND_3 , CH_3F , CHF_3 , and SO_2 has been proven experimentally.

In our first experiment we investigated the Penning ionization of ND_3 ; therefore, a closer look has been taken at the transmission of ND_3 through the electric guide and into the merged beam. Figure 4.7a shows the simulated transmission for ND_3 through the curved part of the guide (black and gray) and through the whole electric guide into the merged beam (red and pink).

First we take a look at the transmission through the curved part in figure 4.7a. If the guiding voltage is ± 8 kV (gray line) all molecules up to 600 m/s are guided through this part. Between 600 m/s and 900 m/s it depends on the particles initial transverse velocities and start positions whether they can complete the curved guide. Above 900 m/s no ND_3 molecule can be guided anymore with ± 8 kV. Increasing the guiding voltages to ± 12 kV (black line) shifts these velocities to higher values. According to equation 2.70 we would expect the velocities to increase by $1.22 = \sqrt{12/8}$ by increasing the voltage from ± 8 kV to ± 12 kV. Therefore we expect the 100% transmission velocity to move up from 600 m/s to 735 m/s , which fits very well to the simulated transmission. As for the molecules displayed in figure 2.5 the Stark effect cannot be assumed to be linear and equation 2.70 doesn't apply anymore. The ratio of the transmission velocities

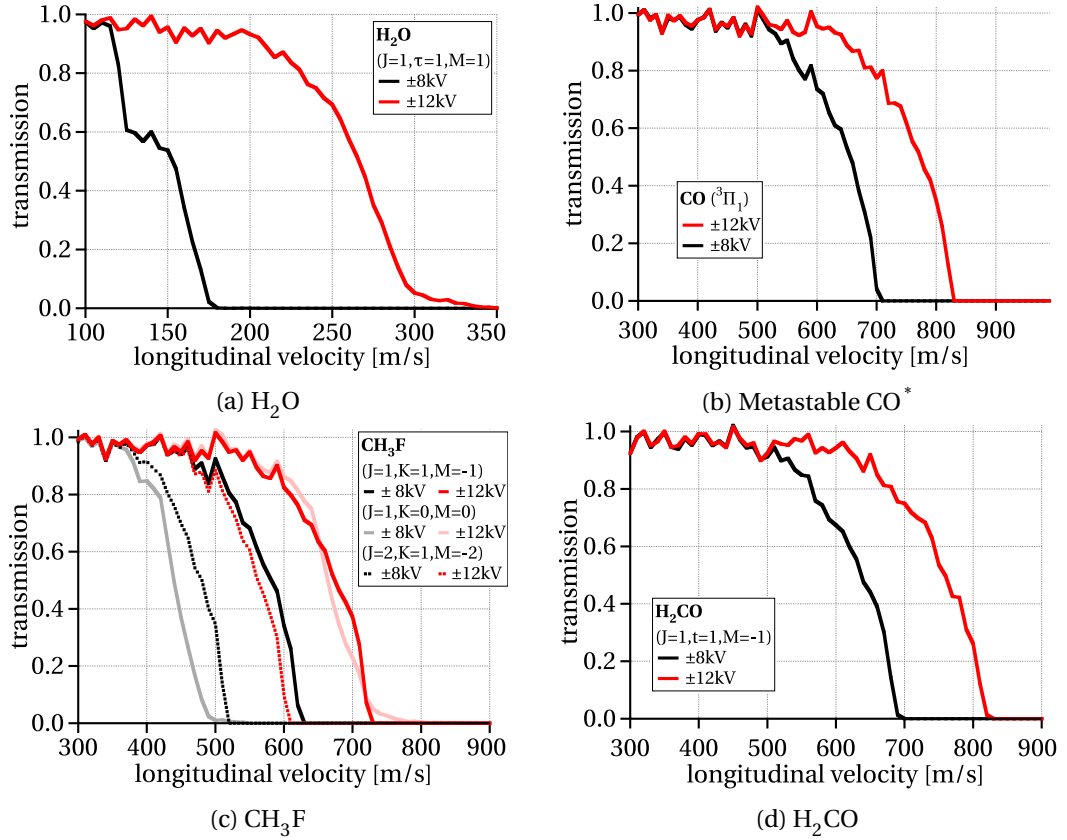


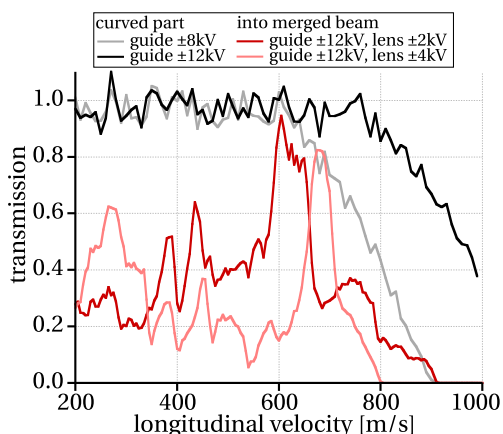
Figure 4.6: Simulated transmission of H_2O , CO^* , CH_3F and H_2CO through the curved part of the electric guide with different guiding voltages.

for $\pm 12\text{kV}$ and $\pm 8\text{kV}$ differ therefore from the value $\sqrt{12/8}$. Most remarkably this can be seen in the transmission profile of CH_3F (fig. 4.6c), where different states of the same molecule show very different ratios.

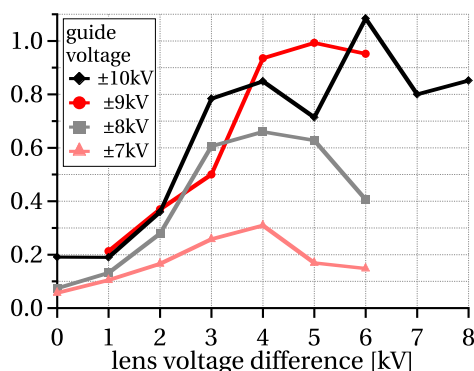
The total transmission of the particles into the merged beam is more complicated for two reasons: The free flight and the entry into the magnetic guide. As it is the purpose of the lens to focus the molecules into the magnetic beam, the focal length of this lens is crucial for the transmission. This strength depends not only on the voltage applied to the lens segment but also on the time a molecule spends inside the lens [72]. Therefore slow molecules tend to be over-focused, while fast molecules will not be focused enough. A changed beam velocity demands therefore for a different lens voltage.

In figure 4.7a this can be seen in the red and pink transmission curves. Here the transmissions until the end of the magnetic guide, i.e. to the point where the two beams are completely merged, are calculated. A higher lens voltage shifts velocities with an optimal focus to higher values.

In figure 4.7b the experimental results are shown. In this measurement the density of the ammonia molecules in the detection chamber was recorded by REMPI. As expected there is an optimum for the lens voltage.



(a) Simulated transmission through the curved part of the electric guide (black and gray) and into the merged beam (red and pink).



(b) Measured transmission of the electric guide (curved part and lens) for different lens and guide voltages. The guided molecules all had the same velocity distribution of $710 \pm 10 \text{ m/s}$.

Figure 4.7: Transmission of ND_3 in the $J_K = 1_1$ state through the electric guide.

In addition to the focal strength of the lens, the position of the focal point also depends on the phase of the molecules when they enter the lens. This effect can be seen in the different position of the optimal focus voltage for different guide voltages in this figure. A higher voltage on the curved part of the guide increases the frequency of the betatron oscillation. Therefore the phase with which the molecules enter the lens and consequently the positions of the focus is changed. This has to be compensated by a slightly different lens voltage. Figure 4.8 shows the beam profile for ND_3 in the merged beam inside the detection region of the TOF-MS.

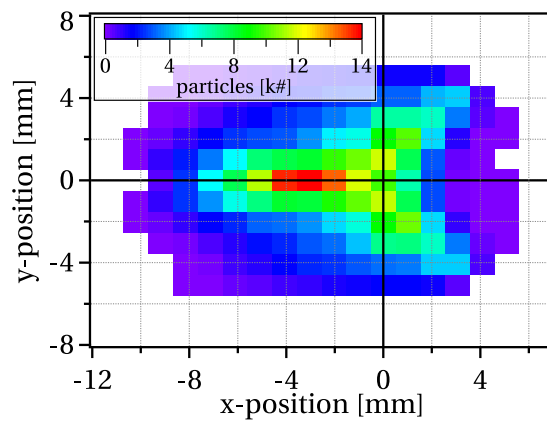


Figure 4.8: Beam profile of ND_3 with 770 m/s inside the detection region. The voltage on the guide was $\pm 12 \text{ kV}$, the focus voltage $\pm 1 \text{ kV}$. All particles inside the detection region have been summed up along the z -axis.

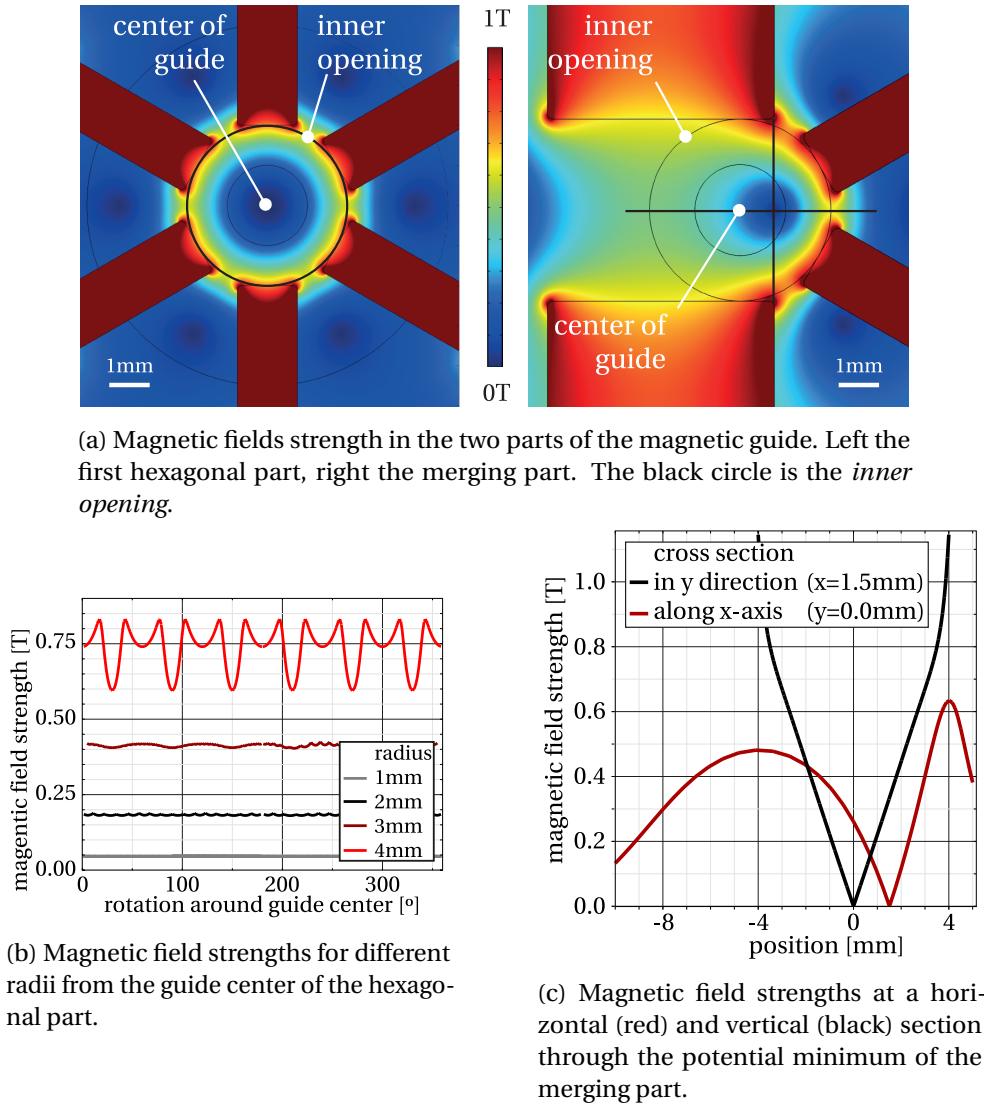


Figure 4.9: Simulated magnetic fields strength in the magnetic guide.

Magnetic Guide

The magnetic field inside the magnetic guide is created by strong permanent NdFeB magnets (grade N35, nickel coated) with a remnant magnetization of $B_r = 1.17$ T. The resulting magnetic field strength can be seen in figure 4.9.

The guide itself consists of two parts. The first part, closer to the source, has a symmetric hexapole configuration (see left-hand side of figure 4.9a). The purpose of this part is to compensate for the different length of the two guides. The magnetic field strength at different circular cross sections around the guides center in the first part are shown in figure 4.9b. The rectangular permanent magnets resemble a hyperbolic shape much worse than the circle shape of the electrodes of the electric guide. Therefore the variance of the magnetic field strength on the edge of the inner opening is, for the hexagonal part of the magnetic guide,

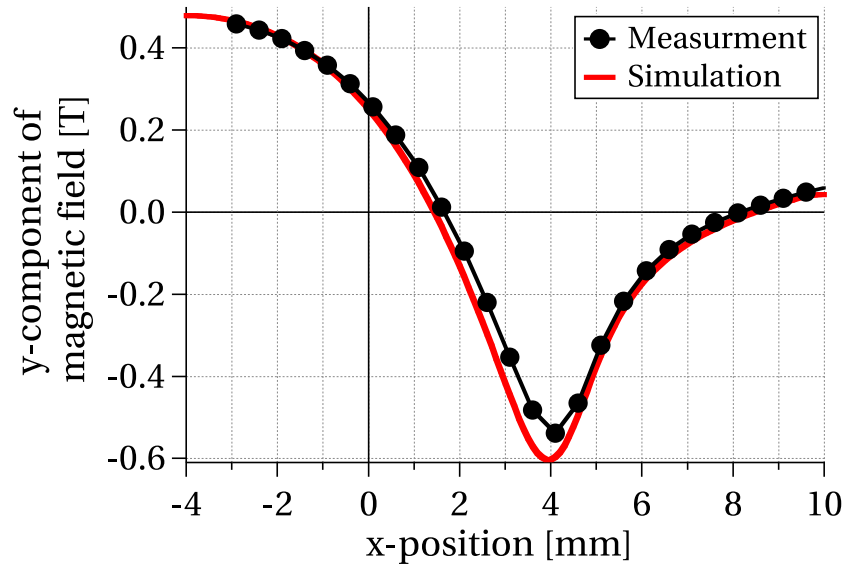


Figure 4.10: Measured magnetic field strength in the magnetic guide in comparison with the simulated strength by COMSOL [74].

with 30 % much stronger than for the electric guide. (See figure 4.4b for comparison.) The first part is made by three 300 mm long straight segments. Each segment is tilted by 1° in the horizontal (xz-) plane with respect to the previous one.

The second part of the magnetic guide has a very different geometry (see right side of figure 4.9a or figure 4.3b). In this part the two beams are merged, so the two magnets at the outside bend (left-hand side in the figures) are removed. In order to keep the particles inside the guide, the top and bottom magnets are replaced by wider magnets. Figure 4.9c shows that the field at the open outside bend is only 15 % weaker than at the closed inside bend. The beam from the electric guide can enter through this 8 mm wide gap, while the magnetic field in the gap is still strong enough to keep the paramagnetic particles inside the magnetic guide. This second, merging, part of the guide consists of 10 identical segments. Each is 100 mm long and tilted by 1° in the horizontal (xz-) plane with respect to the previous one. The merging part of the magnetic guide and the curved electric guide therefore have the same curvature.

The accuracy of the simulated magnetic fields had been tested with a hall probe. Figure 4.10 shows that the simulations were fairly accurate.

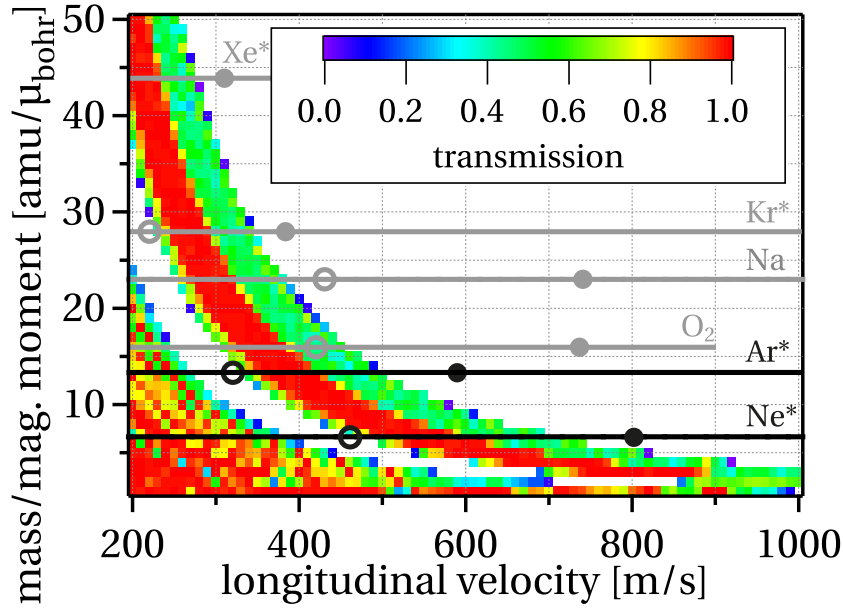


Figure 4.11: Simulated transmission of the magnetic guide for different ratios of mass over magnetic moment. The horizontal lines indicate the ratio for the labeled particles. The full (open) circles on the lines illustrates the expected beam velocity for a source at 300 K (100 K) according to [93]. The metastable atoms are in the 3P_2 -state, the O_2 is in the $X^3\Sigma_g^-$ state and Na is in the ground state.

Transmission

Figure 4.11 displays the simulated transmissions for different mass-to-magnetic moment ratios. This figure illustrates which particles could be guided. We have successfully guided metastable Ar^* and Ne^* .

There is a remarkable gap in the transmission as shown in figure 4.11, is a stop band, as described in the velocity filter experiment in section 3.3.4 on page 65. In figure 4.12, which shows the transmission for Ne^* in the 3P_2 -state in more detail, this gap is between $\approx 380 \text{ m/s}$ and $\approx 460 \text{ m/s}$. The reasons for this gap are the betatron oscillations inside the hexagonal part of the magnetic guide and the resulting mismatch of phase space distribution of the exiting molecules with the acceptance of the merging part of the magnetic guide. As shown in figure 4.13a Ne^* atoms enter the merging part of the magnetic guide at different x-positions for different longitudinal velocities. The potential minimum of the merging part is, unlike inside a curved hexapole guide, for all guidable velocities at the same position ($x = 1.5 \text{ mm}$ in fig. 4.13b). With a longitudinal velocity of 400 m/s Ne^* enters the merging part on the left-hand side around $x = -1.1 \text{ mm}$ ($\pm 1 \text{ mm}$) (red line in figure 4.13a). As the potential minimum of the merging part is located at $x = 1.5 \text{ mm}$, this molecules will have very large amplitudes around the equilibrium radius and will be lost much easier.

Molecules with 500 m/s will enter the merging part of the magnetic guide very close to the potential minimum. They will therefore oscillate much less around the equilibrium radius and are therefore very well guided.

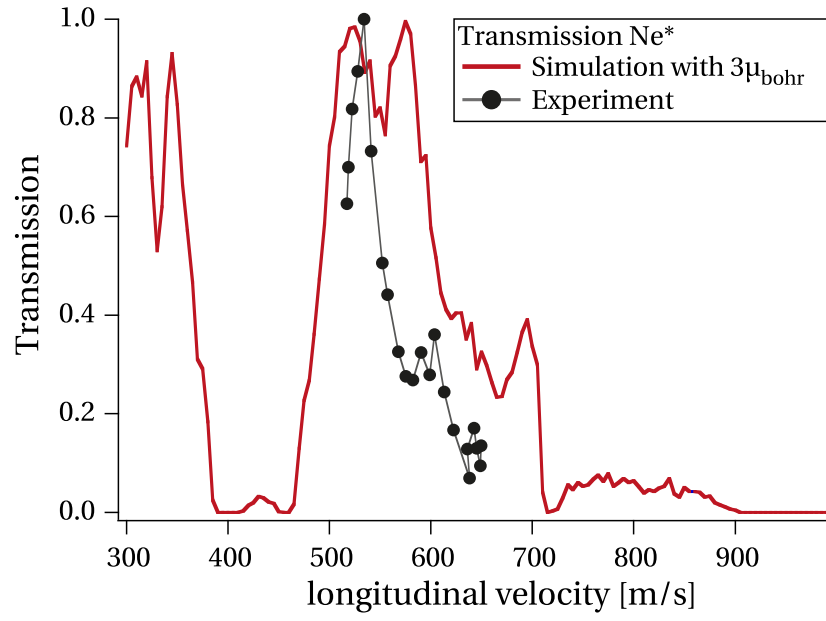
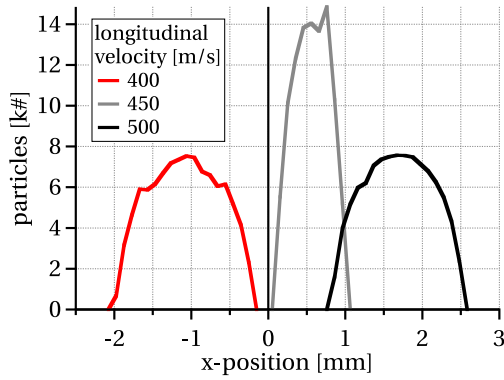


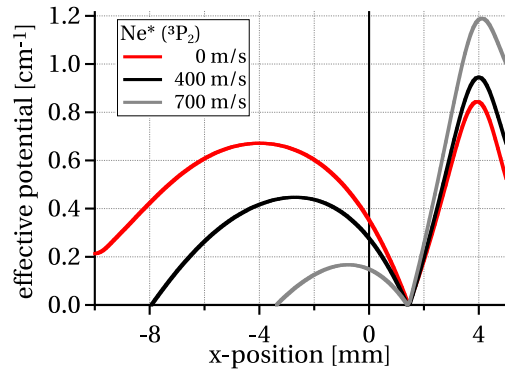
Figure 4.12: Transmission of the magnetic guide. The highest experimental transmission was set to 1.

A future improvement would be adding the possibility to adjust the horizontal displacement between the two parts of the magnetic guide inside the vacuum in order to avoid such stop bands.

The simulated beam profile of guided Ne^* are displayed in figure 4.14. The three dimensional distribution of the Ne^* in the detection region according to the trajectory simulation is shown in figure 4.14a, the integration of those particles along the longitudinal direction can be seen in figure 4.14.

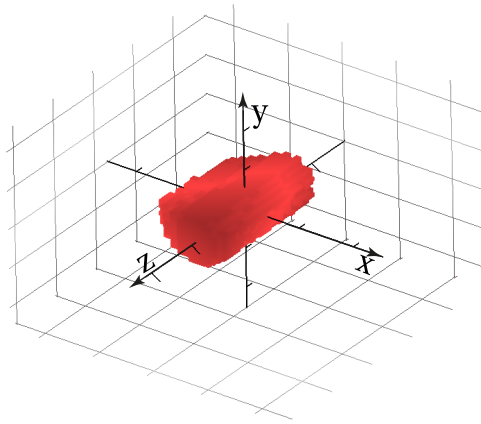


(a) Simulated x-positions of Ne^* at the end of the hexagonal part of the magnetic guide.

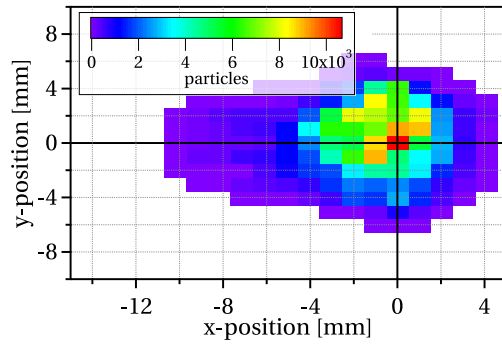


(b) Effective guiding potential for Ne^* in the merging part of the magnetic guide for different longitudinal velocities.

Figure 4.13: Illustrative simulation for the observed stop band in the magnetic guide around 450 m/s .



(a) 3-dimensional position of detected particles.



(b) Beam Profile in the xy -plane. All particles of figure 4.14a have been summed up along the z -axis.

Figure 4.14: Beam profile of Ne^* in the detection region.

paramagnetic particles	polar molecules						
	NH ₃	ND ₃	CH ₃ F	CHF ₃	CO	CH ₂ O	H ₂ O
Ne [*]	[42, 106]	[106]	[107]		[108–110]		[45, 55, 56]
Ar [*]	[111]		[112]	[112]	[113]	[111]	[111]
Kr [*]	[111]				[113]	[111]	[111]
Xe [*]	[111]		[112]	[112]	[113]	[111]	[111]
O ₂					[114]	[114]	

Table 4.2: Possible reactions that can be investigated with the current setup. Red: PI-Reactions already observed with current apparatus. Gray: Penning ionization is possible.

Possible Reactions

Besides the already successfully measured reactions (NH₃ + Ne^{*}, ND₃ + Ne^{*} and CH₃F + Ne^{*}), the current setup allows the investigation of many other reactions.

An overview of all reactions we can investigate without major changes to the apparatus (especially without any changes at the source) is displayed in table 4.2. The references within table 4.2 list experiments with the corresponding reaction, usually at room temperature or higher.

Especially interesting will be the investigation of radical-radical reaction, as they can have an increasing rate constant for lower collision energies and are key reactions to understand the chemistry in interstellar clouds [22, 115]. As most of those radicals can not be bought in bottles but has to be produced in the beam expansion, the use of different sources would be necessary. The ability to produce beams of CH and guide them in the magnetic guide would be very interesting, as the rate constant of the reaction CH + NH₃ has been measured by the CRESU apparatus down to 23 K, the reaction CH + CO down to 53 K [22]. The production of CN for the electric guide would allow us to investigate the rate constant for the CN + O₂ reaction. This reaction been measured down to 15 K and showed arising rate constants for lower temperatures [101]. With our apparatus we could extend those measurements to even lower temperatures.

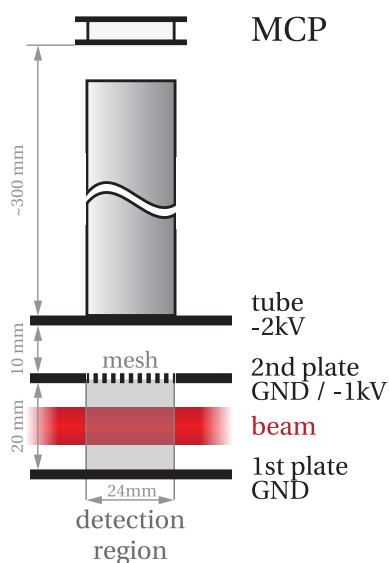


Figure 4.15: The time-of-flight mass spectrometer to detect the Penning ions.

4.3.3 Detection

Detection of Collision Products

The detector for the Penning ions, the time-of-flight mass spectrometer (TOF-MS), has a Wiley-McLaren design [89] as shown in figure 4.15. The two plates next to the merged beam are kept on ground potential, allowing the Penning ions formed inside to travel freely. Penning ions created outside these first two plates are extracted from the beam by the field from the tube of the TOF-MS. Therefore only collisions occurring between the first two plates can be detected.

For a very short time (≈ 300 ns), the second plate is set to 1000 V. All Penning ions which are under the mesh in the second plate, i.e. inside the detection region, at this moment are accelerated towards the detector's MCP by this pulse.

As shown in figure 4.16, the TOF-MS has a mass resolution of $R \approx 30$, which is high enough to separate the different dissociative channels of the collision products, e.g. NH_2^+ and NH_3^+ if NH_3 is present in the detection region. Please note that the gases in figure 4.16 had been leaked in shortly after each other in order to calibrate the TOF-MS. The unphysical findings, such as the peak at 19 u for ND_3 for example, is believed to originate from the $\text{D} \longleftrightarrow \text{H}$ exchange reactions in the improperly flushed gas line.

Energy Resolution

A time-sliced detection, due to the pulsing of the TOF-MS in our apparatus, increases the energy resolution of the merged beam experiment tremendously [35].

In our setup only those molecules which are inside the detection region at the time the TOF-MS is pulsed are detected. As the opening time of the sources are short compared to the total

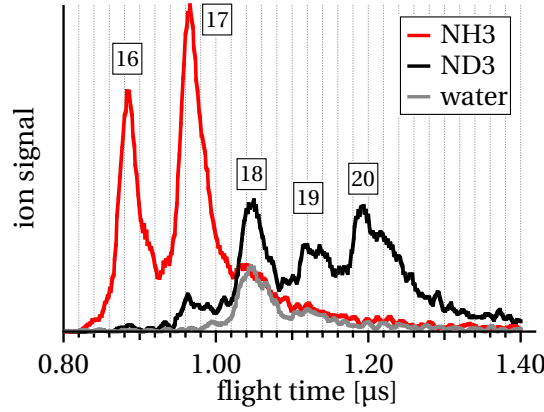


Figure 4.16: Recorded ion signal of the TOF-MS due to Penning ionization of different gases leaking into the detection chamber with Ne^* .

flight time of the particles and the diameter of the detection region is small compared to the total flight distance, only a very small range of velocities are present in the detection region during the TOF-MS pulse. A geometric illustration of this argument is displayed in figure 4.17. The mean velocity v_i for the two sources ($i = 1$ or $i = 2$, respectively) is

$$v_i = \frac{d_{MS} - d_{Si}}{t_{MS} - t_{Si}}, \quad (4.1)$$

where d_{MS} is the position of the TOF-MS and d_{Si} the position of the source i . The times are labeled accordingly: t_{MS} is the time the TOF-MS is pulsed and t_{Si} is the time the source i is triggered. In order to estimate the maximum velocity spread, we calculate the minimum v_{imin} and maximum velocities v_{imax} that can be detected.

$$v_{imin} = \frac{d_{MS} - d_{Si} - \frac{1}{2}\Delta d_{MS}}{t_{MS} - t_{Si} + \frac{1}{2}\Delta t_{Si}} \quad (4.2)$$

$$v_{imax} = \frac{d_{MS} - d_{Si} + \frac{1}{2}\Delta d_{MS}}{t_{MS} - t_{Si} - \frac{1}{2}\Delta t_{Si}}, \quad (4.3)$$

where Δt_{Si} is the opening time of the source i and Δd_{MS} is the size of the detection area. As the length of the pulse to detect the ions is only 300 ns it is neglected in this calculation. The uncertainty of the starting position of the molecules can be assumed to be zero as this uncertainty is already covered by the opening time of the source. The velocity spread is therefore

$$\Delta v_i = \frac{(d_{MS} - d_{Si}) \Delta t_{Si} + (t_{MS} - t_{Si}) \Delta d_{MS}}{(t_{MS} - t_{Si})^2 - \frac{1}{4}\Delta t_{Si}^2}. \quad (4.4)$$

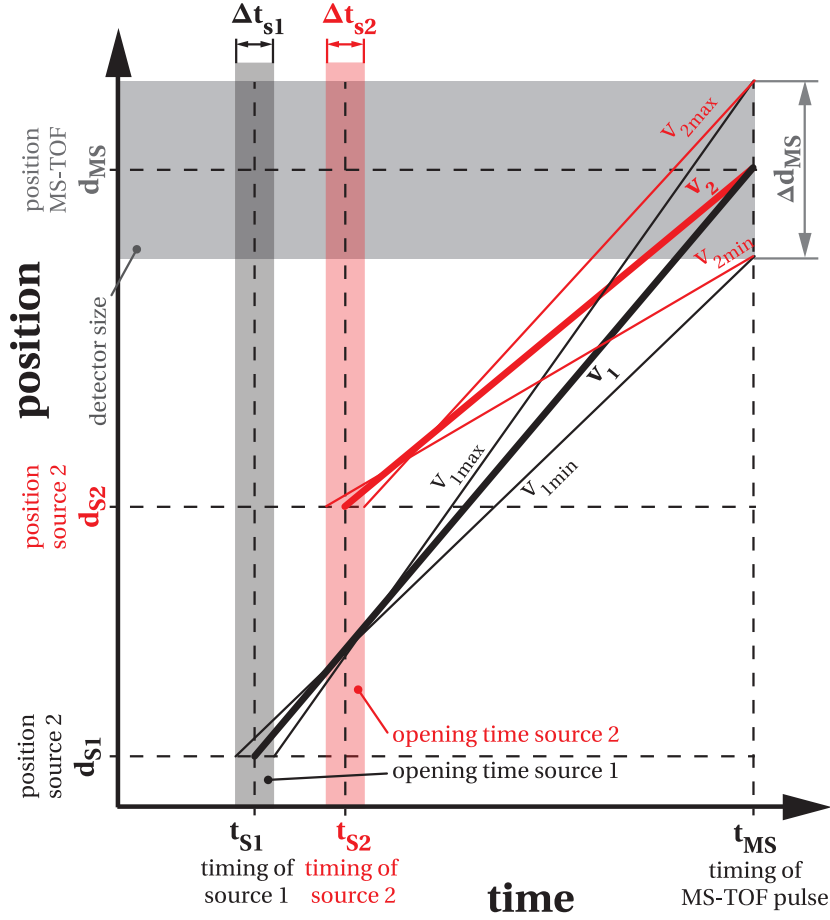


Figure 4.17: Schematic derivation of the energy resolution with a pulsed TOF-MS. The distances and times are arbitrarily scaled in order to emphasis the dependencies.

As in our experiment the flight time is much longer than the opening time of the sources and as the size of the detector is much smaller than the distance between source and detector, i.e. $\Delta t_{Si} \ll (t_{MS} - t_{Si})$ and $\Delta d_{MS} \ll (d_{MS} - d_{Si})$, the spread in the beam velocity can be approximated by

$$\Delta v_i = \left(\frac{\Delta t_{Si}}{t_F} \right) v_i, \quad (4.5)$$

where $t_F = t_{MS} - t_{Si}$ is the flight time of the particles. With the properties of the presently used sources as given in table 4.1 the velocity spread is less the 3% of the beam velocity.

In order to estimate the total uncertainty in collision energy the velocity spread in the transversal velocity has to be added. The transversal spread is already limited by the transversal acceptance of the guides to less the $\pm 10 \text{ m/s}$ for the guided particles.

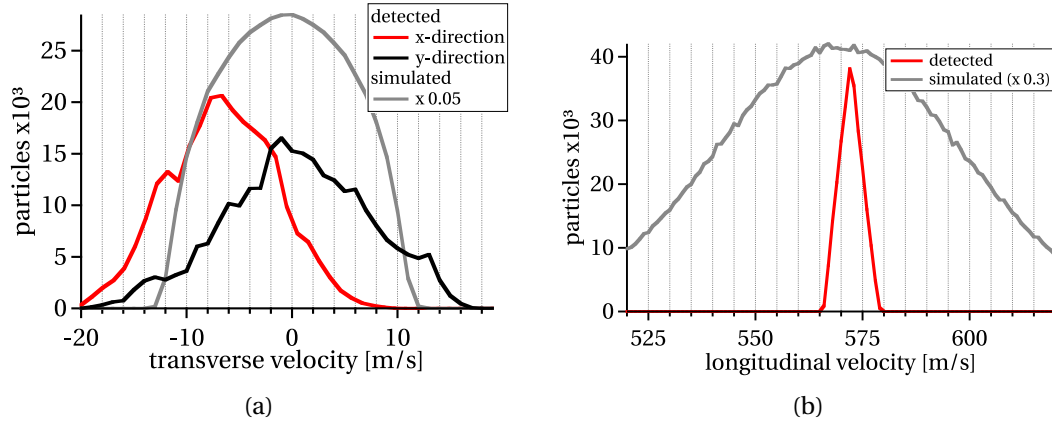


Figure 4.18: Simulated velocity distribution for Ne^* with a pulsed TOF-MS. An atom is counted as detected (red and black lines) if it is in the detection when the TOF-MS is pulsed. The gray line illustrates the distribution of the initially simulated particles. For better comparison the graphs for the initially simulated particles are scaled down as indicated.

Simulated Energy Resolution

Our trajectory simulation program gives us the possibility to simulate the effect of the pulsed detection and provides us a more detailed analysis of the spread in the collision energy. For the simulations in figure 4.18 we have calculated the path of 10^7 particles through the guide. For the initial longitudinal velocity distribution a gaussian distribution around 570 m/s with a width of $\pm 70 \text{ m/s}$ (gray line in fig. 4.18b) was assumed. For the transversal velocities a geometric cutoff was chosen, which limited the magnitude of the transversal velocity to less than 12 m/s (gray line in 4.18a). The source had an opening time of $40 \mu\text{s}$. The start time of the particles were randomly distributed during the opening time of the source. All particles which were 3.6 ms after the source was opened in the detection region were counted as “detected”. The velocity distribution of those particles are displayed as red and black lines in figure 4.18.

Figure 4.18a illustrates the energy spread in the transversal directions. Noteworthy is that the distribution in the x-axis is not centered around 0 m/s . This is a result of the curvature. The distribution in the y-axis, where no curvature is acting, is centered around 0 m/s .

In figure 4.18b the improvement in longitudinal energy resolution due to the pulsed TOF-MS can be clearly seen. The gray curve shows the velocity distribution of all the particles which leave the source. This distribution is with $\approx 2 \text{ K}$ (FWHM 70 m/s) already very cold. But due to the long flight time, the small detection region and the pulsing of the TOF-MS, the detected velocity distribution was reduced by one order of magnitude (FWHM 7 m/s) and the corresponding uncertainty in collision energy even by two orders of magnitude.

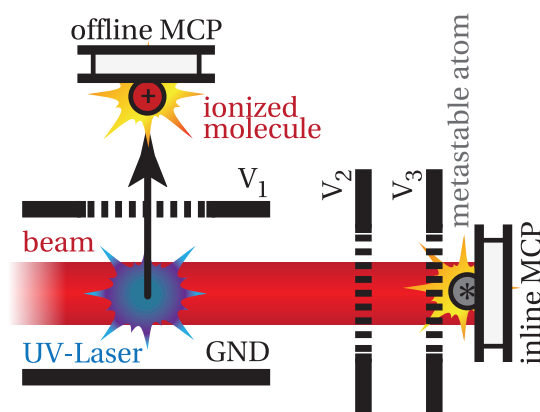


Figure 4.19: The detectors for the reactant beams. The density of ammonia is measured via a REMPI scheme, while the metastable Ne^* are directly detected via the inline MCP.

Monitoring of the density of the reactants

An accurate calculation of the cross section demands for a precise knowledge of the flux of the reactants (see equation 2.19). This information is gained in real time by the detectors in the detector chamber. The density of the metastable Ne^* atoms can easily be measured by the inline MCP (see figure 4.19). The excitation energy of Ne^* is high enough to strike electrons out of the metal surface of the MCP. These electrons are subsequently detected.

Two meshes are in front of the inline MCP. The first one, further away from the MCP, is kept at a positive voltage ($V_2 \approx 10\text{V}$). This first mesh prevents the detection of Penning ions, which have been created between the TOF-MS and this mesh, on the inline MCP. This would disturb the measured Ne^* density. The second mesh is set to a voltage with a higher absolute value but inverted polarity ($V_3 \approx -20\text{V}$) to assure that only neutral particles can reach the inline MCP.

For the detection of the ammonia molecules we use REMPI to ionize ammonia molecules that are in a certain rotational state. These ions are accelerated to the *Offline MCP*. The detection scheme is identical to the REMPI detection in the velocity filter experiment (see section 3.2.3 *Detection* on page 52) except for the lack of any mass resolution as the flight time in this setup is too short to discriminate between different masses.

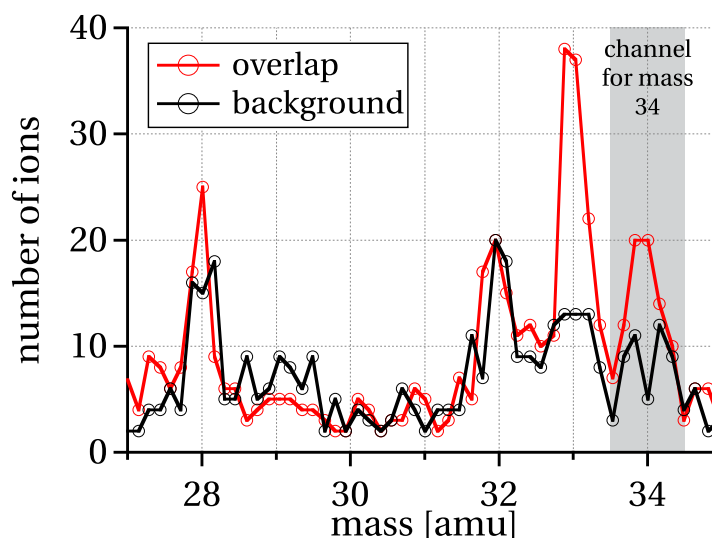


Figure 4.20: Measured traces of the TOF-MS with overlap settings (red) and with background settings (black) for the $\text{Ne}^* + \text{CH}_3\text{F}$ reaction. Ion counts within the shaped area are considered to have a mass of 34 amu.

4.4 Measurements

For each collision energy we want to investigate, the necessary collision velocity is calculated. As we normally operate the source of the electric guide (source 2 in fig. 4.1) at room temperature, we adjust the velocity of the metastable atoms of the magnetic guide to achieve the calculated collision velocity.

The timings for the two sources and the TOF-MS pulse are calculated so that both beams overlap right in the detection region of the TOF-MS when the TOF-MS is pulsed. As the pulsed TOF-MS detects only a very small fraction of the longitudinal velocities (see figure 4.18b) of the beams, the timings of the sources relative to the TOF-MS pulse defines the velocities which are observed by the TOF-MS. From the timings of the source and the observed velocities of the two beams, we can calculate the arrival times of the observed velocities at the reactant detectors in the detection chamber. The temperature of the Ne source (source 1 in fig. 4.1) is changed until the pulse center of the Ne^* pulse arrives at the inline MCP (fig 4.19) approximately at the time when the observed velocities will arrive. As the observed velocities are completely defined by the timings of the sources and the TOF-MS pulse, we do not have to control the average beam velocities of the two beams very strictly. The densities of the reactants with the observed velocities are measured in real time and are used to normalize the measured reaction rate. Therefore a change in beam velocities is not expected to have an influence on the measured ratios. As a higher number of product ions will lower the statistical error of our measurements, we try to keep the average beam velocities close to the observed velocities. The settings where both pulses overlap in the detection zone when the TOF-MS is pulsed, as described above, are called *overlap settings*. In order to determine the influence of the residual background gas, we change the timing of the sources to the so-called *background setting*, right

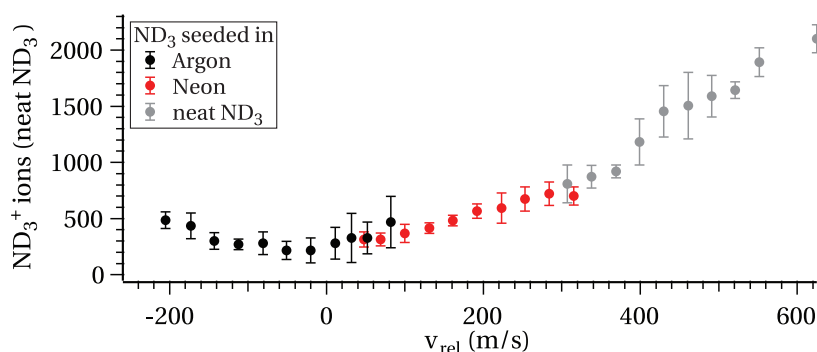


Figure 4.21: Normalized relative reaction rates for the $\text{Ne}^* + \text{ND}_3$ reaction as a function of collision energy. The velocity of the Ne^* was controlled by the source temperature. The velocity of the ND_3 was changed by different seeding gases (as labeled).

after each measurement with overlap settings. With the background settings only the center of the pulse of the metastable atoms is in the detection region when the TOF-MS is pulsed, while the beam of the polar molecules passed the detection region just before. Therefore we expect to record only Penning ions originating from collisions of the metastable atoms with the residual gases. As those Penning ions are also present in an overlap measurement, we need to know the rate of their creation to subtract it from the overlap measurement.

We integrated the ion signal of the TOF-MS with the above described settings over some minutes (12 min to 30 min), depending to the total ion yield. Typically we could record a few hundred ions in one measurement which contained 15,000 to 40,000 single beam collisions. Figure 4.20 shows the traces of the TOF-MS for such a measurement with overlap settings (red line) and with background settings (black line). In order to obtain results for the individual dissociation products, we divided the signal trace of the TOF-MS in channels which we addressed to integer atomic mass units. One of these channels is shown exemplary for the mass 34 amu as the gray shaped area in figure 4.20.

The difference between the ion signal of an overlap and a background measurement for each mass channel is considered to be the relative yield of the corresponding product ion of the Penning ionization.

Such a pair of measurements is repeated several times (3 to 5 times) to estimate the statistical fluctuations of our measurements. This procedure was repeated for each collision energy. In order to check the results of consistency, the same collision velocity can be reached by different beam velocity. Such a measurement is shown in figure 4.21. In this measurement the velocity of the Ne^* beam was tuned by changing the source temperature between 200 K and 340 K. The beam average velocity of the ND_3 beam was changed by using different seed gases (black symbols: ND_3/Ar , red symbols: ND_3/Ne , and gray symbols: neat ND_3). This provided us the possibility to vary the collision energy over a wide range. The number of Penning ions of the $\text{Ne}^* + \text{ND}_3$ collisions were counted over the same period of time for each measurement. The possibility to achieve the same collision energies with different laboratory frame velocities or by interchanging the velocities of the two particles provides a systematic check for

the consistency of the results. In figure 4.21 this can be seen in the matching overlap of the ion counts for different ND₃ velocities due to different seeding around 30 m/s and at 310 m/s. Especially changing the sign of the relative velocity should not change the reaction rate and such a measurement should therefore be symmetric around $v_{coll} = 0$. Within the experimental uncertainty, this is the case in for the measurement shown in figure 4.21.

As shown in figure 4.20, we are able to count single product ions, therefore we know the absolute rate of the reaction. Unfortunately it is experimentally very challenging to obtain absolute values for the reactant densities. Up to now we could not calibrate the signal of the reactant detection (see section 4.3.3 *Monitoring of the density of the reactants*). Therefore we can presently measure only relative rate constants and cross sections.

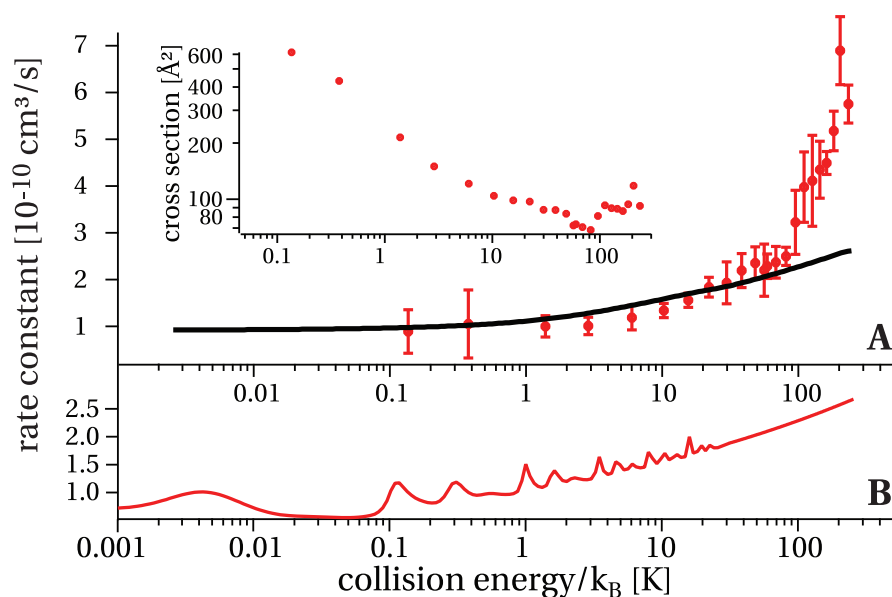


Figure 4.22: Experimental (red symbols) and calculated (lines) rate constants at different collision energies. The black lines show the calculations using a pure van der Waals potential the gray line the ones using a Lennard-Jones potential. Both are convoluted by a 30 m/s-wide Gaussian to account for the experimental resolution. The inset shows the experimental cross section. Panel B: Non-convoluted calculated rate constants (black: pure van der Waals interaction; gray: Lennard-Jones potential); weak shape resonances above 25 K are not shown.

4.5 Results

4.5.1 Reaction Rates

Penning Ionization of ND_3 and NH_3 by Metastable Ne^*

The measured rate constant for the $\text{ND}_3 + \text{Ne}^*$ reaction is shown as red symbols in figure 4.22 A. The error bars indicate the statistical fluctuations of the three to five replicate measurements which have been averaged for each data point. The lines in figure 4.22 A shows the calculated rate constant, using the multichannel quantum defect (MQDT) theory [116–119], convoluted with the estimated 30 m/s resolution of our experiment (see fig. 4.18). For the black line a pure van der Waals potential was used, for the gray line a Lennard-Jones potential with a well depth of 2.5 K. This calculation has been performed by Krzysztof Jachymski, Michał Hapka and Zbigniew Idziaszek of the University of Warsaw. We used this calculation to scale our measured relative constants to absolute values.

Their non-convoluted data is shown in figure 4.22 B. This curve shows many resonances which are presently not observable in our measurements. For the lowest studied collision energies, this model had to include 7 partial waves; in the highest range almost 100 partial waves are required to converge the cross section.

The MQDT model describes the short-range processes by two quantum defect parameters:

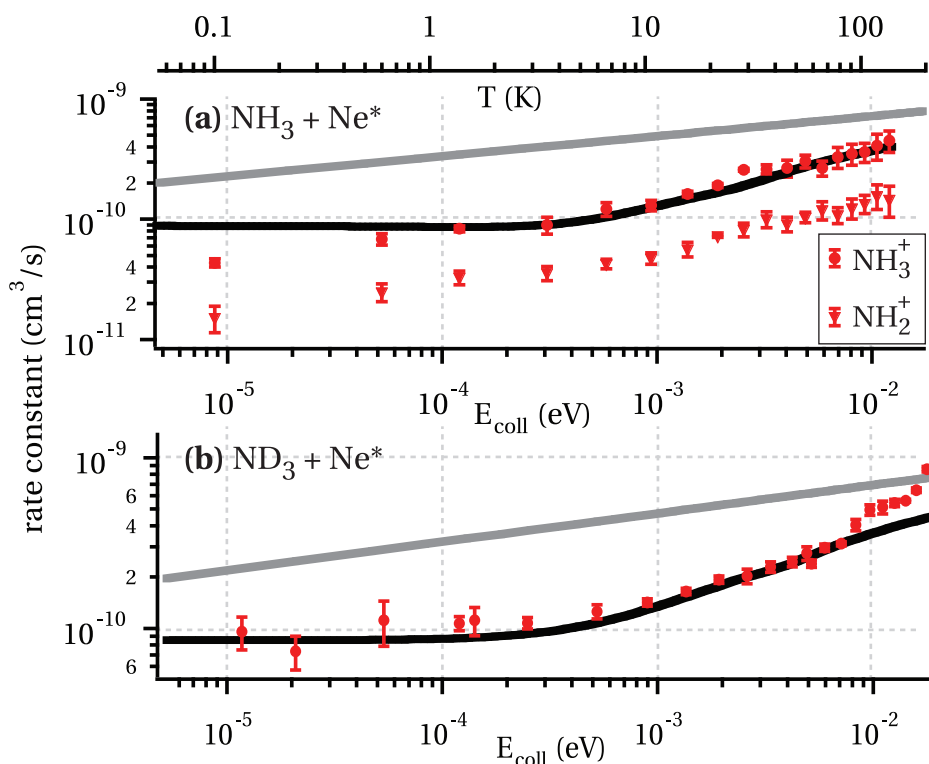


Figure 4.23: Rate constants for (a) the $\text{Ne}^* + \text{NH}_3$ reaction and (b) the $\text{Ne}^* + \text{ND}_3$ reactions. In both panels the red symbols are the experimental data and the black lines are the results of the MQDT calculations. The gray lines show the rate predicted on the basis of equation 2.35 assuming a potential $V_0 \propto R^{-6}$ of the intermediate complex. Panel (a) the circles (triangles) show the rate constant for the channel producing NH_3^+ (NH_2^+) products. In panel (b) the sum of ND_3^+ and ND_2^+ is shown [106].

y and s. The former describes the short-range reactivity, the latter is the scattering length corresponding to the full potential. The model requires that the energy and length scales can be separated between the reaction process and the long-range scattering. The suitability of this approach was confirmed in the theoretical reproduction of the results by Henson *et al.* [29] for the $\text{Ar} + \text{He}^*$ Penning ionization [116].

The measured reaction rates of the $\text{NH}_3 + \text{Ne}^*$ reaction are shown in figure 4.23 (a), the results of the $\text{ND}_3 + \text{Ne}^*$ reaction is displayed for comparison in panel (b). The circles in figure 4.23 (a) show the rate constant measured for NH_3^+ production and the triangles this rate for the NH_2^+ products. As before the results of the MQDT calculations (black lines in fig. 4.23) are used to normalize the measured relative rate constants to absolute values. This MQDT calculation used in both cases a Lennard-Jones potential with the same van der Waals coefficient. A well depth of the Lennard Jones potential of 1.1 K for NH_3 and 2.5 K for ND_3 was assumed.

The gray lines in figure 4.23 indicate the expected dependency of the rate constant from the collision energy according to the capture model of equation 2.35 assuming a $V_0(R) \approx R^{-6}$ long range potential of the intermediate complex NeNH_3^* or NeND_3^* , respectively. As shown in

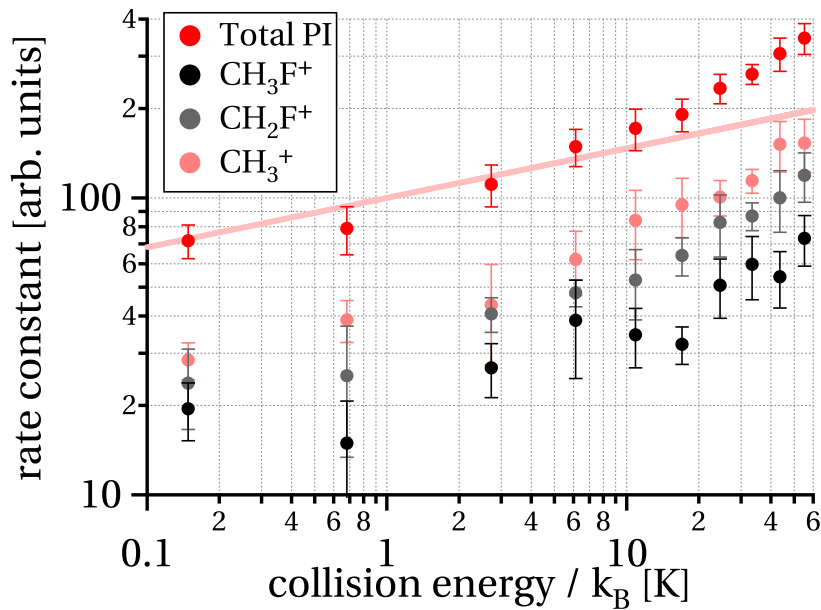


Figure 4.24: Reaction rates for the Penning ionization of CH_3F by metastable Ne^* , for the total reaction (red circles) and for the different dissociation channels (black, pink and gray circles). The pink line illustrates the theoretical expectations for potential $\propto R^{-6}$ according to equation 2.35 [107].

figure 4.23 this model predicts a linear relationship between $\log(k)$ and $\log(E_{\text{coll}})$. It is clearly visible that this simple model can not explain the measured rate constant in figures 4.23, as the slope (in a log-log plot) of both reaction is rising with rising collision energy.

The results of the MQDT calculations fit the experimental data much better. The rate constant in the central part of the investigated collision energies is reproduced very well. Only at the edges of the temperature range discrepancies seem to appear. For the $\text{Ne}^* + \text{ND}_3$ reaction the measured and calculated values disagree above 100 K. This finding can be rationalized by the growing influence for short-range potentials at higher collision energies. As the presently used MQDT calculations use a pure $V(R) \propto R^{-6}$ to model the long range interactions this model might fail once different potentials terms gain in importance. At the low-energy edge of our measurements a mismatch of MQDT calculations and experimental data might appear in the $\text{Ne}^* + \text{NH}_3$ reaction. At the lowest collision energies (100 mK) the MQDT calculations predict a significantly higher rate constant than we have measured (see fig. 4.23). The origin of this discrepancy at this point remains unclear.

Penning Ionization of CH_3F by Metastable Ne^*

The reaction rates of the $\text{CH}_3\text{F} + \text{Ne}^*$ in the range from 150 mK to 56 K are shown in figure 4.26. The reaction rate for the different dissociation channels CH_3F^+ (black), CH_2F^+ (gray) and CH_3^+ (pink) are displayed individually along with the total reaction rate ($\text{CH}_3\text{F}^+ + \text{CH}_2\text{F}^+ + \text{CH}_3^+$) (red). Unfortunately we were not able to investigate the dissociation into CHF^+ , as this ion has

the same mass as O_2 . The rather high signal of O_2^+ due to collisions of Ne^* with the residual gas caused a background signal on this mass channel too high to resolve any CHF^+ signal. Presently there are no MQDT calculations available for this reaction. For a comparison with the capture theory, the expectation according to equation 2.35 for an attractive potential $V_0 \propto R^{-6}$ is shown as the rose line. This line reproduces the expected data below 10 K rather well while it strongly differs from the experimental data at higher energies. We conclude that the long-range part of the potential is well-described by the R^{-6} dependence while strong deviations appear at short distances.

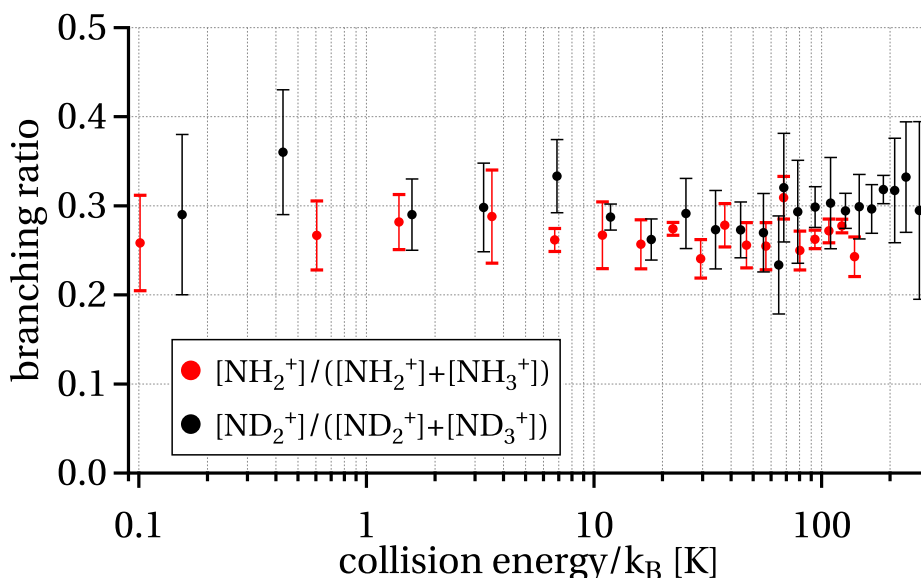


Figure 4.25: Branching ratios of the ND₃ and NH₃ reaction with metastable Ne^{*} as a function of collision energy.

4.5.2 Stereochemistry

Penning Ionization of ND₃ and NH₃ by Metastable Ne^{*}

In figure 4.25 the measured branching ratio of the Penning ionization of ND₃ und NH₃ by metastable Ne^{*} in the range from 0.1 K to 250 K is shown. Although the ratio was recorded over three orders of magnitude in temperature for two different reactions, we observed a constant ratio within our error bars.

This is not only in contradiction to the theoretical expectation of section *Stereochemistry* (sec. 2.3) but also with the measurement at higher temperature. In the range from 0.035 eV to 0.2 eV, corresponding to temperatures around 400 K to 2300 K, Ben Arfa *et al.* measured the branching ratio for the NH₃ + Ne^{*} reaction [42]. Although the value of Ben Arfa *et al.* for collision energies around 250 K is comparable with our measurements, the behavior of the recorded ratios is very different. While the branching ratio measured by Ben Arfa *et al.*² rises exponentially from ≈ 0.39 at 400 K to ≈ 0.45 at 2300 K, the ratio in our measurements stays constant between 0.1 K and 140 K

In the view of the arguments of section *Stereochemistry* (sec. 2.3), one might conclude from our findings that within our temperature range the collision energies are so low that the system has to follow one MEP very closely.

There is no PES available of the ND₃–Ne^{*} or NH₃–Ne^{*} complex, but from chemically similar complexes one can assume that there is a deep well for the bond of Ne^{*} to the lone pair of ND₃. In the case of the H₂O–Ne^{*} complex, there is a 400 meV deep well along the O-lone

²Please note that in [42] the branching was measured by the $[\text{NH}_2^+]/[\text{NH}_3^+]$. In order to compare it with our measurements for ND₃, it has been converted to the branching ratio $[\text{NH}_2^+]/([\text{NH}_2^+]+[\text{NH}_3^+])$.

pair \cdots Ne * coordinate, while there is barely any minimum along the O–H \cdots Ne * coordinate [45]. Accordingly we expect the Ne $^*\cdots$ NH $_3$ complex to be favored over the Ne $^*\cdots$ HN $_3$ complex, leading to a domination of the NH $_3^+$ (ND $_3^+$ respectively) channel when the complex have enough time to funnel in the energetic preferable configuration. If the reactions is happening at a very short time scale, leaving the complex insufficient time to funnel in its energetically preferred configuration, a branching ratio which reflects the geometric distribution of the involved orbitals is expected. Ben Arfa *et al.* use this argument to rationalize their finding of an increased production of NH $_2^+$ for rising collision energies [42]. Applying these considerations to our experiment, we can estimate the collision time t_c by

$$t_c = \frac{b_c}{v_{rel}}, \quad (4.6)$$

where b_c is the critical impact parameter as defined in equation 2.33. As $b_c \approx \sqrt{\sigma}$ we can use the cross section obtained by the MQDT calculations to estimate the collision times. In case of NH $_3$ we obtain $b_c(15\text{ m/s}) = 25\text{ \AA}$ and $b_c(600\text{ m/s}) = 10\text{ \AA}$, which the corresponding collision times of $t_{c,low} = 170\text{ ps}$ and $t_{c,high} = 1.7\text{ ps}$ for the low- and high-energy collisions.

The rotational period of ND $_3$ in the most populated state $J_K = 1_1$ is $t_{rot} = 2\text{ ps}$. Following the argument above, the branching ratio for high collision energy should approaching the geometric value, while for the collision energies the complex would have enough time to funnel into the preferred configuration, as $t_{c,low} \gg t_{rot}$. In contrast to this expectations we have measured a constant branching ratio.

A possible explanation for the failure of the model might be the fact that the de Broglie wavelength of the reactants cannot be neglected anymore in our temperature regime. As the de Broglie wavelength grows with reduced energy, the reaction can not be described as the classical motion of a point on the PES anymore. The reaction will then cover bigger parts of the PES simultaneously, possible spanning over different channels and might tunnel through barriers. This in turn could again lead to an geometric branching ratio.

At the lowest collision velocity of our experiments, the de Broglie wavelength is more than 10 \AA . Up to a collision velocity of 200 m/s (15 K), the size of the reactants stays well above 1 \AA . Although the de Broglie wavelength might be considerably high for the low energy collisions to invalidate classical assumptions, this should not be the case for the high collision energies. Another effect that has to be considered is that as we decrease the collision energy the cross section of the Penning ionization increases (see inset of figure 4.22 A), which shifts the (classical) turning point to greater distances (see equation 2.33). If the potentials of the different channels are nearly identical at the position where the reaction happens a geometric branching ratio is expected as the energetic differences of the channels have not come into play yet. The potentials along the O-lone pair \cdots Ne * reaction coordinate and along the O–H \cdots Ne * coordinate differ only for distances $< 8\text{ \AA}$ [45]. If we assume the PES of the NeNH $_3^*$ (NeND $_3^*$) complex to be similar to the NeH $_2$ O * complex, this argument might explain our finding of a constant branching ratio if the turning point is above 8 \AA in the observed temperature range. Interestingly the observation of a constant branching ratio continued in the reaction CH $_3$ F +

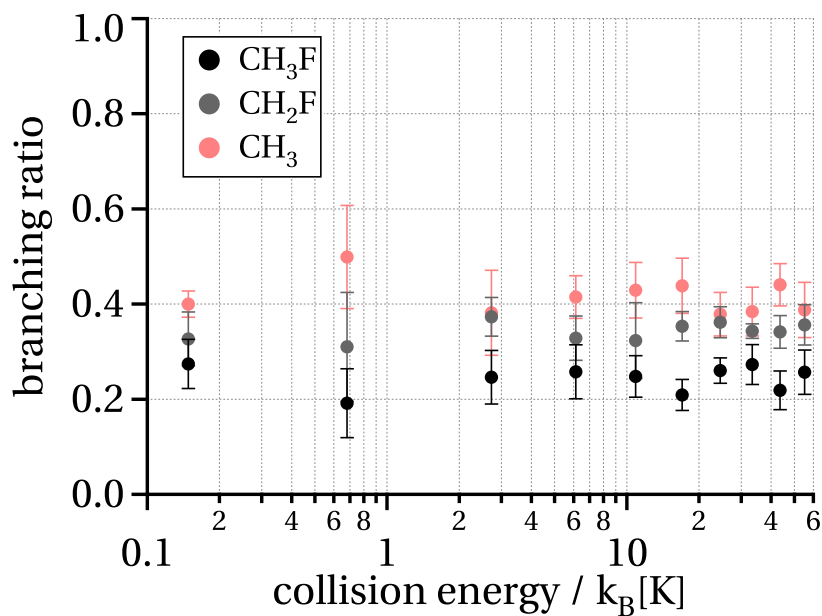
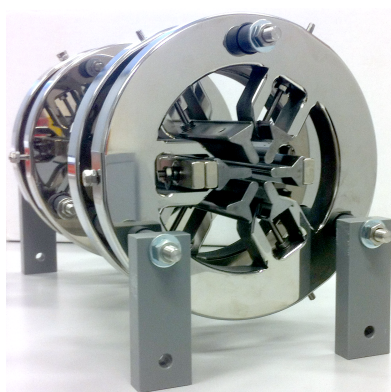
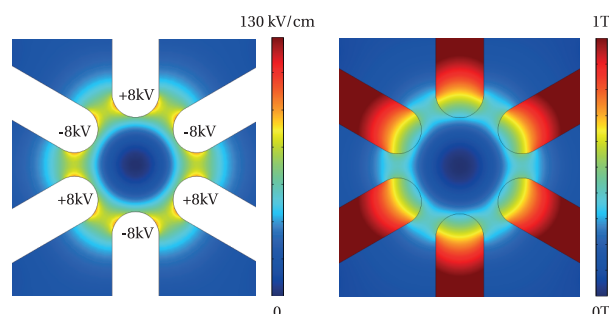


Figure 4.26: Branching ratios for the different dissociation channels of the Penning ionization of CH_3F by metastable Ne^* . The branching ratio is defined as $[i]/([\text{CH}_3\text{F}] + [\text{CH}_2\text{F}] + [\text{CH}_3])$.

Ne^* as well. As shown in figure 4.26, the branching ratios of all three observed dissociation channels are constant between 150 mK and 56 K. As for the NH_3 and ND_3 the reason for this findings remains unclear.



(a) Photo of the projected reaction guide.



(b) Electric field (left) and magnetic field strength (right) of the reaction guide.

Figure 4.27: The reaction guide.

4.5.3 Improvements of the Experimental Apparatus

Although our apparatus performs very much as planned, there are already some ideas for further improvement. A reaction guide, as shown in figure 4.27a, which combines a magnetic and an electric guide, could be added just after the curved guides where the beams are merged. This would confine the merged beams over an arbitrarily long distance. The combination of magnetic and electric guiding in one single guide demanded a rather complex design. As a consequence the magnetic and electric field strength in the reaction guide will be much weaker as in the bent guides of the merged beam experiment (compare figure 4.27b with figure 4.4a and 4.9a). But as this reaction guide will be straight those fields are sufficient to confine all particles which successfully passed the curved guides. Therefore the density of the reactants in such a reaction guide would be constant over the full length of the reaction guide. The reactants will spend a long time inside this guide causing the collision probability to increase, which would make the detection of small cross sections more likely.

The detection of the reaction production could be achieved at the end of the reaction guide by a quadrupole mass spectrometer if the products are guidable. Reactions leading to unguidable products might be investigated by the depletion of the reactant densities or by the appearance of those products in the background pressure of the chamber of the reaction guide. Inelastic scattering could be investigated via changes in the vibrational or rotation energy distribution of the reactants.

4.6 Conclusions

The studied the reactions of NH_3 , ND_3 , and CH_3F with metastable Ne^* in an unprecedented temperature range spanning three order of magnitude, from above 100 K down to about 100 mK [106, 107]. In case of the $\text{Ne}^* + \text{ND}_3$ and the $\text{Ne}^* + \text{NH}_3$ reaction the measured rate constants at temperatures below 100 K fit well to the theoretical predictions of the multichannel quantum defect (MQDT) theory [116–119]. For higher temperature the measured rate constant of the $\text{Ne}^* + \text{ND}_3$ differs from the MQDT calculation significantly. The rate constant of the reaction $\text{Ne}^* + \text{NH}_3$ is well described by the MQDT model over the whole investigated length, expect for the measurement with the lowest collision energy (100 mK).

For the $\text{Ne}^* + \text{CH}_3\text{F}$ reactions there are yet no theoretical predictions available. But at least for the collision energies below 20 K, the reaction rates is consistent with the assumption of a $V_0 \propto R^{-6}$ potential.

The most remarkable finding of our reaction studies so far is the constant branching ratio of the dissociation channels of the reactions of Ne^* with NH_3 , ND_3 and CH_3F . In our measurements all possible channels remain a constant probability from 200 K down to 100 mK. Which effect causes this unexpected result is yet unknown. Of the three rationalizations which are commonly used to explain the branching ratio for reactions at room temperature and above, two fail to explain the behavior in our temperature range. The model which uses to explain the constant ratio by the shifting of the turning point to large distances for low collision energies has to be investigated more deeply.

We were able to investigate those reactions in this very low temperature regime by building an new merged beam apparatus, which bends two beams of neutral particles into an overlapping, parallel movement. To my knowledge this was the first time this was achieved with two bent beams. The use of a magnetic guide and an electric guide to bend the beams allows us to investigate reactions between paramagnetic particles and polar molecules, providing us with a very wide range of possible reactants.

The guiding of two paramagnetic particles (Ne^* and Ar^*) and five polar molecules (NH_3 , ND_3 , $\text{SO}_2\text{CH}_3\text{F}$, and CHF_3) has been experimentally proven, for six more particles (Kr^* , Xe^* , O_2 , CO^* , CH_2O , and H_2O) guiding should be possible according to our trajectories simulations. Many more particles are expected to be guidable in our apparatus.

5 Conclusions

The aim of my thesis was the development of an experimental device which will enable us to observe chemical reactions at such low temperatures where these reactions could not be observed so far. Very much like in all of scientific history¹, the way to develop such a device was not as straightforward as it might look like in retrospect. In our first experiment, the *velocity filter* experiment, we were able to produce a beam of ND₃ with a translational temperature down to a few K. Although we gained a very deep insight in the dynamics of a *velocity filter* [120–122], we could not reduce the rotational temperature and the achieved densities were too low to use this tool to in a collision experiment.

But, again history is repeating itself. The experience and knowledge we gained in the *velocity filter* experiment were vital for the success of our second experiment, the *merged beam* experiment [106, 107]. With this experiment we were able to lower the temperatures at which the investigated reactions, Ne^{*} with ND₃, NH₃ and CH₃F, have been observed, by three orders of magnitude, down to the edge of the ultracold regime. The validity of the MQDT model in the temperature range between 100 mK and 200 mK could be proven for the reaction of NH₃ and ND₃ with Ne^{*}. All measured reaction showed unexpected constant branching ratio of the dissociative channels over the investigated temperature regime.

In order to reach such low collision velocities (down to 15 m/s) we extended the merged beam method to neutral-neutral reactions. The newly apparatus is only operating since a few month but already three different reactions has been studied. As I write these words we successfully guided two metastable atoms in the magnetic beam and five polar molecules. Many more polar molecules and paramagnetic particles are expected to be guidable as well. Therefore I can end my thesis not only by looking back to measurements I could participate in, but also with a very promising outlook for many interesting experiments to come.

¹I would dare to say that this was the case for nearly all developed experimental devices.



Bibliography

- [1] S. Symons, *Ancient Egyptian astronomy: Timekeeping and Cosmography in the New Kingdom*, Ph.D. thesis, University of Leicester (1999).
- [2] R. V. Krems, *Cold Controlled Chemistry*, Phys. Chem. Chem. Phys. **10**, 4079 (2008).
- [3] G. Roddenberry, J. D. F. Black, and B. Justman, *Introductory Sequence of the Star Trek TV-Series* (1966).
- [4] E. Herbst and J. T. Yates, *Introduction: Astrochemistry*, Chem. Rev. **113**, 8707 (2013).
- [5] A. Migdall, J. Prodan, W. Phillips, T. Bergeman, and H. Metcalf, *1st Observation of Magnetically Trapped Neutral Atoms*, Phys. Rev. Lett. **54**, 2596 (1985).
- [6] E. S. Shuman, J. F. Barry, and D. DeMille, *Laser Cooling of a Diatomic Molecule*, Nature **467**, 820 (2010).
- [7] J. F. Barry, E. S. Shuman, E. B. Norrgard, and D. DeMille, *Laser Radiation Pressure Slowing of a Molecular Beam*, Phys. Rev. Lett. **108**, 103002 (2012).
- [8] M. T. Hummon, M. Yeo, B. K. Stuhl, A. L. Collopy, Y. Xia, and J. Ye, *2D Magneto-Optical Trapping of Diatomic Molecules*, Phys. Rev. Lett. **110**, 143001 (2013).
- [9] J. Riedel, S. Hoekstra, W. Jaeger, J. J. Gilijamse, S. Y. T. van de Meerakker, and G. Meijer, *Accumulation of Stark-Decelerated NH Molecules in a Magnetic Trap*, Eur. Phys. J. D **65**, 161 (2011).
- [10] J. D. Weinstein, R. deCarvalho, T. Guillet, B. Friedrich, and J. Doyle, *Magnetic Trapping of Calcium Monohydride Molecules at Millikelvin Temperatures*, Nature **395**, 148 (1998).
- [11] R. Fulton, A. I. Bishop, and P. F. Barker, *Optical Stark Decelerator for Molecules*, Phys. Rev. Lett. **93**, 243004 (2004).
- [12] R. Fulton, A. I. Bishop, M. N. Shneider, and P. F. Barker, *Optical Stark Deceleration of Nitric Oxide and Benzene Molecules Using Optical Lattices*, J. Phys. B **39**, S1097 (2006).
- [13] R. Fulton, A. I. Bishop, M. N. Shneider, and P. F. Barker, *Controlling the Motion of Cold Molecules with Deep Periodic Optical Potentials*, Nature Phys. **2**, 465 (2006).

Bibliography

- [14] H. L. Bethlem, G. Berden, and G. Meijer, *Decelerating Neutral Dipolar Molecules*, Phys. Rev. Lett. **83**, 1558 (1999).
- [15] N. Vanhaecke, U. Meier, M. Andrist, B. H. Meier, and F. Merkt, *Multistage Zeeman Deceleration of Hydrogen Atoms*, Phys. Rev. A **75**, 031402 (2007).
- [16] E. Narevicius, A. Libson, C. G. Parthey, I. Chavez, J. Narevicius, U. Even, and M. G. Raizen, *Stopping Supersonic Beams with a Series of Pulsed Electromagnetic Coils: An Atomic Coilgun*, Phys. Rev. Lett. **100**, 093003 (2008).
- [17] J. J. Gilijamse, S. Hoekstra, S. Y. T. van de Meerakker, G. C. Groenenboom, and G. Meijer, *Near-Threshold Inelastic Collisions Using Molecular Beams with a Tunable Velocity*, Science **313**, 1617 (2006).
- [18] M. Kirste, X. Wang, H. C. Schewe, G. Meijer, K. Liu, A. van der Avoird, L. M. C. Janssen, K. B. Gubbels, G. C. Groenenboom, and S. Y. T. van de Meerakker, *Quantum-State Resolved Bimolecular Collisions of Velocity-Controlled OH with NO Radicals*, Science **338**, 1060 (2012).
- [19] B. K. Stuhl, M. T. Hummon, M. Yeo, G. Quemener, J. L. Bohn, and J. Ye, *Evaporative Cooling of the Dipolar Hydroxyl Radical*, Nature **492**, 396 (2012).
- [20] B. C. Sawyer, B. K. Stuhl, D. Wang, and J. Ye, M. Ye, *Molecular Beam Collisions with a Magnetically Trapped Target*, Phys. Rev. Lett. **101**, 203203 (2008).
- [21] B. Rowe, G. Dupeyrat, J. Marquette, and P. Gaucherel, *Study of the Reactions $N_2^+ + 2 N_2 \longrightarrow N_4^+ + N_2$ and $O_2^+ + 2 O_2 \longrightarrow O_4^+ + O_2$ from 20 to 160 K by the CRESU Technique*, J. Chem. Phys. **80**, 4915 (1984).
- [22] I. Smith, *Reactions at Very Low Temperatures: Gas Kinetics at a New Frontier*, Angew. Chem. Int. Ed. Engl. **45**, 2842 (2006).
- [23] D. Willey, R. Timlin, J. Merlin, M. Sowa, and D. Wesolek, *An Experimental Investigation of Collisions of NH_3 with para- H_2 at the Temperatures of Cold Molecular Clouds*, Astrophys. J. Suppl. Ser. **139**, 191 (2002).
- [24] J. Toennies, W. Welz, and G. Wolf, *Molecular-Beam Scattering Studies of Orbiting Resonances and the Determination of van der Waals Potentials for H-Ne, Ar, Kr, and Xe and for H_2 -Ar, Kr, and Xe*, J. Chem. Phys. **71**, 614 (1979).
- [25] S. Chefdeville, Y. Kalugina, S. Y. T. van de Meerakker, C. Naulin, F. Lique, and M. Costes, *Observation of Partial Wave Resonances in Low-Energy O_2 - H_2 Inelastic Collisions*, Science **341**, 1094 (2013).
- [26] S. Chefdeville, T. Stoecklin, A. Bergeat, K. M. Hickson, C. Naulin, and M. Costes, *Appearance of Low Energy Resonances in CO-Para- H_2 Inelastic Collisions*, Phys. Rev. Lett. **109**, 023201 (2012).

- [27] V. Singh, K. S. Hardman, N. Tariq, M.-J. Lu, A. Ellis, M. J. Morrison, and J. D. Weinstein, *Chemical Reactions of Atomic Lithium and Molecular Calcium Monohydride at 1 K*, Phys. Rev. Lett. **108** (2012).
- [28] B. C. Sawyer, B. K. Stuhl, M. Yeo, T. V. Tscherbul, M. T. Hummon, Y. Xia, J. Klos, D. Patterson, J. M. Doyle, and J. Ye, *Cold Heteromolecular Dipolar Collisions*, Phys. Chem. Chem. Phys. **13**, 19059 (2011).
- [29] A. B. Henson, S. Gersten, Y. Shagam, J. Narevicius, and E. Narevicius, *Observation of Resonances in Penning Ionization Reactions at Sub-Kelvin Temperatures in Merged Beams*, Science **338**, 234 (2012).
- [30] S. Chervakov, X. Wu, J. Bayerl, A. Rohlfes, T. Gantner, M. Zeppenfeld, and G. Rempe, *Continuous Centrifuge Decelerator for Polar Molecules*, Phys. Rev. Lett. **112**, 013001 (2014).
- [31] M. Gupta and D. Herschbach, *A Mechanical Means to Produce Intense Beams of Slow Molecules*, J. Phys. Chem. A **103**, 10670 (1999).
- [32] M. Gupta and D. Herschbach, *Slowing and Speeding Molecular Beams by Means of a Rapidly Rotating Source*, J. Phys. Chem. A **105**, 1626 (2001).
- [33] M. S. Eliooff, J. J. Valentini, and D. W. Chandler, *Subkelvin Ccooling NO Molecules via "Billiard-Like" Collisions with Argon*, Science **302**, 1940 (2003).
- [34] R. Phaneuf, C. Havener, G. Dunn, and A. Muller, *Merged-Beams Experiments in Atomic and Molecular Physics*, Rep. Prog. Phys. **62**, 1143 (1999).
- [35] Y. Shagam and E. Narevicius, *Sub-Kelvin Collision Temperatures in Merged Neutral Beams by Correlation in Phase-Space*, J. Phys. Chem. C **117**, 22454 (2013).
- [36] H. Hotop and A. Niehaus, *Reactions of Excited Atoms and Molecules with Atoms and Molecules – 2. Energy Analysis of Penning Electrons*, Z. Physik **228**, 68 (1969).
- [37] F. Biondini, B. Brunetti, P. Candori, F. De Angelis, S. Falcinelli, F. Tarantelli, M. Teixidor, F. Pirani, and F. Vecchiocattivi, *Penning Ionization of N_2O Molecules by $He^*(2^3,1S)$ and $Ne^*(^3P_{2,0})$ Metastable Atoms: A crossed Beam Study*, J. Chem. Phys. **122**, 164308 (2005).
- [38] P. Siska, *Molecular-Beam Studies of Penning Ionization*, Rev. Mod. Phys. **65**, 337 (1993).
- [39] H. Feshbach, *Unified Theory of Nuclear Reactions*, Ann. Phys. **5**, 357 (1958).
- [40] A. Niehaus, *The Excited State in Chemical Physics, Part 2*, John Wiley & Sons (1981).
- [41] V. Čermák, *Penning Ionization Electron Spectroscopy I. Determination of Ionization Potentials of Polyatomic Molecules*, Collect. Czech. Chem. Commun. **33**, 2739 (1968).

- [42] M. Ben Arfa, B. Lescop, M. Cherid, B. Brunetti, P. Candori, D. Malfatti, S. Falcinelli, and F. Vecchiocattivi, *Ionization of Ammonia Molecules by Collision with Metastable Neon Atoms*, Chem. Phys. Lett. **308**, 71 (1999).
- [43] R. Locht, C. Servais, M. Ligot, F. Derwa, and J. Momigny, *The Dissociative Electroionization of Ammonia and Ammonia-D3 - 1. The NH^+ and NH_2^+ Dissociation Channels*, Chem. Phys. **123**, 443 (1988).
- [44] J. Bentley, *Potential-Energy Surfaces for Excited Neon Atoms Interacting with Water-Molecules*, J. Chem. Phys. **73**, 1805 (1980).
- [45] B. G. Brunetti, P. Candori, S. Falcinelli, F. Pirani, and F. Vecchiocattivi, *The Stereodynamics of the Penning Ionization of Water by Metastable Neon Atoms*, J. Chem. Phys. **139** (2013).
- [46] R. D. Levine, *Molecular Reaction Dynamics*, Cambridge University Press (2005).
- [47] M. H. G. de Miranda, A. Chotia, B. Neyenhuis, D. Wang, G. Quemener, S. Ospelkaus, J. L. Bohn, J. Ye, and D. S. Jin, *Controlling the Quantum Stereodynamics of Ultracold Bimolecular Reactions*, Nature Phys. **7**, 502 (2011).
- [48] B. Lescop, M. BenArfa, M. Cherid, G. LeCoz, G. Sinou, G. Fanjoux, A. LeNadan, and F. Tuffin, *Penning Ionization Electron Spectroscopy of the C_2H_2 Molecule by $\text{Ne}^* (3(3)P(2), 3(3)P(0))$ Metastable Atoms*, J. Electron. Spectrosc. Relat. Phenom. **87**, 51 (1997).
- [49] H. Bevsek and P. Siska, *A Vibrationally Adiabatic Theory of Molecular Penning Ionization*, J. Chem. Phys. **102**, 1934 (1995).
- [50] B. Brunetti, P. Candori, J. DeAndres, F. Pirani, M. Rosi, S. Falcinelli, and F. Vecchiocattivi, *Dissociative Ionization of Methyl Chloride and Methyl Bromide by Collision with Metastable Neon Atoms*, J. Phys. Chem. A **101**, 7505 (1997).
- [51] K. Ohno, T. Takami, K. Mitsuke, and T. Ishida, *State-Resolved Collision Energy-Dependence of Penning Ionization Cross-Sections for N_2 and CO_2 by $\text{He}^* 2^3\text{S}$* , J. Chem. Phys. **94**, 2675 (1991).
- [52] M. Yamato, S. Okada, V. Wu, H. Ohoyama, and T. Kasai, *Direct Observation of the Steric Effect in Penning Ionization Reaction of $\text{Ar}^* + \text{CHCl}_3 \longrightarrow \text{CHCl}_2^+ + \text{Cl} + e^- + \text{Ar}$* , J. Chem. Phys. **113**, 6673 (2000).
- [53] B. Brunetti, P. Candori, S. Falcinelli, T. Kasai, H. Ohoyama, and F. Vecchiocattivi, *Velocity Dependence of the Ionization Cross Section of Methyl Chloride Molecules Ionized by Metastable Argon Atoms*, Phys. Chem. Chem. Phys. **3**, 807 (2001).
- [54] H. Ohoyama, M. Yamato, S. Okada, T. Kasai, B. Brunetti, and F. Vecchiocattivi, *Direct Measurement of Oscillating Behavior in $\text{Ar}(^3P) + \text{CH}_3\text{Cl} \longrightarrow \text{Ar} + \text{CH}_3\text{Cl}^+ + e^-$ Ionization Cross Section by Velocity and Orientation Angle Selected Collisions*, Phys. Chem. Chem. Phys. **3**, 3598 (2001).

- [55] B. Brunetti, P. Candori, D. Cappelletti, S. Falcinelli, F. Pirani, D. Stranges, and F. Vecchiocattivi, *Penning Ionization Electron Spectroscopy of Water Molecules by Metastable Neon Atoms*, Chem. Phys. Lett. **539**, 19 (2012).
- [56] N. Balucani, A. Bartocci, B. Brunetti, P. Candori, S. Falcinelli, F. Palazzetti, F. Pirani, and F. Vecchiocattivi, *Collisional Autoionization Dynamics of $Ne^*(^3P_{2,0})-H_2O$* , Chem. Phys. Lett. **546**, 34 (2012).
- [57] E. Narevicius, A. Libson, M. F. Riedel, C. G. Parthey, I. Chavez, U. Even, and M. G. Raizen, *Coherent Slowing of a Supersonic Beam with an Atomic Paddle*, Phys. Rev. Lett. **98**, 103201 (2007).
- [58] J. Stark, *Die gegenwärtige Krisis in der deutschen Physik*, Verlag Joh. Ambr. Barth (Leipzig), (1922).
- [59] H. G. Bennewitz, W. Paul, and C. Schlier, *Fokussierung polarer Moleküle*, Z. Phys. **141**, 6 (1955).
- [60] H. L. Bethlem, G. Berden, F. M. H. Crompvoets, R. T. Jongma, A. J. A. van Roij, and G. Meijer, *Electrostatic Trapping of Ammonia Molecules*, Nature **406**, 491 (2000).
- [61] H. L. Bethlem, J. van Veldhoven, M. Schnell, and G. Meijer, *Trapping Polar Molecules in an AC Trap*, Phys. Rev. A **74**, 063403 (2006).
- [62] R. D. Johnson III (Editor), *NIST Computational Chemistry Comparison and Benchmark Database - NIST Standard Reference Database Number 101*, Release 16a, <http://cccbdb.nist.gov/> (2013).
- [63] N. Ashfold, R. Dixon, R. Stickland, and C. Western, *2+1 MPI Spectroscopy of B^1E' State NH_3 and ND_3 - Rotational Analysis of the Origin Bands*, Chem. Phys. Lett. **138**, 201 (1987).
- [64] S. Urban, R. Dcunha, K. Rao, and D. Papousek, *The $\Delta K = \pm 2$ Forbidden Band and Inversion Rotation Energy-Levels of Ammonia*, Can. J. Phys. **62**, 1775 (1984).
- [65] L. Fusina, G. Dilonardo, and J. Johns, *The ν_2 and ν_4 Bands of $14ND_3$* , J. Mol. Spectrosc. **118**, 397 (1986).
- [66] R. Nuckolls, L. Rueger, and H. Lyons, *Microwave Absorption Spectrum of ND_3* , Phys. Rev. **89**, 1101 (1953).
- [67] A. Lande, *Term Structure and the Zeeman Effect of Multiplets*, Z. Phys. **19**, 112 (1923).
- [68] M. Zinner, P. Spoden, T. Kraemer, G. Birkel, and W. Ertmer, *Precision Measurement of the Metastable 3P_2 Lifetime of Neon*, Phys. Rev. A **67**, 010501 (2003).
- [69] N. E. Small-Warren and L.-Y. C. Chiu, *Lifetime of the Metastable 3P_2 and 3P_0 States of Rare-Gas Atoms*, Phys. Rev. A **11**, 1777 (1975).

Bibliography

- [70] R. W. Anderson, *Tracks of Symmetric Top Molecules in Hexapole Electric Fields*, J. Phys. Chem. A **101**, 7664 (1997).
- [71] C. Hammer, R. Pidd, and K. Terwilliger, *Betatron Oscillations in the Synchrotron*, Rev. Sci. Instrum. **26**, 555 (1955).
- [72] M. Kirste, H. Haak, G. Meijer, and S. Y. T. van de Meerakker, *A Compact Hexapole State-Selector for NO Radicals*, Rev. Sci. Instrum. **84**, 073113 (2013).
- [73] M. Galassi *et al.*, *GNU Scientific Library Reference Manual (3rd Ed.)*, ISBN 0954612078.
- [74] Comsol, *Multiphysics 4.3a*, (2012).
- [75] P. Zugenmaier, *Zur Theorie der Molekularstrahlerzeugung mit Hilfe zylindrischer Rohre*, Z. Angew. Phys. **20**, 184 (1966).
- [76] P. R. Bunker and P. Jensen, *Molecular Symmetry and Spectroscopy*, NRC Research Press, Ottawa, Ontario, Canada, 2nd edition, (1998).
- [77] J. Bentley, B. Cotterell, A. Langham, and R. Stickland, *2+1 Resonance-Enhanced Multiphoton Ionisation Spectroscopy of the High v_2 Levels of the $\tilde{B} E'_1$ Rydberg State of $\text{NH}_3(\text{ND}_3)$* , Chem. Phys. Lett. **332**, 85 (2000).
- [78] S. Deachapunya, P. J. Fagan, A. G. Major, E. Reiger, H. Ritsch, A. Stefanov, H. Ulbricht, and M. Arndt, *Slow Beams of Massive Molecules*, Eur. Phys. J. D **46**, 307 (2008).
- [79] L. Cowley, M. Fluendy, and K. Lawley, *A Radial Disk Velocity Selector for Molecular Beams*, Rev. Sci. Instrum. **41**, 666 (1970).
- [80] B. Ghaffari, J. Gerton, W. McAlexander, K. Strecker, D. Homan, and R. Hulet, *Laser-Free Slow Atom Source*, Phys. Rev. A **60**, 3878 (1999).
- [81] S. A. Rangwala, T. Junglen, T. Rieger, P. W. H. Pinkse, and G. Rempe, *Continuous Source of Translationally Cold Dipolar Molecules*, Phys. Rev. A **67**, 043406 (2003).
- [82] T. Rieger, T. Junglen, S. A. Rangwala, P. W. H. Pinkse, and G. Rempe, *Continuous Loading of an Electrostatic Trap for Polar Molecules*, Phys. Rev. Lett. **95**, 173002 (2005).
- [83] M. Motsch, L. D. van Buuren, C. Sommer, M. Zeppenfeld, G. Rempe, and P. W. H. Pinkse, *Cold Guided Beams of Water Isotopologs*, Phys. Rev. A **79**, 013405 (2009).
- [84] M. Motsch, M. Schenk, L. D. van Buuren, M. Zeppenfeld, P. W. H. Pinkse, and G. Rempe, *Internal-State Thermometry by Depletion Spectroscopy in a Cold Guided Beam of Formaldehyde*, Phys. Rev. A **76**, 061402 (2007).
- [85] S. Willitsch, M. T. Bell, A. D. Gingell, S. R. Procter, and T. P. Softley, *Cold Reactive Collisions between Laser-Cooled Ions and Velocity-Selected Neutral Molecules*, Phys. Rev. Lett. **100**, 043203 (2008).

- [86] A. D. Gingell, M. T. Bell, J. M. Oldham, T. P. Softley, and J. N. Harvey, *Cold Chemistry with Electronically Excited Ca^+ Coulomb Crystals*, J. Chem. Phys. **133**, 194302 (2010).
- [87] K. Okada, T. Suganuma, T. Furukawa, T. Takayanagi, M. Wada, and H. A. Schuessler, *Cold Ion-Polar Molecule Reactions Studied with a Combined Stark-Velocity-Filter-Ion-Trap Apparatus*, Phys. Rev. A **87**, 043427 (2013).
- [88] M. Motsch, C. Sommer, M. Zeppenfeld, L. D. van Buuren, P. W. H. Pinkse, and G. Rempe, *Collisional Effects in the Formation of Cold Guided Beams of Polar Molecules*, New J. Phys. **11**, 055030 (2009).
- [89] W. Wiley and I. McLaren, *Time-Of-Flight Mass Spectrometer with Improved Resolution*, Rev. Sci. Instrum. **26**, 1150 (1955).
- [90] T. Junglen, T. Rieger, S. Rangwala, P. Pinkse, and G. Rempe, *Slow Ammonia Molecules in an Electrostatic Quadrupole Guide*, Eur. Phys. J. D **31**, 365, (2004).
- [91] C. Sommer, M. Motsch, S. Chervenkoy, L. D. van Buuren, M. Zeppenfeld, P. W. H. Pinkse, and G. Rempe, *Velocity-Selected Molecular Pulses Produced by an Electric Guide*, Phys. Rev. A **82**, 013410 (2010).
- [92] P. C. Zieger, C. J. Eyles, G. Meijer, and H. L. Bethlem, *Resonant Excitation of Trapped Molecules in a Molecular Synchrotron*, Phys. Rev. A **87**, 043425 (2013).
- [93] G. Scoles (Editor), *Atomic and Molecular Beam Methods*, volume 2, Oxford University Press, New York / USA, (1992).
- [94] B. Davis and A. Barnes, *The Capture of Electrons by Swiftly Moving Alpha-Particles*, Phys. Rev. **34**, 152, (1929).
- [95] S. M. Trujillo, R. H. Neynaber, L. Marino, and E. W. Rothe, *Proc. of the IVth Int. Conf. on the Physics of Electronic and Atomic Collisions*, Science Bookcrafters (New York), (1965).
- [96] V. Belyaev, B. Brezhnev, and E. Erastov, *Measurement of Cross Sections of Ion-Atom Collisions at Low Energies by Method of Overtaking Beams*, JETP Letters-USSR **3**, 207 (1966).
- [97] S. Y. T. van de Meerakker, H. L. Bethlem, N. Vanhaecke, and G. Meijer, *Manipulation and Control of Molecular Beams*, Chem. Rev. **112**, 4828 (2012).
- [98] K. Luria, W. Christen, and U. Even, *Generation and Propagation of Intense Supersonic Beams*, J. Phys. Chem. A **115**, 7362 (2011).
- [99] M. Lara, F. Dayou, J.-M. Launay, A. Bergeat, K. M. Hickson, C. Naulin, and M. Costes, *Observation of Partial Wave Structures in the Integral Cross Section of the $\text{S}^{\dagger}(\text{D}_2) + \text{H}_2(j=0)$ Reaction*, Phys. Chem. Chem. Phys. **13**, 8127 (2011).

Bibliography

- [100] S. Chefdeville, T. Stoecklin, A. Bergeat, K. M. Hickson, C. Naulin, and M. Costes, *Appearance of Low Energy Resonances in CO – Para- H_2 Inelastic Collisions*, Phys. Rev. Lett. **109**, 023201 (2012).
- [101] I. Sims, J. Queffelec, A. Defrance, C. Rebrionrowe, D. Travers, P. Bocherel, B. Rowe, and I. Smith, *Ultralow Temperature Kinetics of Neutral-Neutral Reactions - The Technique and Results for the Reactions $CN + O_2$ down to 13 K and $CN + NH_3$ down to 25 K*, J. Chem. Phys. **100**, 4229 (1994).
- [102] L. Herbert, I. Smith, and R. Spencer-Smith, *Rate Constants for the Elementary Reactions between CN Radicals and CH_4 , C_2H_6 , C_2H_4 , C_3H_6 , and C_2H_2 in the Range $295 \leq T/K \leq 700$* , Int. J. Chem. Kinet. **24**, 791 (1992).
- [103] E. Lavert-Ofir, Y. Shagam, A. B. Henson, S. Gersten, J. Klos, P. S. Żuchowski, J. Narevicius, and E. Narevicius, *Observation of the Isotope Effect in Sub-Kelvin Reactions*, Nature Chem. **6**, 332 (2014).
- [104] J. Liouville, *Note sur la Théorie de la Variation des constantes arbitraires*, Journal de Mathématiques Pures et Appliquées **3**, 342 (1838).
- [105] J. Gibbs, *Elementary Principles in Statistical Mechanics: Developed with Especial Reference to the Rational Foundations of Thermodynamics*, Charles Scribner's Sons (1902).
- [106] J. Jankunas, B. Bertsche, K. Jachymski, M. Hapka, and A. Osterwalder, *Dynamics of Gas Phase $Ne^* + NH_3$ and $Ne^* + ND_3$ Penning Ionization at Low Temperatures*, submitted, arXiv:1405.0407, (2014).
- [107] J. Jankunas, B. Bertsche, and A. Osterwalder, *Study of the $Ne(^3P_2) + CH_3F$ Reaction Below 1 Kelvin*, J. Phys. Chem. A, accepted (2014).
- [108] J. H. Noroski and P. E. Siska, *Collision Energy Dependence of the Reactions of Metastable $Ne(2p^5\ 3s^3P_2, ^3P_0)$ with Small Molecules*, Chem. Phys. Lett. **475**, 208 (2009).
- [109] A. Aguilar, B. Brunetti, M. Gonzalez, and F. Vecchiocattivi, *A Crossed Beam Study of the Ionization of Molecules by Metastable Neon Atoms*, Chem. Phys. **145**, 211 (1990).
- [110] B. Lescop, M. BenArfa, G. LeCoz, M. Cherid, G. Sinou, A. LeNadan, and F. Tuffin, *Autoionization Process in the Penning Ionization of the CO Molecule by $Ne^*(^3P_0, ^3P_2)$ Metastable Atoms*, Chem. Phys. Lett. **252**, 327 (1996).
- [111] J. Balamuta, M. Golde, and Y. Ho, *Product Distributions in the Reactions of Excited Noble-Gas Atoms with Hydrogen-Containing Compounds*, J. Chem. Phys. **79**, 2822 (1983).
- [112] X. Chen and D. W. Setser, *Electronic Quenching Rate Constants for Xenon (3P_2), Argon (3P_0) and Argon (3P_2) Atoms by Fluorine-Containing Molecules: Silane, Dichlorosilane, Trichlorosilane, and Silicon Tetrachloride* J. Phys. Chem. **95**, 8473 (1991).

-
- [113] J. Balamuta and M. Golde, *Quenching of Metastable Ar, Kr, and Xe Atoms by Oxygen-Containing-Compounds - A Resonance Fluorescence Study of Reaction-Products*, J. Chem. Phys. **76**, 2430 (1982).
- [114] W. Tsang and R. Hampson, *Chemical Kinetic Data Base for Combustion Chemistry. Part I: Methane and Related Compounds*, J. Phys. Chem. Ref. Data **15**, (1986).
- [115] I. W. M. Smith, *Laboratory Astrochemistry: Gas-Phase Processes*, Annu. Rev. Astron. Astrophys. **49**, 29 (2011).
- [116] K. Jachymski, M. Krych, P. S. Julienne, and Z. Idziaszek, *Quantum Theory of Reactive Collisions for $1/r^n$ Potentials*, Phys. Rev. Lett. **110**, 213202 (2013).
- [117] Z. Idziaszek and P. S. Julienne, *Universal Rate Constants for Reactive Collisions of Ultra-cold Molecules*, Phys. Rev. Lett. **104**, 113202 (2010).
- [118] F. Mies and P. Julienne, *A Multichannel Quantum Defect Analysis of 2-State Couplings in Diatomic-Molecules*, J. Chem. Phys. **80**, 2526 (1984).
- [119] F. Mies, *A Multichannel Quantum Defect Analysis of Diatomic Predissociation and Inelastic Atomic Scattering*, J. Chem. Phys. **80**, 2514, (1984).
- [120] B. Bertsche and A. Osterwalder, *State-Selective Detection of Velocity-Filtered ND₃ Molecules*, Phys. Rev. A **82**, 033418 (2010).
- [121] B. Bertsche and A. Osterwalder, *Dynamics of Individual Rotational States in an Electrostatic Guide for Neutral Molecules*, Phys. Chem. Chem. Phys. **13**, 18954 (2011).
- [122] G. Di Domenicantonio, B. Bertsche, and A. Osterwalder, *Preparation of Translationally Cold Neutral Molecules*, Chimia **65**, 725 (2011).

BENJAMIN BERTSCHE

Birthday	10. January 1979	(Nürtingen, Germany)
Civil Status	married	(18.06.2010)
Children	Marla Loreen Bertsche	(06.08.2006)
	Romy Berenike Bertsche	(30.09.2008)

EDUCATION

PERIOD	October 2001 — July 2009	
DEGREE	Diplom-Physiker	
UNIVERSITY	Freie Universität	Berlin, Germany

PERIOD	1996 — 1999	
DEGREE	Allgemeine Hochschulreife	
SCHOOL	Technisches Gymnasium	Tuttlingen, Germany

WORK EXPERIENCE

PERIOD	January 2014 — July 2015	
JOB TITLE	Studienreferent (Mathematics and Physics)	
EMPLOYER	Staatliches Seminar für Didaktik und Lehrerbildung (Berufliche Schulen)	Freiburg i. Br., Germany

An education and preparation course for teachers.

PERIOD	September 2010 — Dezember 2013	
JOB TITLE	Assistant Doctoral	
EMPLOYER	École Polytechnique Fédérale de Lausanne (EPFL)	Lausanne, Switzerland

Including 648 hours of teaching undergraduate students in experimental physical chemistry (396 h), spectroscopy (56 h) and quantum chemistry (196 h).

PERIOD	September 2006 — July 2010	
JOB TITLE	Teaching Assistant	
EMPLOYER	Freie Universität	Berlin, Germany

Teaching experimental physics to students of veterinary medicine.

PUBLICATIONS

B. Bertsche and A. Osterwalder, *State-Selective Detection of Velocity-Filtered ND₃ Molecules*, Phys. Rev. A **82**, 033418 (2010).

B. Bertsche and A. Osterwalder, *Dynamics of Individual Rotational States in an Electrostatic Guide for Neutral Molecules*, Phys. Chem. Chem. Phys. **13**, 18954 (2011).

G. Di Domenicantonio, B. Bertsche, and A. Osterwalder, *Preparation of Translationally Cold Neutral Molecules*, Chimia **65**, 725 (2011).

HERMANN-LÖNS-STR. 3 · 79100 FREIBURG · GERMANY

✉ BENJAMIN.BERTSCHE@EPFL.CH ☎ +49-(0)172-7222634

